Winter 4-22-2019

A Characterization of Structures Across the Hurricane Ridge Fault in the Southeastern Olympic Peninsula, WA, Hamma Hamma River Transect

Veronica Catherine Biesiada
Portland State University

A Characterization of Structures across the Hurricane Ridge Fault in the Southeastern

Olympic Peninsula, WA, Hamma Hamma River Transect

by

Veronica Catherine Biesiada

A thesis submitted in partial fulfillment of the
requirements for the degree of

Master of Science
in
Geology

Thesis Committee:
Dr. Nancy Price
Dr. Ray Wells
Dr. Martin Streck

Portland State University
2019

Abstract

The Olympic Mountains in northwestern Washington, USA are defined by the arcuate shape of the basaltic Crescent Formation (Fm.) that wraps a faulted and folded meta-sedimentary core. This area was developed through accretion and exhumation by subduction-related processes, but how this relates to the deformational history of the area is not fully understood. The region has been mapped geologically, however little focus has been placed on interpreting meso-scale structures. This study investigates structures along a transect where the Hamma Hamma River crosses the Hurricane Ridge Fault, which juxtaposes the meta-sedimentary core (west) and the basaltic Crescent Fm. (east). In the study area, the meta-sedimentary unit is characterized by outcrop scale folding with a calculated fold axis of 69→342 and a penetrative foliation with a representative orientation of (178, 75). The folds and foliation are crosscut by two fracture populations with representative orientations of (115, 61) and (303, 76). The pillow basalts of the Crescent Fm. are near vertical, N-S striking beds that are cut by four fault groups. Fault Groups A and B have representative orientations of (304, 37) and (207, 59), respectively, and are associated with similarly oriented fracture populations. Fault Group C crosscuts Groups A and B and has a representative orientation of (031, 61). Fault Group D runs subparallel to the outcrop, cuts all other faults, and has a representative orientation of (087, 50). From an interpretation of this data, a deformation model is presented that proposes three distinct periods of deformation under three different states of stress. The first period was dominated by E-W or ENE-WSW oriented compression, followed by a period of N-S or NNW-SSE oriented compression, followed by vertical compression.

Acknowledgements

The writing of this thesis would not have been possible without the support of several individuals.

First, I would like to thank my research group, led by our adviser, Dr. Nancy Price, and includes Christine Maher, Eleanor Lahart, Alex Dill, and Alyssa Orr. These people have listened to hours of me talking about my research and have provided critical feedback and direction. Nancy has not only helped me grow as a geologist, but also as a person. She has taught me many life lessons and has given me great advice and I truly look up to her. Christine and I have also become very close throughout this process since we share an office and have similar research interests. I deeply value our friendship and am excited to see her complete her thesis work.

I would also like to thank the other members of my committee, Dr. Martin Streck and Dr. Ray Wells. Martin has been very supportive and always has a positive attitude when it comes to my thesis. I have been a big fan of Ray's since before I even started on this thesis. I was first introduced to Ray's work as an undergraduate at Indiana University while writing a paper for my plate tectonics class. I was fascinated by the clockwise rotation model of Siletzia and thought the figures in his papers did such a great job of explaining it. When I first met him, I was honestly star struck, so it has been a true honor to get to work with him. His expertise and guidance have helped me tremendously through writing this thesis.

My father, Michael Biesiada, mother, Jeanine Herold, and sister, Holly Biesiada have also been a great source of support throughout my whole life and especially over the last couple years. I would not be the person I am today without their love and encouragement.

Finally, I would like to thank Dr. James Brophy from the geology department of Indiana University. When I began college, I did not think of myself as an 'exceptional student'. However, Dr. Brophy saw something in me and pushed me to do a senior thesis with him and then encouraged me to apply for graduate school. He has been a big influence on me as a student and as a geologist and I am forever grateful for him believing in me.

Contents

List of Tables

Table Name and Title	Page
Table 5.1. Description of confidence levels for identifying fault groups in the pillow basalt outcrops.	58

List of Figures

1. Introduction

The Olympic Mountains make up the Olympic Peninsula of northwestern Washington, USA, and mark the northern extent of the Coast Ranges, which run parallel to the coast of western Washington and Oregon. The Coast Ranges are underlain by a large basaltic terrane, Siletzia, which was accreted to North America along the Cascadia subduction zone in the Eocene, about 50 Ma. The oceanic basalt of the Crescent Formation (Fm.) in the Olympic Mountains is part of Siletzia (Wells et al., 2014), and it forms an arcuate backstop around the meta-sedimentary core of the Olympics. The core is composed of highly disrupted sediments that were accreted at the Cascadia subduction zone beneath Siletzia (Tabor & Cady, 1978). The Hurricane Ridge Fault (HRF) is the major suture boundary between the Crescent Fm. and the meta-sedimentary core complex.

The peninsula has been mapped at the regional scale (Tabor & Cady, 1978; Gerstel & Lingley, 2000; Gerstel & Lingley, 2003; Logan, 2003; Schasse, 2003a & b), and Tabor and Cady (1979) interpreted the area to be a subduction accretionary complex exhumed by structural doming. Their model has several implications for the evolution of the major fault zones but a detailed analysis of the structures at the meso- and micro-scales has yet to be accomplished. A deeper understanding of the structures at a smaller scale will give insight into the deformational history of the rocks and better define the steps in their exhumation. The study area for this work is too small to directly make claims about the regional exhumational history, however, it is the beginning of a larger endeavor to map and understand meso- to micro- scale structures in the Olympics.

This study analyzes structures in the rock units on both sides of the HRF and compares how strain was accommodated in the meta-sedimentary core and the Crescent Fm. For each side of the fault, a detailed description of each structure's morphological expression in outcrop is presented, followed by their orientation measurements and an analysis of micro-structures. These descriptions and data are then interpreted and compared with regional data and background literature to construct a deformational model for strain accommodation in the study area for the Crescent Fm. and the meta-sedimentary core.

2. Background

The Olympic Peninsula is composed of core rocks and peripheral rocks that were accreted along the Cascadia subduction zone and subsequently tilted to near vertical orientations. The peripheral rocks refer to the turbidite composed Blue Mountain Unit, the basaltic Crescent Formation, and overlying sedimentary rocks. The core rocks are part of a meta-sedimentary accretionary complex, and can be divided into the eastern and western core (**Fig. 2.1**). The core rocks and peripheral rocks are separated by the Hurricane Ridge Fault (HRF). The core rocks are cut by major crustal faults that are subparallel to the HRF.

2.1 Geologic History of the Olympic Mountains

The Crescent Formation is part of Siletzia, a basaltic oceanic island chain that formed as a result of the Kula-Farallon Ridge moving over the Yellowstone Hotspot between 60 and 50 Ma (Duncan, 1982; Glassley, 1974; Wells et al., 2014). This large igneous province accreted onto North America approximately 50 Ma and crops out in anticlinal uplifts along the Oregon and Washington Coast Range (Wells et al., 2014). The Crescent Fm. is the largest exposure of Siletzia and forms a large horseshoe shape on the peninsula that wraps around the meta-sedimentary core.
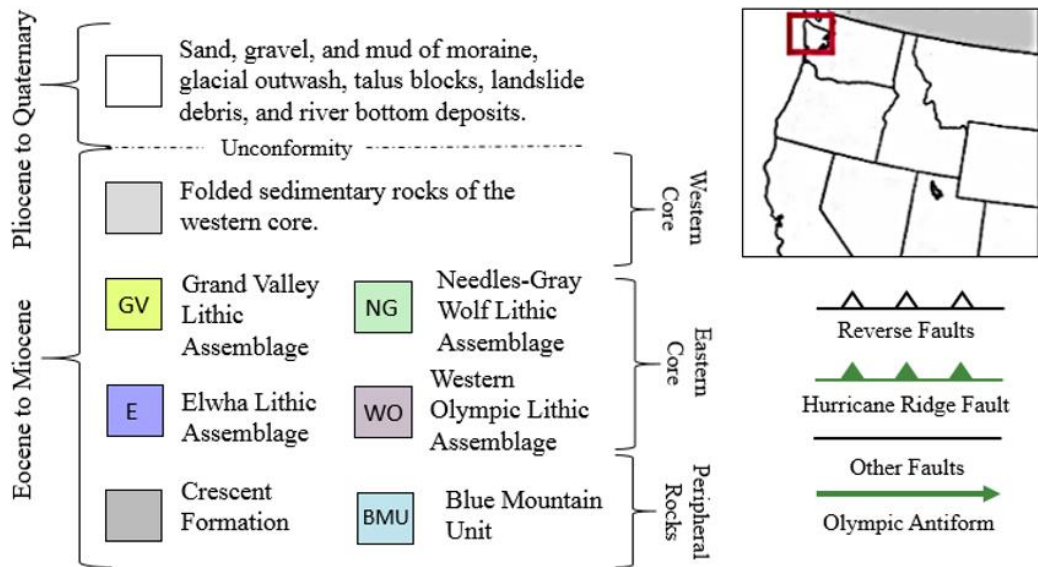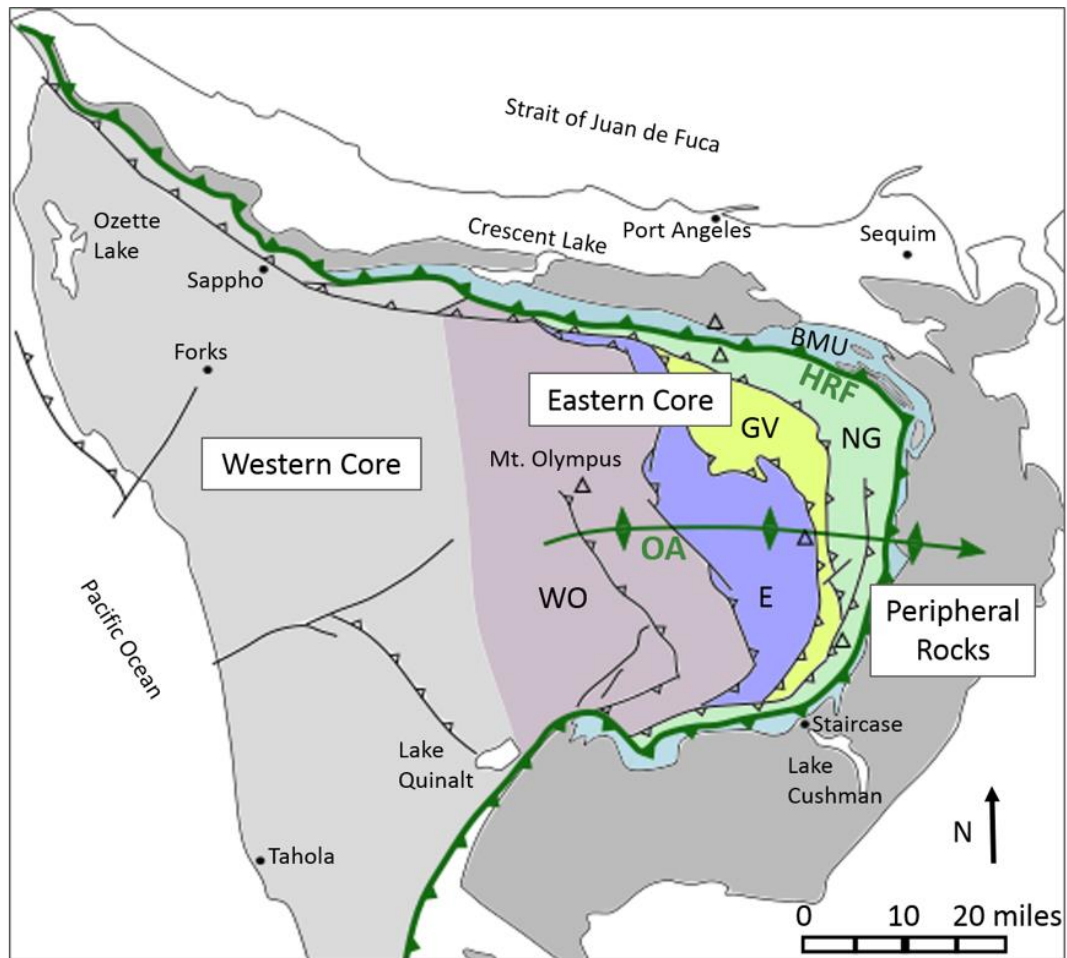
Figure 2.1. Geologic map highlighting the major structures and units of the Olympic Peninsula. Figure after Eddy, Clark, & Polenz (2017) and Tabor & Cady (1978).
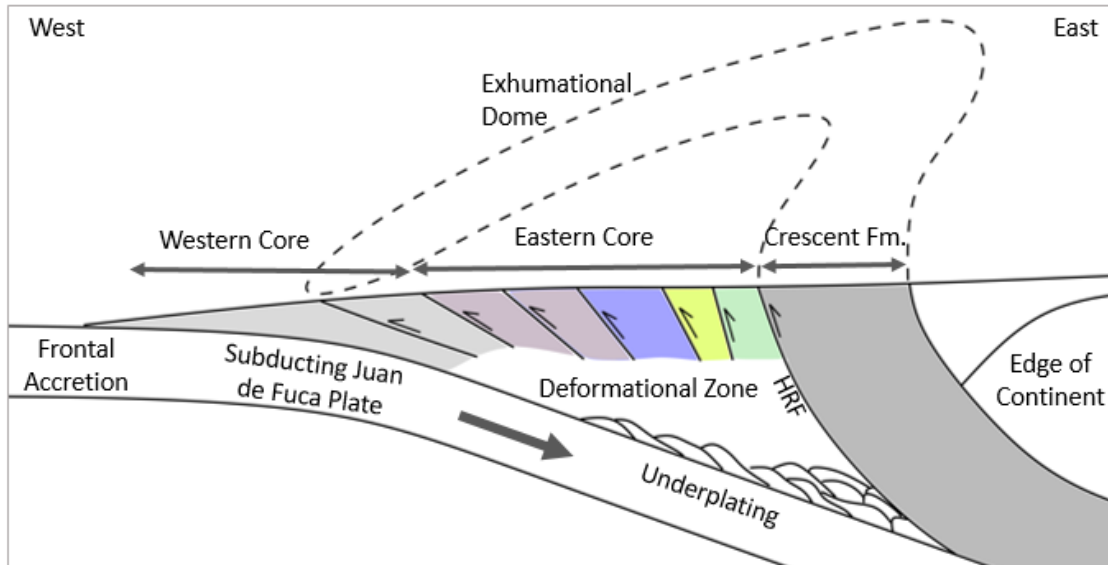
Figure 2.2. Cross sectional schematic of the Olympic Peninsula. Cross section runs west-east across the center of the peninsula. Figure interpreted and modified from Batt, Brandon, Farley, & Roden-Tice (2001); Eddy, Clark, & Polenz (2017); Tabor & Cady (1978).

Following the accretion of Siletzia, sedimentary material was accreted to the margin forming the sedimentary core. The accretion of these sediments involved classic frontal accretion and underplating, a process by which material is added beneath the margin (Brandon & Vance, 1992). The Crescent Fm. acted as a backstop to the meta-sediments, and continued E-W compression caused the sediments to deform by continued faulting and folding (**Fig. 2.2**; Tabor & Cady, 1978). As this process proceeded, the HRF steepened to its current, near-vertical, position (Tabor & Cady, 1978). Zircon and apatite fission track dating studies show that the Olympic Mountains began exhuming 18 Ma and have been uplifting in a uniform manner for at least the last 14 Ma (Batt et al., 2001; Brandon, Roden-Tice, & Carver, 1998).

2.2 Models of Olympic Exhumation

Two models exist for the driving mechanism of the exhumation of the Olympic Mountains. The first involves N-S oriented shortening from rotation of the micro-plates that make up the Pacific Northwest (McCaffrey et al., 2007; Wells, 1998; Wells & McCaffrey, 2013), and the other involves internal deformation of the accretionary wedge and steady state doming (Batt et al., 2001; Brandon & Vance, 1992; Pazzaglia & Brandon, 2001).

Extensive mapping of the Pacific NW GPS velocity field shows clockwise rotation of the Cascadian forearc (McCaffrey et al., 2007). This causes E-W oriented extension in southeastern Oregon and N-S oriented shortening in northwestern Washington of Siletzia against the North American Buttress (**Fig. 2.3**; Wells et al., 1998; Wells & McCaffrey, 2013). This rotation is caused in part by the oblique subduction of the Juan de Fuca plate beneath the North American plate (Wells et al., 2014; Wells & McCaffrey, 2013). Field mapping, paleomagnetic, and magmatic studies track the rotation over the last 16 my (Wells & McCaffrey, 2013).

N-S oriented shortening from clockwise rotation of the Cascadia forearc is thought to drive faults in the Puget Lowland, including the Seattle Fault, the Tacoma Fault, the Olympic Fault, the Utsalady Point Fault, and the Southern Whidbey Island Fault (Wells et al., 1998; Blakely et al., 2009). In the Olympics, the Saddle Mountain, Canyon River, and Frigid Creek Faults, which are located in the Crescent Fm., have been interpreted as western extensions of the faults in the Puget Lowland, suggesting that the

deformation from N-S shortening extends into the peninsula (Blakely et al., 2009; Lamb et al., 2012).
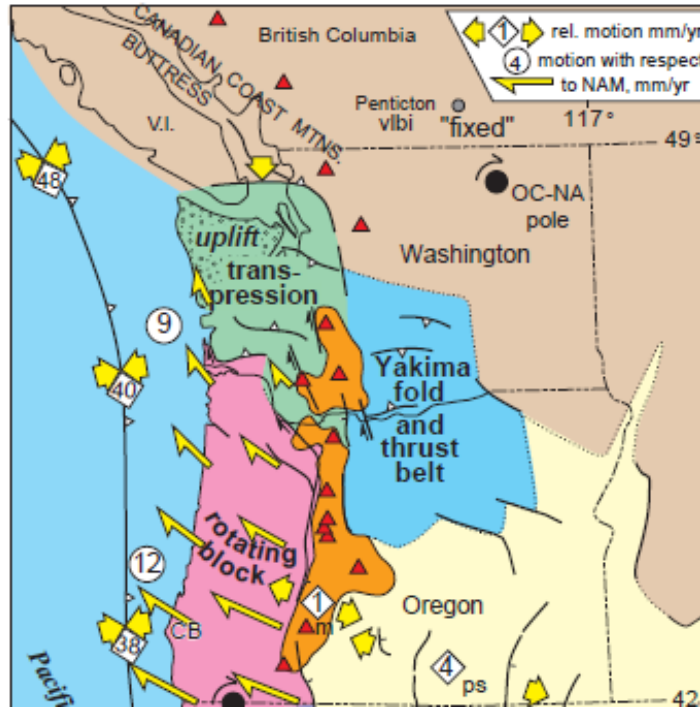
Figure 2.3. Schematic of the velocity field for the Pacific NW. The Oregon block (pink) and the Washington block (green) rotate clockwise about an Euler pole in NE Washington. This causes extension in southeastern Oregon and uplift and transpression in northwestern Washington. Modified from Wells et al. (2014).

The other model for Olympic exhumation posits that uplift resulted from internal deformation in the accretionary wedge (Tabor and Cady, 1979; Batt et al., 2001; Brandon & Vance, 1992; Pazzaglia & Brandon, 2001). Deformation within the meta-sedimentary core caused wedge thickening and exhumation of the Olympics as a mushroom-shaped dome over the last 18 Ma. Mass balance and zircon/apatite fission track studies indicate that the mountain range was in a steady-state flux, meaning that the amount of material being accreted was approximately equal to the erosional rate (Batt et al., 2001; Brandon & Vance, 1992; Pazzaglia & Brandon, 2001). This suggests that the only stresses that

caused deformation in the mountain range were those associated with subduction zone convergence (Batt et al., 2001; Brandon & Vance, 1992; Pazzaglia & Brandon, 2001).

2.3 Description of Rock Units

The Crescent Fm. consists of Eocene basalts up to 16 km thick in the eastern portion of the peninsula. The formation consists of an upper member that outcrops in the east and a lower member that is exposed in the west. The Lower Crescent is tholeiitic in composition and is characterized by pillow basalts at the base that change upward stratigraphically to subaerial basalt (Eddy et al., 2017; Glassley, 1974). The basal portion of the Lower Crescent has a 53 Ma age and has been metamorphosed to lower greenschist facies by burial (Eddy, Clarke, & Polenz, 2017; Hirsch & Babcock, 2009). The Upper Crescent has a 47 Ma age (Eddy, Clarke, & Polenz, 2017) and is characterized by columnar and massive basalt and changes upward stratigraphically from tholeiitic to alkali basalts (Glassley, 1974).

The Blue Mountain Unit (BMU) beneath the Crescent Fm. is composed of marine turbidites (sandstone and mudstone), that formed from the erosion of the Crescent Fm. before it was accreted (Wells et al., 2014). The unit has an interfingering contact with the Crescent Fm. and overlies the HRF. The BMU has, until recently, been considered conformable with the Crescent Fm., however its age of 44 Ma suggests that it is thrust beneath the older Crescent Fm. (Eddy, Clarke, & Polenz, 2017).

The meta-sedimentary core is Eocene-to-Miocene in age and is composed of metamorphosed sediments that were initially deposited offshore (Tabor and Cady, 1978). The core is separated into western and eastern sections based on metamorphic grade and

degree of deformation. The rocks of the western core are younger and were

metamorphosed to laumontite facies (Orange, Geddes, & Moore, 1993). The eastern core

comprises four lithic assemblages (ie., Needles-Gray Wolf, Grand Valley, Elwha, and

Western Olympic; Fig. 2.1) separated by faults that run parallel to the HRF (Tabor and

Cady, 1978). These assemblages contain varying amounts of slate, phyllite, schist, and

feldspathic-to-basaltic lithic meta-sandstone that were metamorphosed to laumontite

grade in the west and epidote-chlorite grade in the east (Hirsch & Babcock, 2009; Tabor

& Cady, 1978). Folding is prevalent in the metasedimentary core, with a higher degree

of deformation in the east than the west.

2.4 Structural Geology of the Olympic Mountains

The regional structure of the Olympic Peninsula is dominated by the Olympic

Antiform (OA; **Fig. 2.4**) and the crustal faults of the meta-sedimentary core. The

Olympic Antiform describes the horseshoe-shaped map pattern of the Crescent Fm., the

axis of which runs E-W through the center of the peninsula. Tabor and Cady (1978)

interpret this structure to be the result of mushroom-like doming of the Crescent Fm.

during the exhumation of the meta-sedimentary core. The meta-sedimentary core is

bound by the Hurricane Ridge Fault (HRF) and other faults that run roughly parallel to

and join the HRF (**Fig. 2.4**). The HRF is interpreted as a high angle fault that juxtaposes

the peripheral rocks (hanging wall) with the meta-sedimentary core (footwall) (Tabor &

Cady, 1978). Tabor and Cady (1978) infer the location of other crustal faults of the meta-

sedimentary core by changes in lithology and presence of tectonic breccia. These faults

separate the major lithic assemblages, which get younger to the west, and are interpreted

as imbricate thrusts. In the northern and southern edges of the meta-sedimentary core

(i.e., Southern and Calawah Fault Zones; SFZ and CAFZ, **Fig. 2.5**) NE-SW and NW-SE

trending faults truncate the N-S trending faults that run across the core (Schasse, 2003).

2.4.1 Structures in the Eastern Core

Folds

Folding is prevalent in the meta-sedimentary core, and the area has been termed a

'chaotically' folded terrane (Tabor & Cady, 1978). For the most part, the folds are

outcrop scale and unmappable, however, there are some larger-scale folds in the western

core (**Fig. 2.4**).

Folds are typically isoclinal, and fold axial planes are commonly subparallel to

bedding. Following the structural domains of Tabor and Cady (1978) (**Fig. 2.5**), the beds

and axial planes of the 'central domains' strike more N-S and dip to the west and those of

the western domains strike NW to NNW and dip to the east. Fold axes were not

measurable in all domains, but where they were measured, an observed pattern shows

that the axes plunge away from the HRF in the east (domains 1, 2, 5, and 12) and towards

it in the west (domains 16 and 17). Tabor and Cady (1978) consider these trends as

evidence for the mushroom-like dome shape of the Olympic core that formed as it was

exhumed.

The bedding planes and axial planes of the 'outer edge' domains follow the strike

of the HRF and dip away from it (**Fig 2.5**). Tabor and Cady (1978) cite this trend as

evidence that the horseshoe-shape of the Crescent Formation was established early.

Structural Fabrics

There are two main structural fabrics of note in the Olympic core: cleavages and pencil structures.

Cleavages are defined by planar features that crosscut and, often, offset beds (**Fig. 2.5**). Where folds are isoclinal, cleavages are parallel to bedding measurements and show similar trends regionally. More than one generation of cleavage is documented throughout the meta-sedimentary core (i.e., domains 4, 12, and 16; Tabor & Cady, 1978). Movement along cleavage planes commonly sheared off the hinges of folds, transposing beds into an orientation subparallel to the cleavage (Tabor & Cady, 1978).

The pencil structures are thin slivers of rock that form at the intersection of either two cleavages or of a cleavage plane and a bedding plane (Tabor & Cady, 1978). These pencils show a radial pattern in which they trend away from the HRF and plunge towards the core (**Fig. 2.6**). This is also cited as evidence by Tabor and Cady (1978) for the mushroom-like dome shape of the Olympic core.
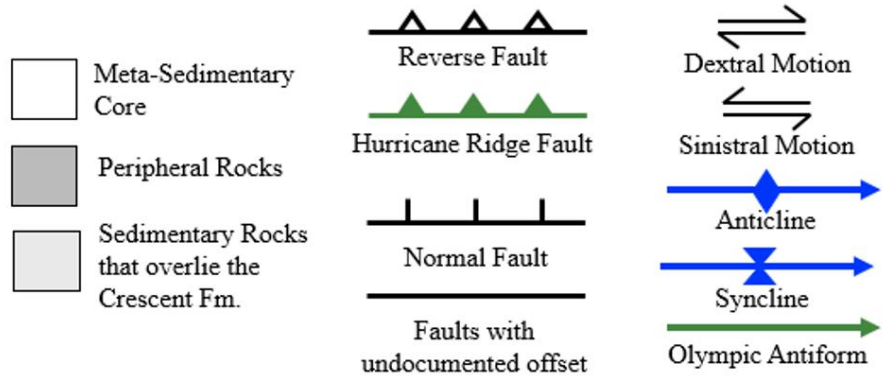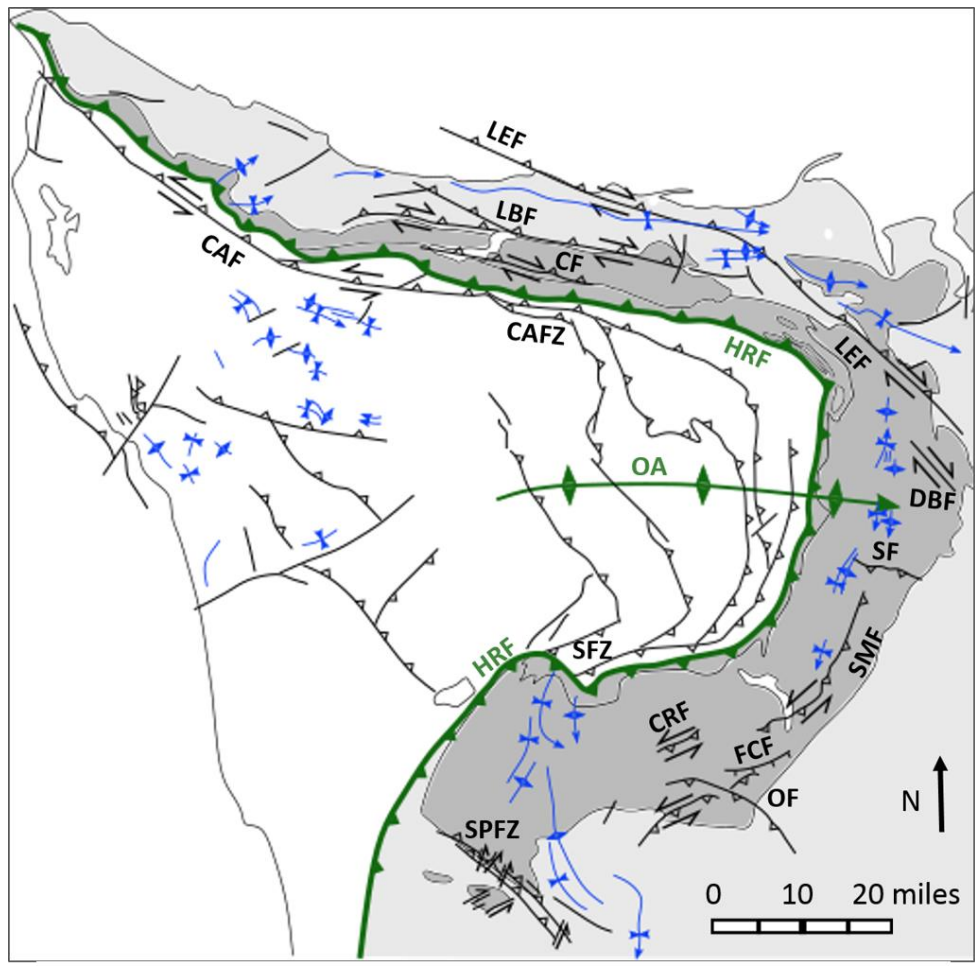
Figure 2.4. Map of structures present in the Olympic Peninsula. Information compiled and modified from**:** Blakely et al. (2009); Eddy et al. (2017); Gerstel & Lingley (2000); Gerstel & Lingley (2003); Joyner (2016); Logan (2003); Orange, Geddes, & Moore (1993); Schasse (2003); Tabor & Cady (1978)**.** Abbreviations: **CAF**=Calawah Fault, **CAFZ**=Calawah Fault Zone **CF**=Crescent Fault, **CRF**=Canyon River Fault, **DBF**=Dabob Bay Fault, **FCF**= Frigid Creek Fault, **HRF**=Hurricane Ridge Fault, **LBF**=Lake-Creek-Boundary-Creek Fault, **LEF**=Lower Elwha Fault, **OA**=Olympic Antiform, **OF**=Olympic Fault, **SF**=possible extension of the Seattle Fault, **SMF**=Saddle Mountain Fault, **SFZ**=Southern Fault Zone.
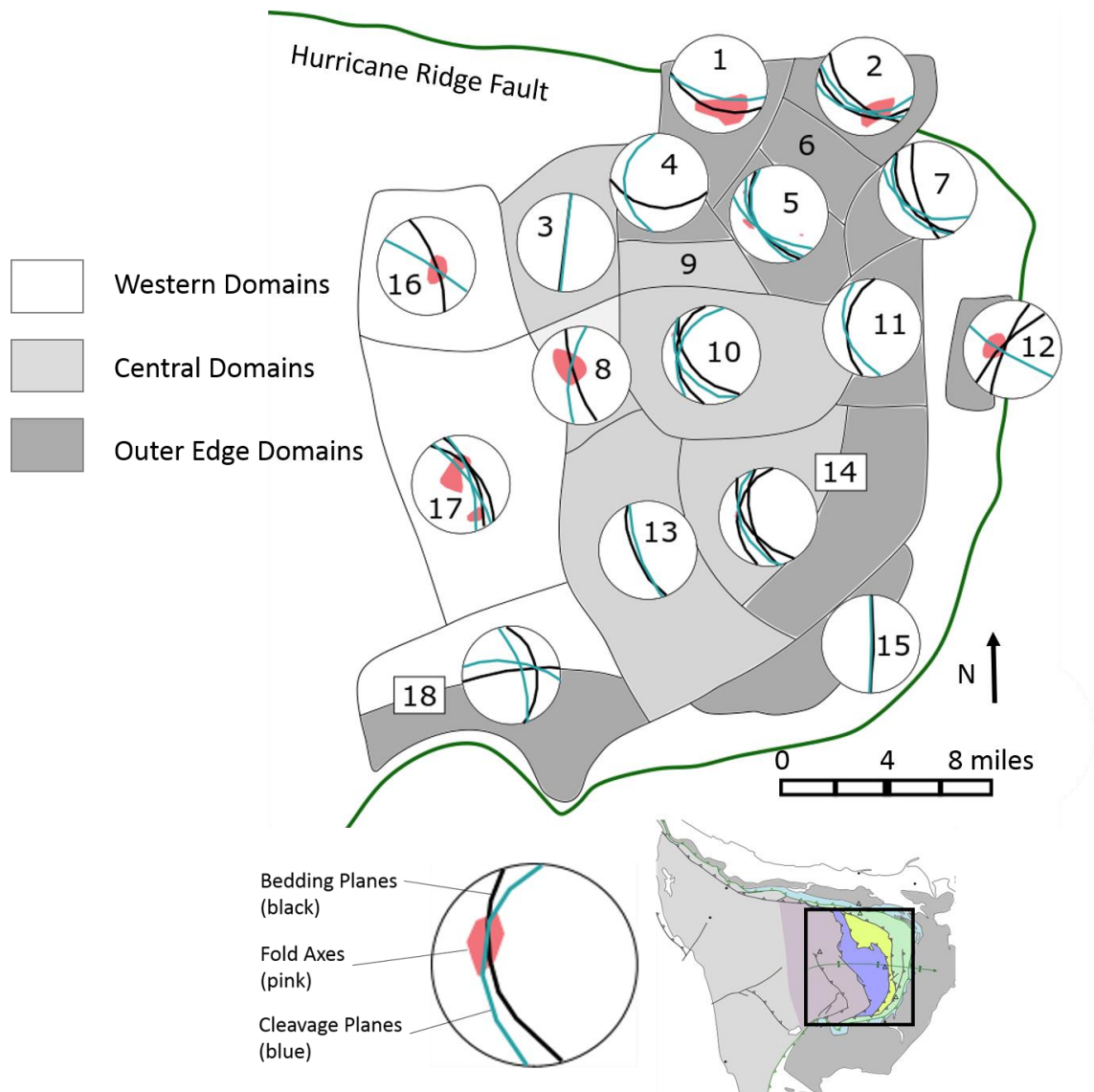
Figure 2.5. Structural domains for the eastern meta-sedimentary core with representative structural measurements. Domains are grouped into outer edge, central, and western areas based on trends in the data. Plots show lower hemisphere stereographic projections. Bedding and cleavage orientations show representative planes, and fold axes show the range of data points. Modified from Tabor and Cady (1978).
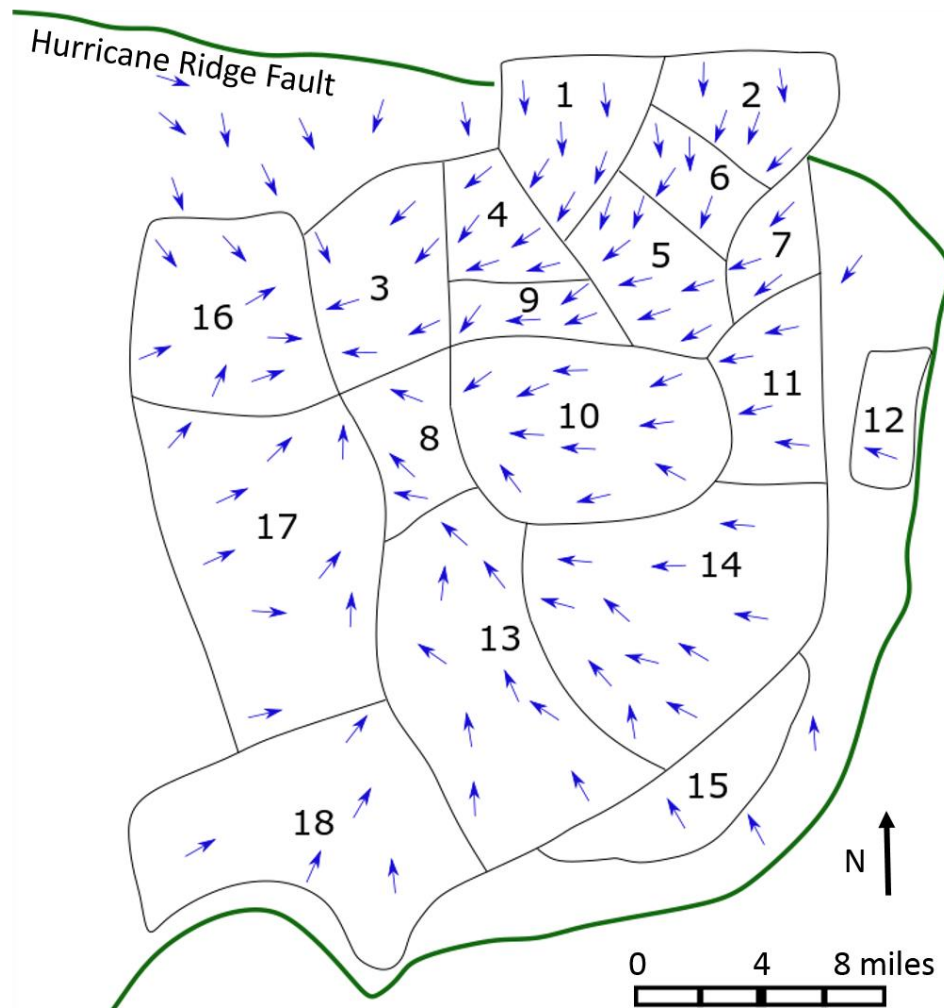
Figure 2.6. Plunge direction of pencil structures in the eastern core. Modified from Tabor and Cady (1978).

2.4.2 Structures in the Peripheral Rocks

Faults

Faults have been mapped throughout the peripheral rocks that strike parallel to the HRF and dip away from the core (**Fig. 2.5**). In the north, the Lake Creek-Boundary Creek, Lower Elwha, and Crescent faults are high angle, E-W oriented, reverse faults, with a component of dextral shear (Eddy et al., 2017; Joyner, 2016). These northern faults are interpreted as imbricates of one another and the HRF (Eddy et al., 2017). In the

central east, the Dabob Bay fault strikes NW-SE, shows dextral motion, and is likely an en echelon portion of the Lower Elwha Fault (Blakely et al., 2009). The central east also shows a possible extension of the Seattle Fault, which has been inferred by magnetic anomalies (Blakely et al., 2009). In the southeast, NE-SW oriented faults including the Saddle Mountain, Canyon River, and other unnamed faults, show reverse, sinistral motions (Blakely et al., 2009; Logan, 2003, Walsh & Logan, 2007). Also in the southeast are the normal Frigid Creek Fault and the reverse northernmost portion of the Olympic Fault (Blakely et al., 2009). An area at the southern edge of the peripheral rocks differs from the trend of the other faults in that these NE-SW oriented southernmost faults do not strike parallel to the HRF and are offset by mostly sinistral strike-slip faults (Logan, 2003).

Additional faults are inferred by geochronological inconsistencies. Recent dating of the Blue Mountain Unit shows that the Blue Mountain Unit and Lower Crescent Formation are not conformable, suggesting that there is a fault separating the two units (Eddy et al., 2017). This fault has not been officially mapped, but its presence would be a continuous fault that parallels the HRF.

Folds

Numerous folds are mapped in the peripheral rocks, though they are rarely discussed in literature (Gerstel & Lingley, 2000; Gerstel & Lingley, 2003; Logan, 2003; Schasse, 2003). The folds follow the same general pattern as the faults with axes that parallel the HRF, however, they are generally at the middle of the Crescent Fm., near the boundary between the Upper and Lower members. As with the faults in the southernmost

part of the peripheral rocks, folds in this area do not follow the HRF but trend NNE-SSW.

3. Methods

Four outcrops were chosen for this study (**Fig. 3.1**): two in the Needles-Gray Wolf Lithic Assemblage of the eastern core (referred to here as the meta-sediments), and two in the Crescent Fm. on the eastern side of the HRF (also referred to here as the pillow basalt). The transect is 5 kilometers long, and the outcrops are 50-150 meters long. Each site is further subdivided by letter (e.g., **Figures 4.1 and 5.1**). Site 1 begins at the Mildred Lakes Trailhead and is a semi-continuous meta-sedimentary outcrop; the Hamma Hamma River cuts through between Sites 1c and 1d. Outcrop exposures on the western side of the river are cliffs that lead down to the river. The eastern side exposures are steep to near vertical outcrops and run along the road. Site 2 is also in the meta-sediments, about 800m northeast of Site 1, and is a steep to near vertical outcrop that runs along the road. Sites 3 and 4 are in the Crescent Fm. and are tall, steep outcrops of pillow basalt. Site 3 is approximately 1600 m east of Site 2 and about 320 m east of the Putvin Trailhead. Site 4 is 300 m east of Site 3.
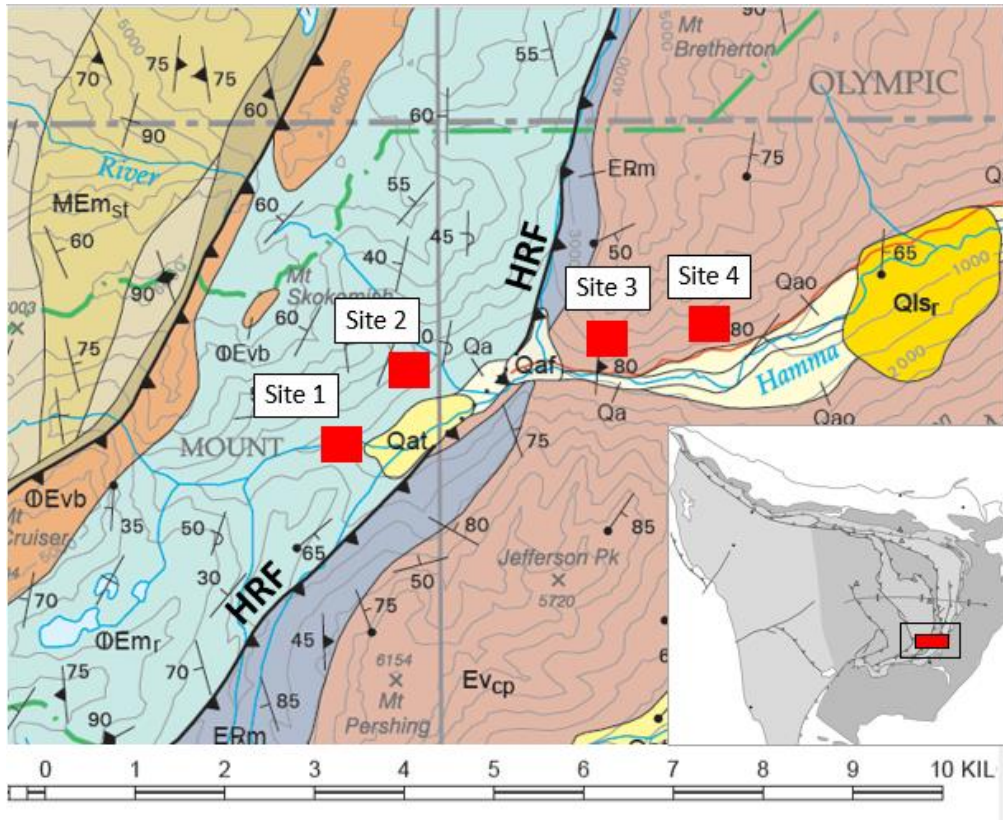
Figure 3.1. Geologic map with sites chosen for this study. Sites 1 and 2 are in the Needles-Gray Wolf Lithic Assemblage and Sites 3 and 4 are in Crescent Formation. Geologic map by Grestel and Lingley (2003).

At each site, I documented the type, orientation, and location of mesoscale structures (i.e., bedding, fractures, faults, veins, and fabrics) and crosscutting relationships between features. Outcrop maps were constructed in order to record the spatial relationship among the structures as well as the degree to which the structures are localized or homogenously distributed. Orientation measurements are representative of structure populations identified by qualitative observation. The exceptions to this are the faults identified in the pillow basalt outcrops, which were few in number and could be individually documented.

Oriented samples were collected in the meta-sedimentary outcrops to investigate the relative timing of fabric formation with respect to other structures such as bedding, veins, and fractures. I collected samples in the meta-sediments of relatively undisturbed and highly disturbed regions and of different rock types within the unit to compare how the structures vary. Oriented samples were collected in the pillow basalts to track how the pillows accommodate deformation and to look for evidence of fabric formation from core to rim and in the sedimentary matrix between pillows.

Samples were reoriented and cut relative to regional and/or relevant structures observed in the field and prepared into thin sections. Samples from the meta-sediments were cut perpendicular to the dominant fabric, and samples from the basalt were cut in map view. A petrographic microscope and a scanning electron microscope were used to identify mineral fabrics, shear structures, crosscutting relationships, and the mineral assemblage in veins.

Structure orientation data were plotted and analyzed using a graphing program called Stereonet, version 9.8 (see Allmedinger, Cardozo, & Fisher, 2013; Cardozo & Allmendinger 2013). All stereographic projections are lower hemisphere, equal area projections. Strike and dip measurements of planar structures (i.e., bedding, foliations, fractures, and veins) are shown as lines, and trend and plunge measurements of linear structures (i.e., slickenlines) are shown as points. Groupings in measurements were made by plotting poles to planes and then adding smoothed, 1% contours to the poles, with an interval of 2, significance level of 3, and 20 grid nodes. When groupings could be made in the data or when a structure type showed a consistent orientation, a 'representative

orientation' was identified by finding the midpoint of the data using the contours of the

poles to planes. It is important to note that measurements should be considered

qualitatively, as no statistical analysis has been conducted on the data.

Fold axes were determined by plotting poles to bedding planes and calculating

the cylindrical best fit. Axial planes of folds were estimated by bisecting the plotted

poles to bedding data, as guided by axial trace measurements taken in the field.

Calculations of the principal stresses (i.e., σ_1, σ_2, and σ_3) were determined using

Anderson's Theory of Faulting for fractures or faults interpreted as conjugates (**Fig 3.2;**

Anderson (1905)). The point of intersection of the fractures or faults is σ_2, and the plane

perpendicular to this intersection is the σ_1-σ_3 plane. The midpoint of the acute angle

(~60°) that the σ_1-σ_3 plane makes with the conjugate fractures or faults is σ_1, and the

midpoint of the obtuse angle (~120°) is σ_3.
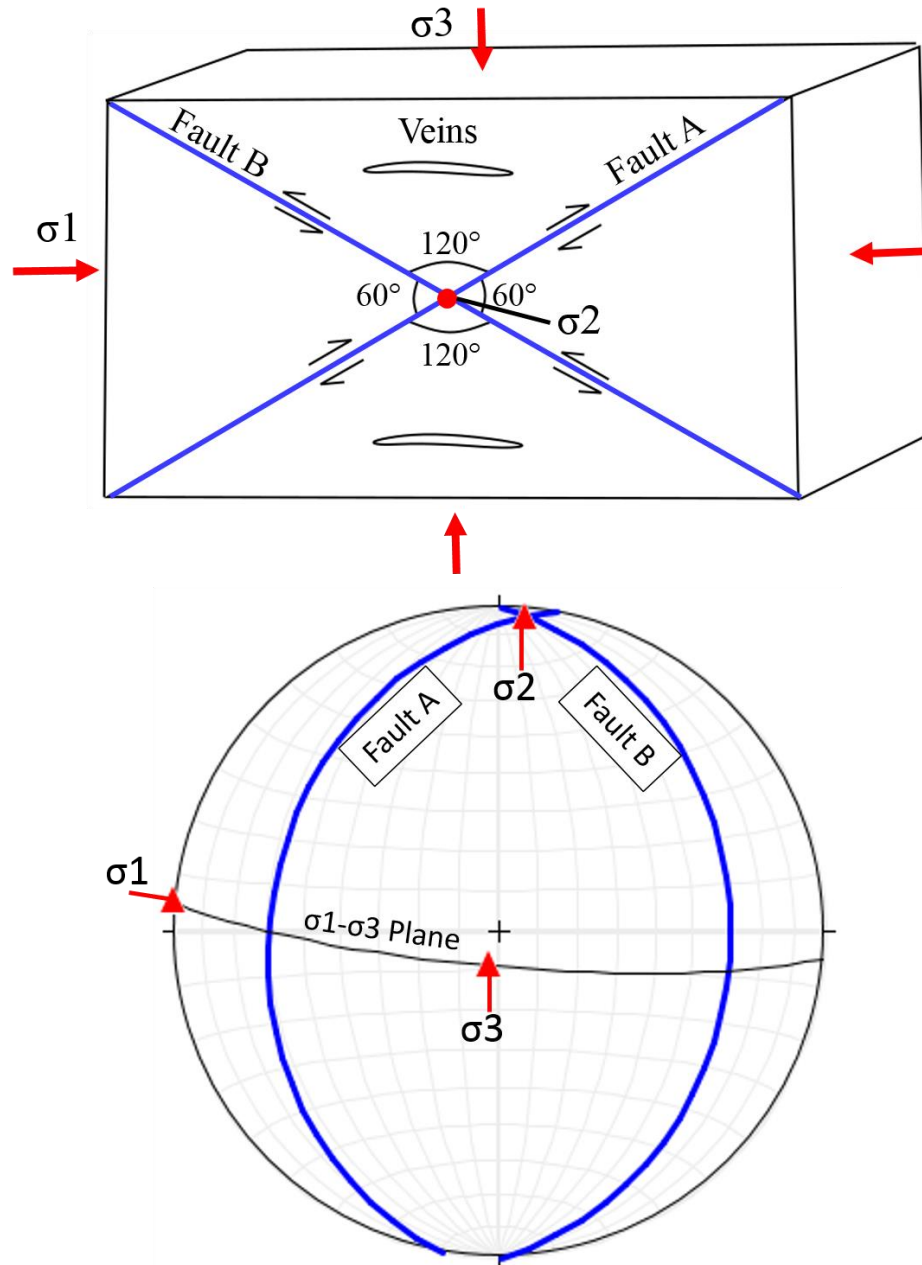
Figure 3.2. Diagram and corresponding stereonet of a representative compressional faulting setting showing the geometry and principal stresses for Anderson's Theory of Faulting. The example shown is that of two conjugate reverse faults, formed by E-W oriented maximum stresses (σ1), and vertical minimum stresses (σ3).

4. Meta-Sediments of the Hamma Hamma Transect

4.1 Data & Observations

4.1.1 Field Observations

At Sites 1 and 2, the structures of interest are bedding, foliations, fractures, and veins. Here, the bedding was defined by layers of slate and meta-sandstone. The layers range in thickness from 2 mm to about 2 m. Sites 1a, 1e, and 1f are predominantly slate; Sites 1b, 1c and 1d are predominately meta-sandstone; and Site 2 has relatively equal amounts of both rock types (**Fig. 4.1**). Fold hinges were identified at sites 1c (**Fig. 4.2**) and 2b indicating that the beds were folded.
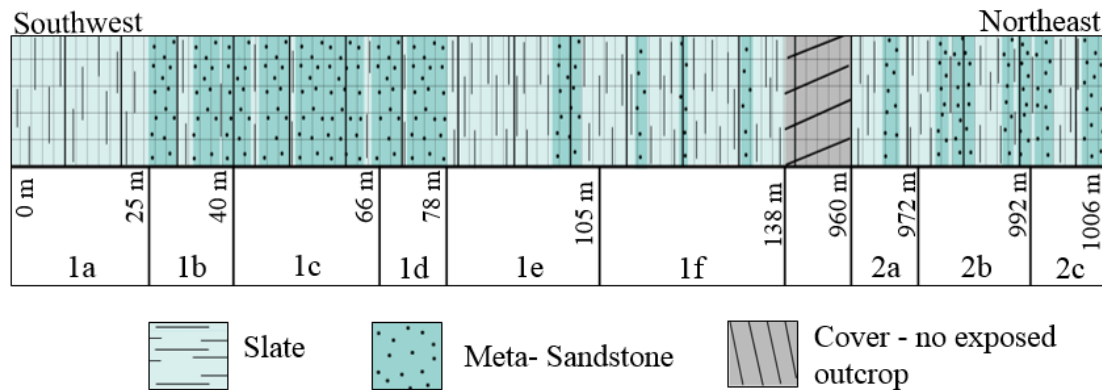
Figure 4.1. Diagram showing the length of each subsite of Sites 1 and 2 and the rock type present at each. The major lines of division on the column represent 10 m. Site 1a begins at the Mildred Lakes Trailhead, which represents "zero", and the numbers indicate how far a subsite is from this point. The column is not continuous; there is approximately 820 m of cover between the two sites.

Foliations are defined by planar mineral fabrics that can be seen along bedding planes. They are not parallel to bedding planes. In the predominantly slate layers and in layers of thin (0-10cm) interbedded slate and meta-sandstone, they cut across the bedding. In thicker (10-40) interbedded slate and meta-sandstone layers, they are

22

confined to the slate layers (**Fig. 4.3**). Foliations are not well-defined in the thicker meta-sandstone layers.

The beds are discontinuous and disrupted by fractures that crosscut and, in some places, offset the beds and foliations. The relative degree of disruption appears to correlate with rock type (**Fig. 4.4**). In the meta-sandstone layers (Sites 1b, 1c, and 1d), the fractures show fewer instances of offset, and the offset is traceable and measureable. Where offset is identifiable, lateral and reverse apparent motions offset beds between 5 and 50 cm (**Fig. 4.5**). The slate (Sites 1a, 1e, and 1f) and interbedded (2a, 2b, and 2c) layers appear to be more highly disrupted by the fractures; the amount of offset is difficult to measure due to the similarity in beds, which makes it hard to correlate them across the fracture planes. In some places, the fractures juxtapose beds of differing orientations, which indicates that they have been offset (**Fig. 4.6**). Lineations on the fracture surfaces are interpreted as slickenlines and the slickensides are smooth up dip on the footwall side of the fracture, suggesting a reverse sense of motion.

Quartz veins were identified in the meta-sediment outcrops and crosscut bedding and foliations (**Fig. 4.7**). They are generally linear but bifurcate amongst each other where there are groups. Veins range from 1 mm to 2 cm in thickness. The thinner ones have smaller crystals, whereas the thicker ones are blockier and have larger crystals. Veins span up to a meter in length and their length appears to correlate with rock type; thicker meta-sandstone layers have longer, thicker, veins, whereas thinner slate layers have shorter, thinner, veins. They typically occur as clusters (e.g. Site 1c), but in some places, a single vein is observed locally.
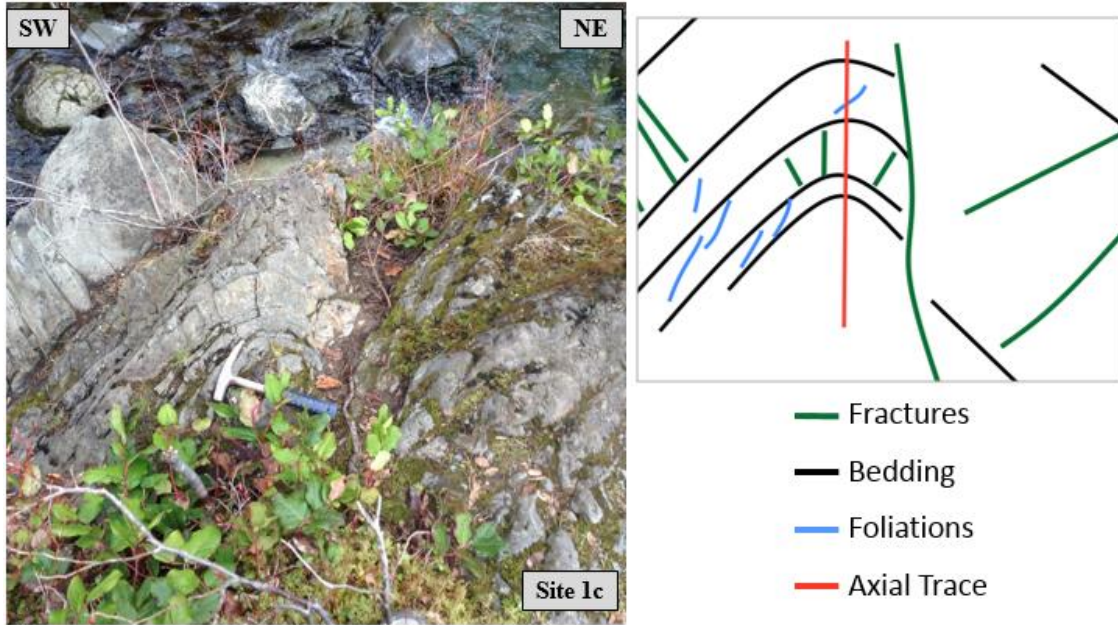
Figure 4.2. Photo of a fold hinge at Site 1c (left) with an interpretive diagram (right). The northeastern limb of the fold appears offset by a fracture. The photo was taken of a steeply inclined outcrop looking northwest. The rock hammer is 36 cm long.
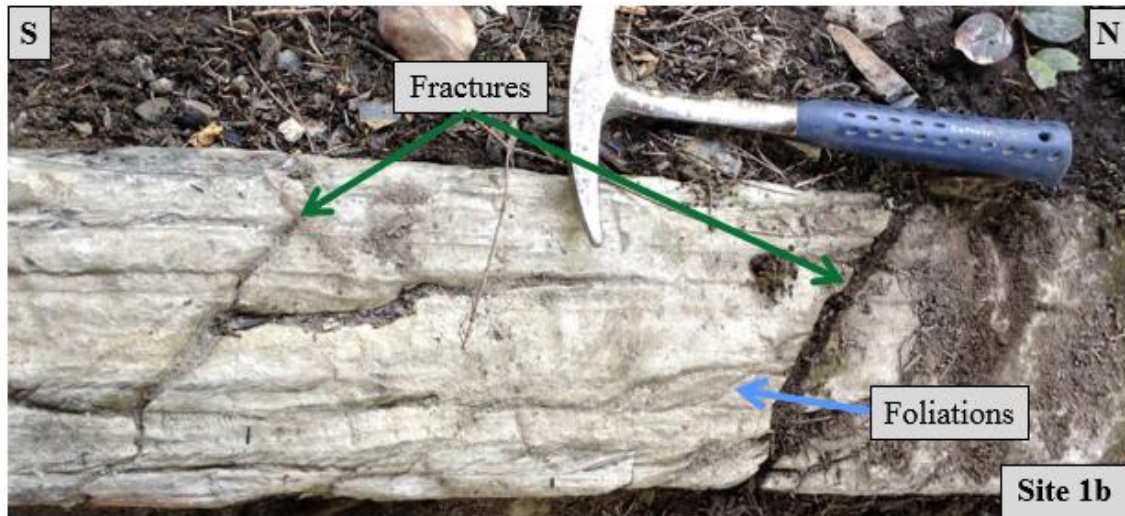
Figure 4.3. Photo showing fractures crosscutting, but not offsetting, bedding and foliations at Site 1b. Here, the bedding is thin layers of interbedded sand and slate. The photo is of a horizontal outcrop, with north to the right. The rock hammer is 36 cm long.
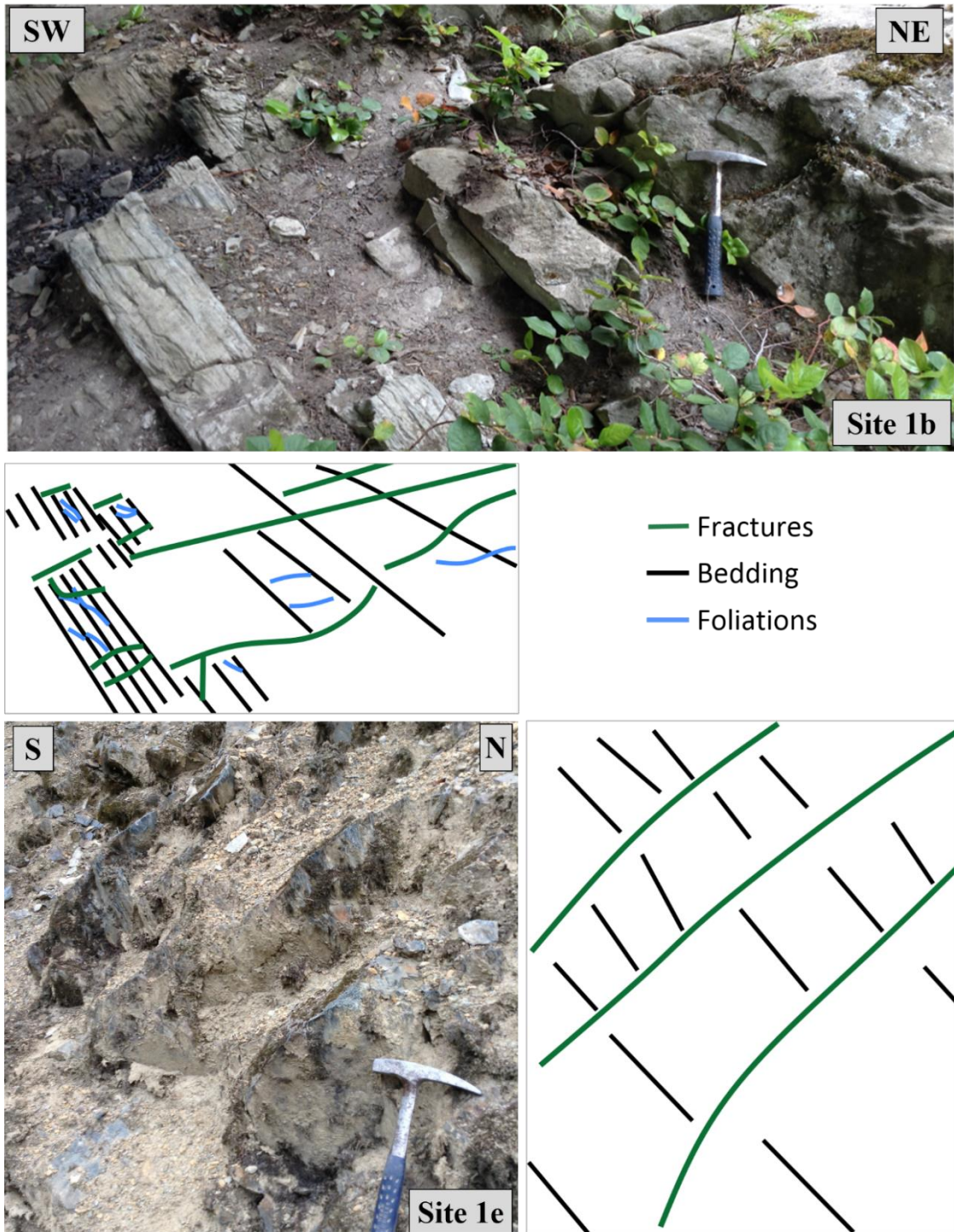
Figure 4.4. Photo of fractures cutting across meta-sandstone (above) and slate (below) layers with corresponding interpretive diagrams. The meta-sandstone layers show less disruption by fractures than the slate layers. In the meta-sandstone layers, bedding can be traced across fractures, and offset can be measured where present. Bedding and offset are more difficult to track across fractures in the slate layers. The meta-sandstone outcrop is horizontal and the slate outcrop is inclined. The rock hammer is 36 cm long.
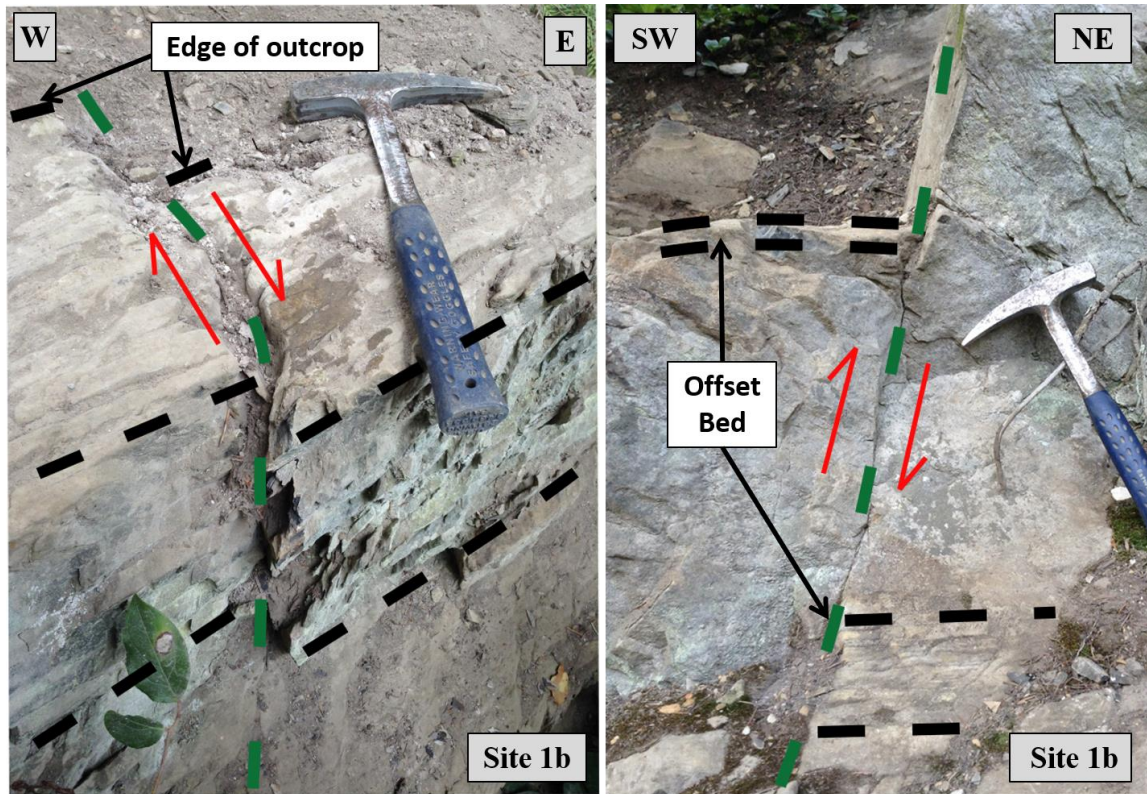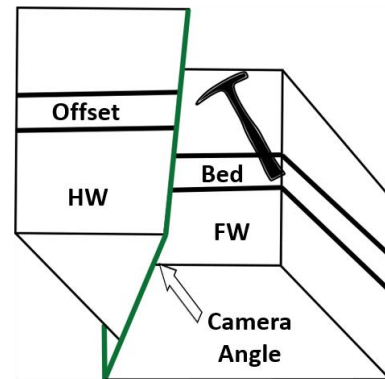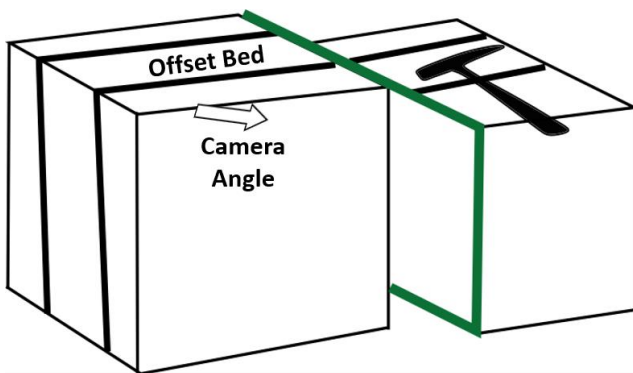
Figure 4.5. Photos of fractures with apparent offset at piercing points and corresponding block diagrams. The apparent right lateral offset of shale and meta-sandstone layers at left is approximately 10 cm, as marked by the edge of the outcrop. The apparent reverse dip-slip offset at right is approximately 45 cm, as marked by the offset bed. Block diagrams show the relationship among the offset beds, fractures, and camera angle. The rock hammer is 36 cm long.
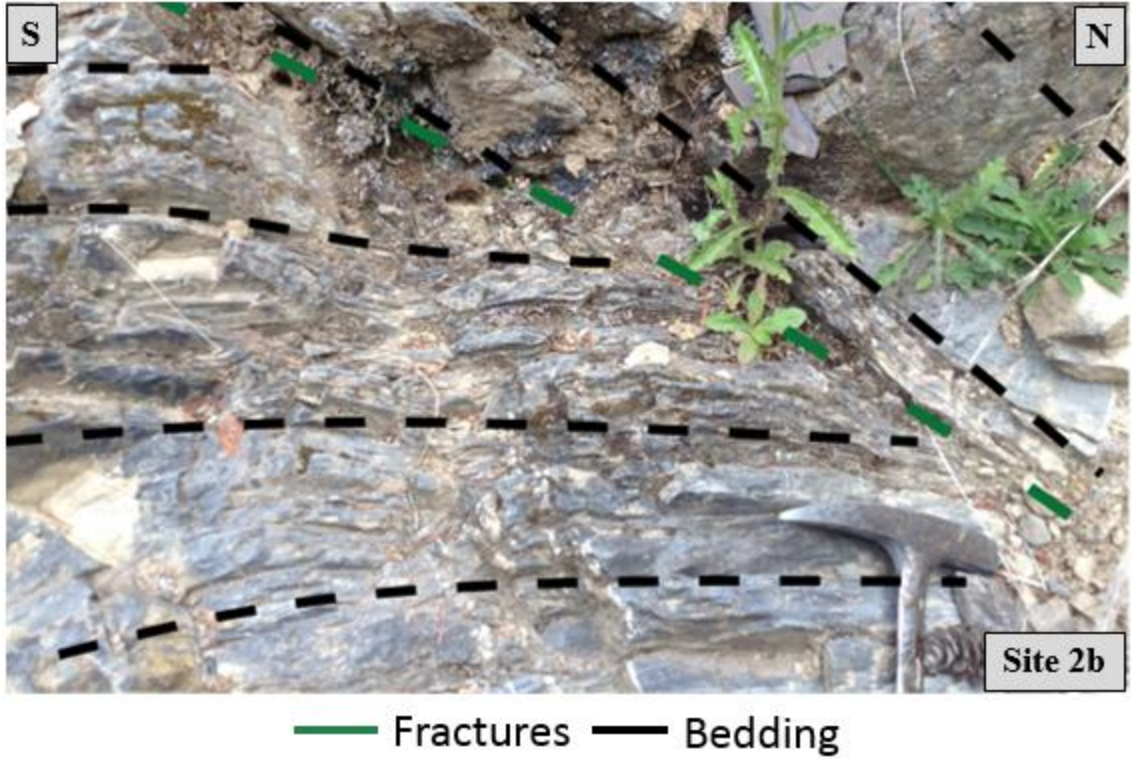
Figure 4.6. Photo of a fracture that has juxtaposed two beds of differing orientations. The beds, foliation, and veins in the bottom left [respectively, strike and dips of (225, 45), (189, 60), and (282, 55)] have orientations that are different from the beds in the top right [strike and dip of (028, 58)]. The fracture is oriented (291, 67). The photo was taken looking west and the head of the rock hammer is 15 cm long.
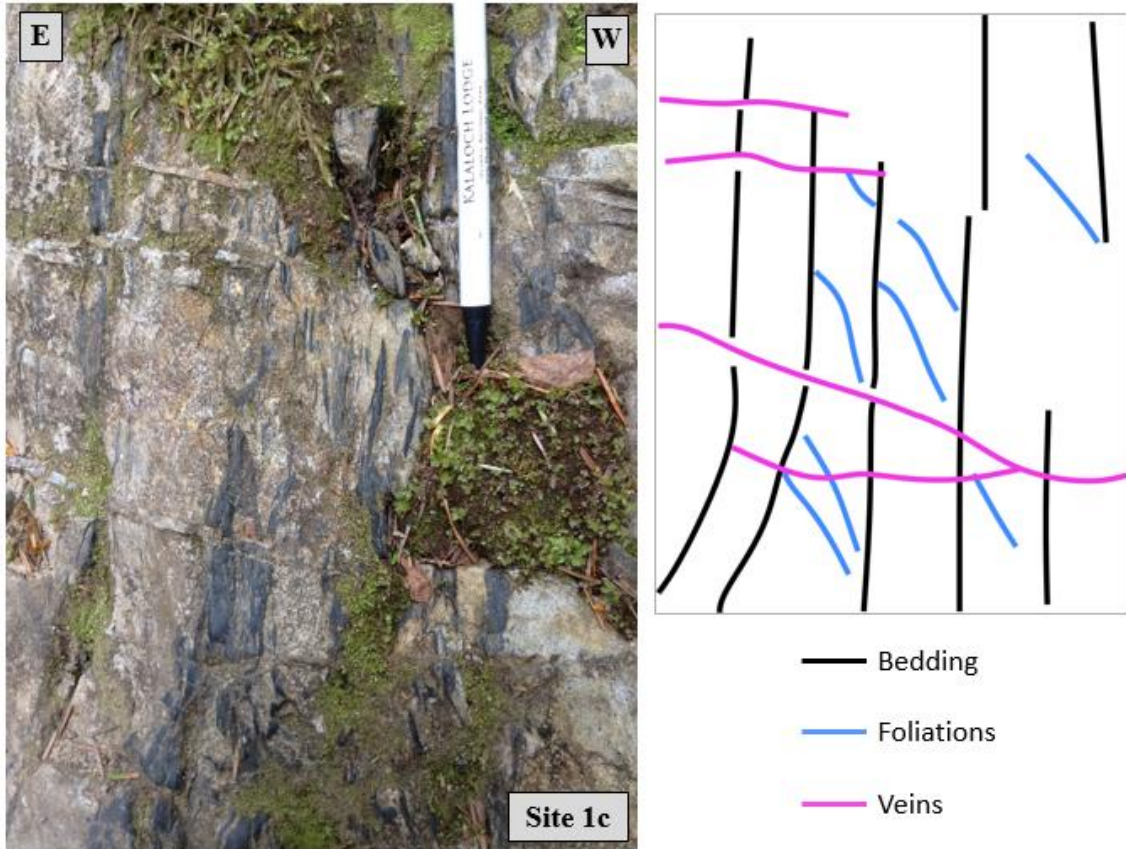
Figure 4.7. Photo of veins cutting across bedding and foliations at Site 1c (left) with an interpretive diagram (right). The photo of the near vertical outcrop was taken looking south. The pen is 15 cm long.

4.1.2 Structural Orientation Data

The bedding data show a wide range in orientations throughout the sites (**Fig. 4.8**). Sites 1a to 1d show a gradual change from N-S oriented beds to NE-SW oriented beds. In general, these beds dip steeply to the west and northwest, however in Site 1c, some dip to the southeast. Sites 1e and 1f show a larger range in orientations. Site 2a shows NE-SW oriented, steeply dipping beds, similar to Site 1b. Sites 2b and 2c also show a range in orientations that are similar to Sites 1e and 1f. The axial traces of the fold hinges on the outcrop surface were also measured and are plotted as points (red squares) along with the bedding data.

28

The foliations show less of a range in orientation, and for the most part, strike N-S and dip to the east and west (**Fig. 4.9**). There are some deviations to this trend where foliations strike NNW-SSE and NW-SE and dip to the northeast and southwest (Sites 1a, 1e, 1f, and 2a). There are also a few instances where the foliations strike NNE-SSW and dip to the northeast (Sites 1e, 1f, and 2b).

In general, the fractures range in strike from E-W to NW-SE and dip to the south and southwest or to the north and northeast (**Fig. 4.10**). There is no apparent change in fracture orientation from site to site. Most sites show the range in orientations, with the exception of Site 1a which only shows E-W oriented fractures that dip to the south. The majority of the slickenline measurements are perpendicular to the strike of the planes, with some at a smaller angle to the horizon.

Vein orientations strike NW-SE and dip to both the northeast and southwest (**Fig. 4.11**). Many veins were identified at Site 1c and strike NW-SE; most dip to the southwest but a few dip to the northeast. A couple veins were identified at Site 1e and strike NNW-SSE and dip to the WSW. Some veins were also identified at Site 1f, one strikes NW-SE and dips to the northeast, and one strikes NE-SW and dips to the northwest. Several veins were identified at Site 2b and strike NW-SE and dip to both the northeast and southwest.

Figure 4.12 shows all of the bedding, fracture, foliation, and vein data combined.
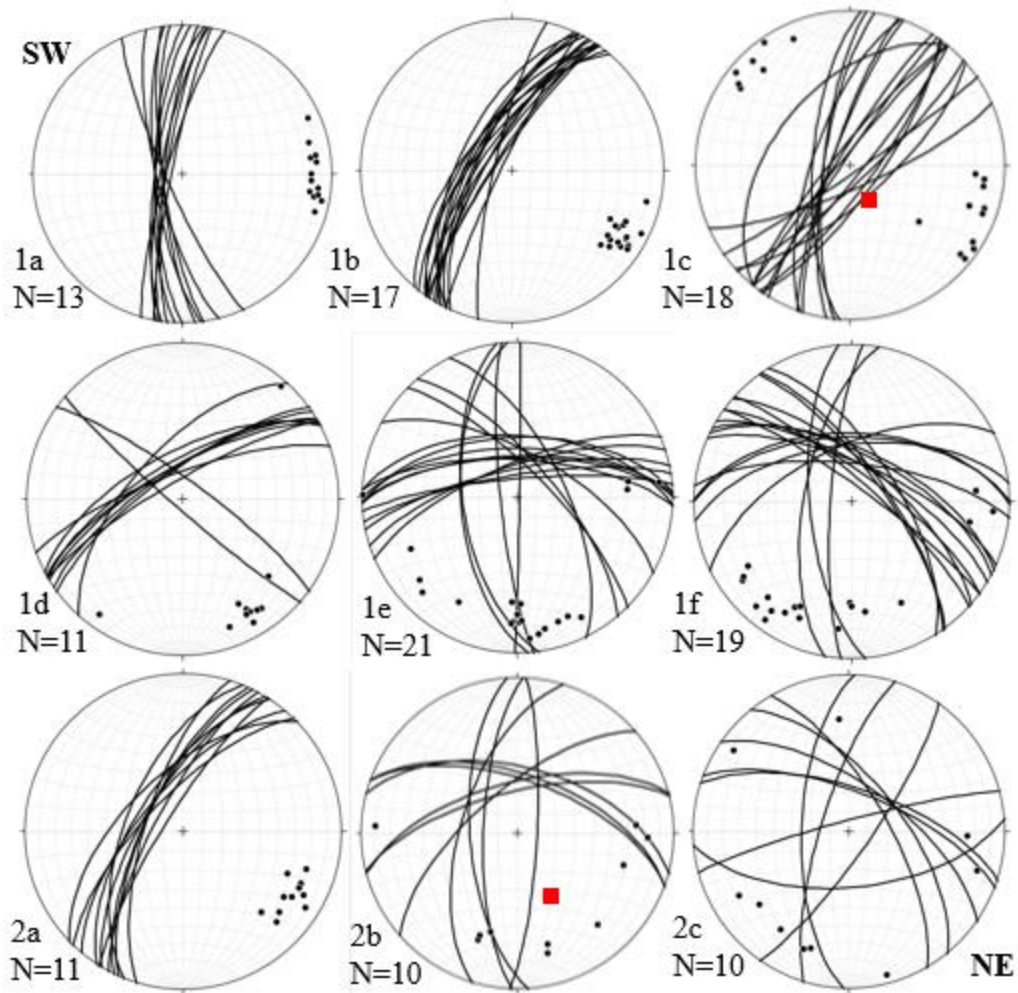
Figure 4.8. Bedding planes and poles for the meta-sedimentary units of Sites 1a-f and 2a-c and axial trace measurements of identified folds (red squares). Plots are lower hemisphere, equal area stereographic projections. N values refer to the number of measurements presented in each stereonet.
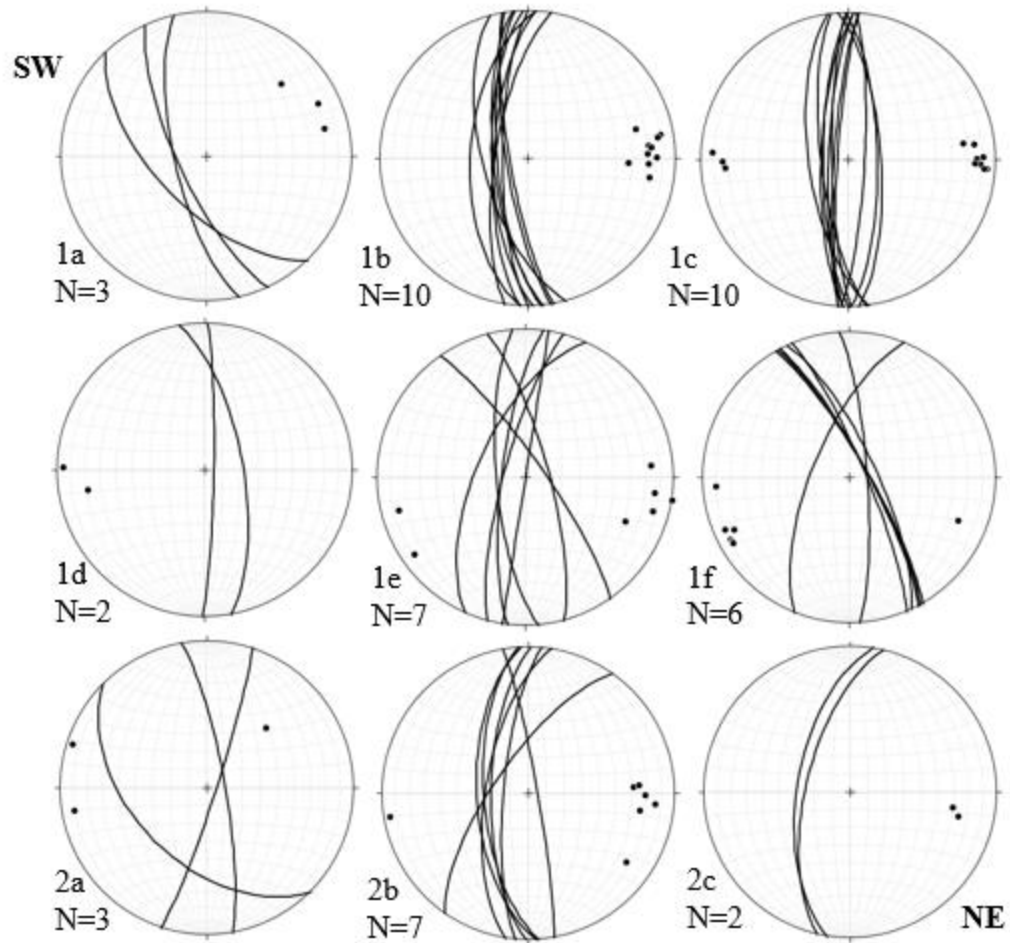
Figure 4.9. Foliation planes and poles for the meta-sedimentary units of Sites 1a-f and 2a-c. Plots are lower hemisphere, equal area stereographic projections. N values refer to the number of measurements presented in each stereonet.
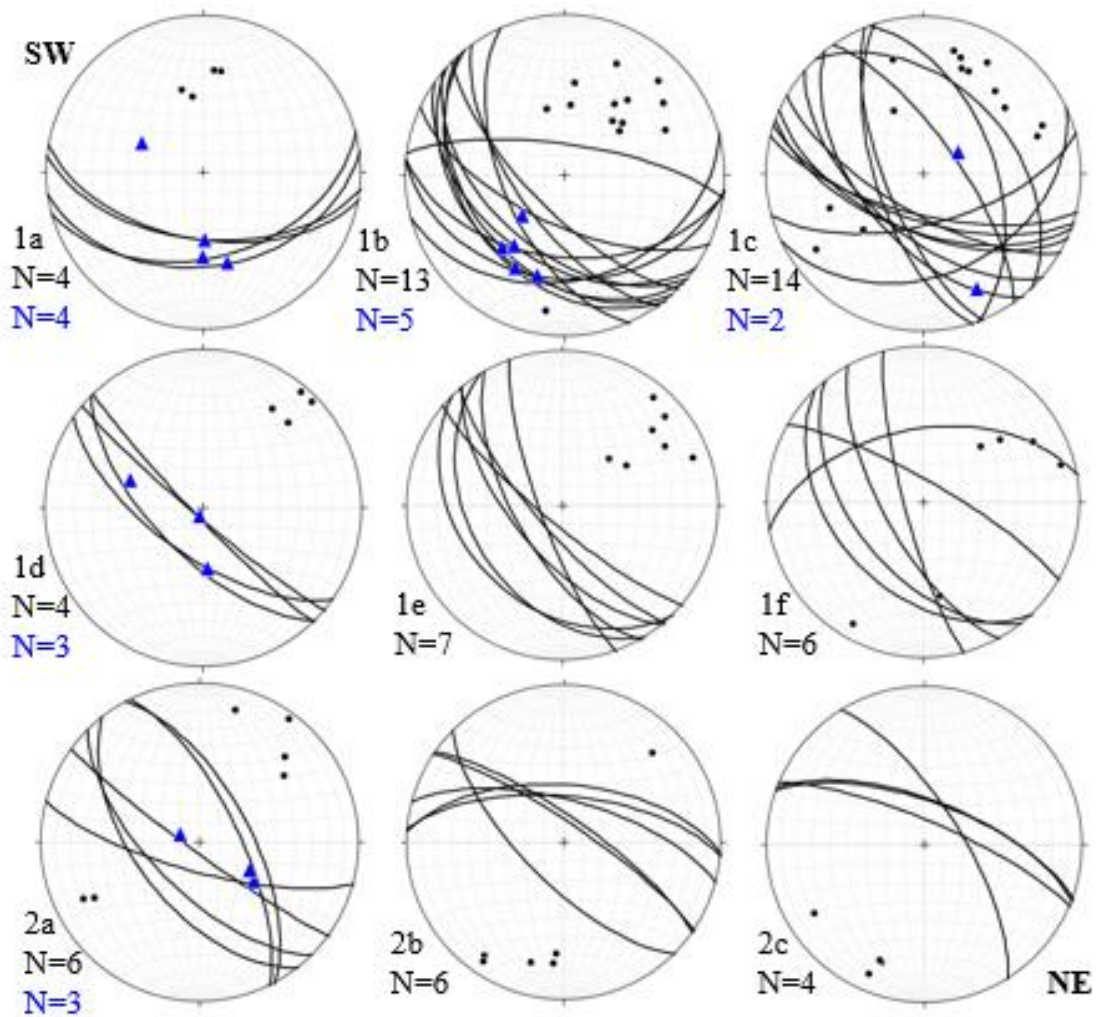
Figure 4.10. Fracture planes and poles (black lines and points) and slickenline measurements (blue triangles) for the meta-sedimentary units of Sites 1a-f and 2a-c. Plots are lower hemisphere, equal area stereographic projections. N values are for fracture measurements (black) and slickenline measurements (blue) in each stereonet.
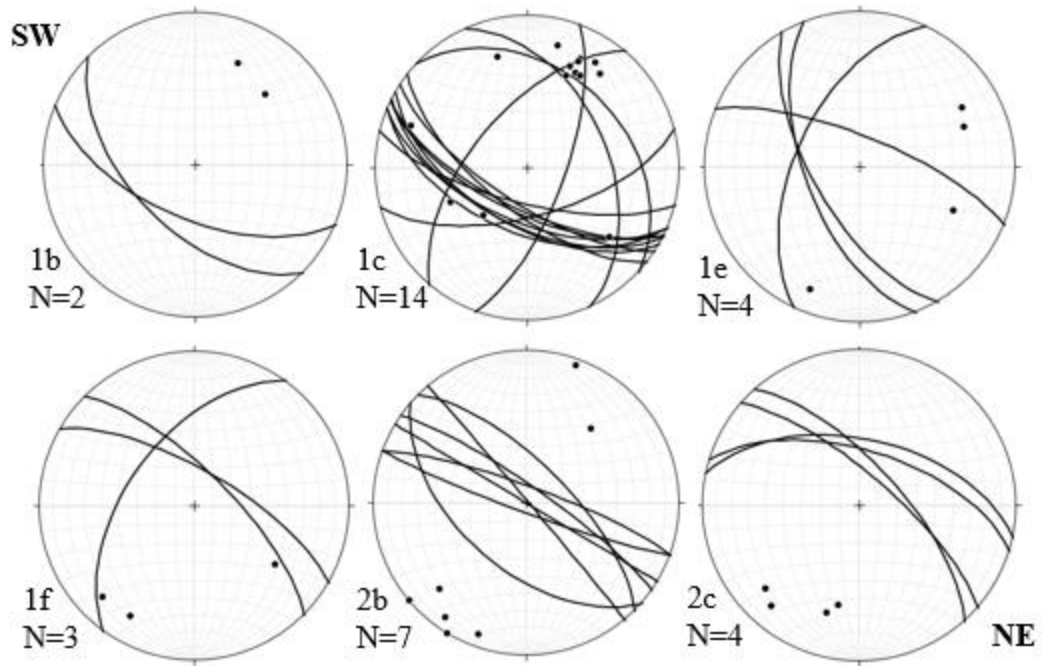
Figure 4.11. Vein planes and poles for the meta-sedimentary units of Sites 1a-f and 2a-c. Plots are lower hemisphere, equal area stereographic projections. N values refer to the number of measurements presented in each stereonet.
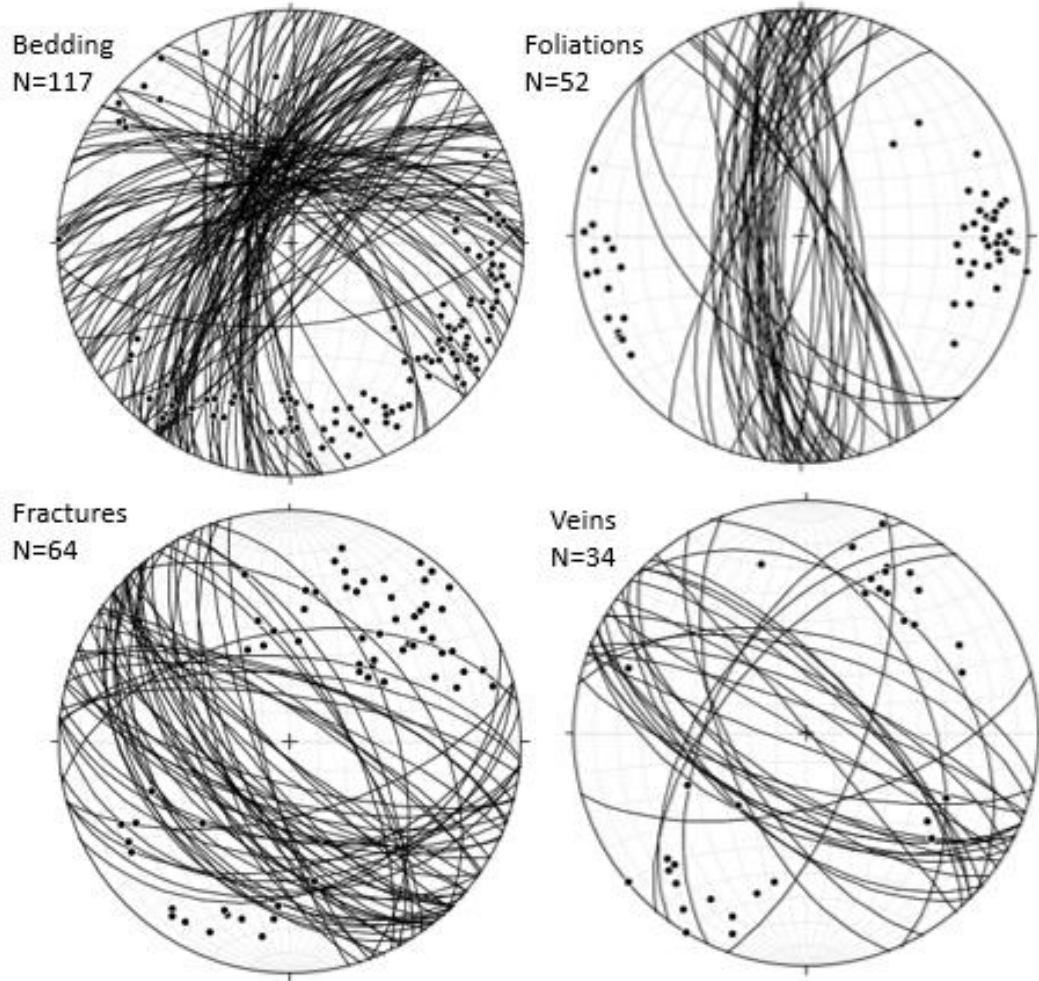
Figure 4.12. All bedding, foliation, fracture, and vein data for the meta-sedimentary units combined from Sites 1a-f and 2a-c. Plots are lower hemisphere, equal area stereographic projections. N values refer to the number of measurements presented in each stereonet.

4.1.3 Microscale Observations & Data

Two rock samples are used in this section to describe the range in disruption of the meta-sediments at the hand sample scale. As described in Section 4.1.1, the sites with more meta-sandstone appear to be less disturbed by fractures and foliations than those with more slate. Sample A (**Fig. 4.13**) is from the less-disturbed, meta-sandstone-rich sites, and Sample B (**Fig. 4.14**) is from the more disturbed slate-rich sites. A thin section from Sample B (**Fig. 4.15**) is also used to show how structures are expressed at the microscale.

At the hand sample scale, Sample A shows primary sedimentary features and secondary deformation features (**Fig. 4.13**). The sample has continuous, linear bedding of slate and meta-sandstone with primary features, such as cross beds, preserved in the meta-sandstone layers. Foliation is observed crosscutting the slate layers and is uniformly oriented throughout the sample.

Sample B shows a variety of deformational structures that disrupt primary structures at the hand sample scale (**Fig. 4.14**). The sample has discontinuous bedding of slate and meta-sandstone at a range of orientations, with some areas displaying folds. Bedding is crosscut and offset by foliations and fractures. Although they have a similar appearance at the hand sample scale, the foliation is a penetrative fabric, whereas the fractures are small, localized, and not expressed throughout the whole rock. Fractures are most confidently identified where they offset and crosscut bedding and where their orientation is similar to larger scale fractures measured at the sample site. Sample B also contains small veins that crosscut bedding and do not have a consistent orientation. These

35

veins are not expressed at the sample site, but these may be smaller versions of those that are observed elsewhere at the outcrop scale.

At the micro-scale, the primary foliation of Sample B affects both the slate and meta-sandstone layers. The meta-sandstone layers are characterized by quartz and feldspar crystals that range from 5-75 μm in diameter, and the slate layers are characterized by white and brown mica that range in size from 1-5 μm in width and 5-100 μm in length (**Fig. 4.16**). The mica grains are in a preferred orientation and form a penetrative foliation that anastomoses around the quartz and feldspar grains. This foliation is especially apparent in the slate layers, but is also expressed in the meta-sandstone layers by sparse micas. The foliation is subparallel to bedding and is termed S1. This foliation is crenulated in some places.

A secondary foliation crosscuts and disrupts the bedding parallel foliation (S1) in Sample B (**Fig. 4.17**). This foliation (S2) is also defined by aligned mica grains. The crenulations in S1 are associated with S2 in orientation and spatial relationship; where S2 crosscuts S1, S1 bends into S2.

Veins in Sample B crosscut many features in the rock and are deformed. They are composed of quartz crystals that are 50-200 μm in diameter (**Fig. 4.18**). The veins crosscut the bedding and, in places, cut S1. The veins are folded, commonly in an orientation consistent with S2. The quartz crystals also show microstructures consistent with bulging and subgrain rotation recrystallization, as described by Stipp, Stünitz, Heilbronner, & Schmid (2002) (**Fig. 4.19**). The veins observed here are not necessarily the same veins that are observed at the outcrop scale. The veins at the outcrop scale are

larger (on the order of a couple millimeters thick and up to a meter in length) and are composed of larger, blocky quartz grains.

Fractures are also observed at the micro-scale crosscutting and offsetting the bedding and foliation (**Fig. 4.20**). The fractures differ from the foliations in that they are not defined by the alignment of mica grains. They are filled with very fine grained quartz crystals, which may indicate that they are related to the veins.
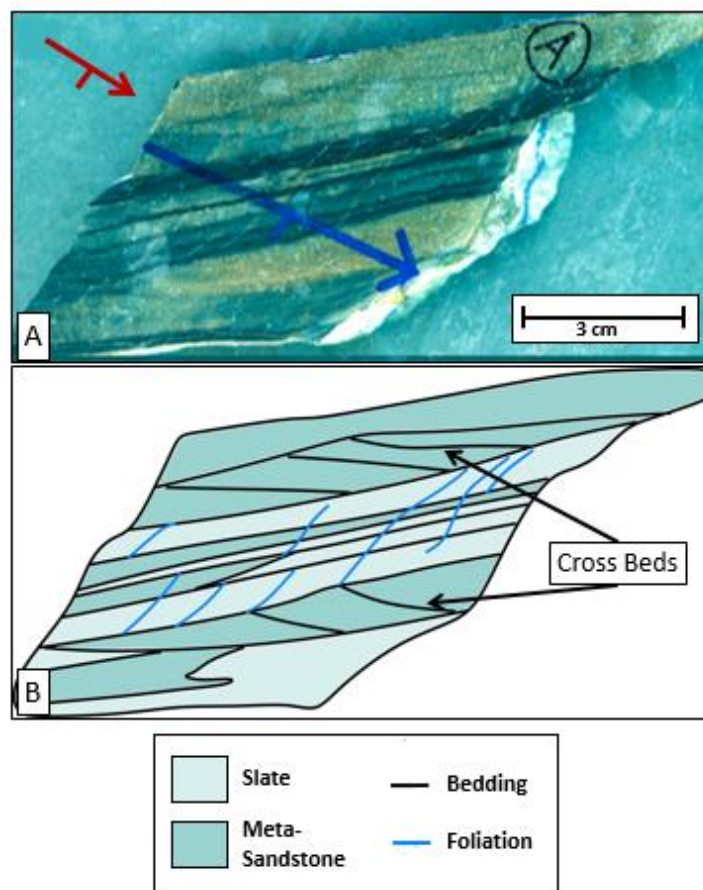
Figure 4.13. Sample A (a) and a corresponding interpretive diagram (b) that outlines structures of interest. The slab scan image shows a near cross sectional view on the plane (053, 22), as indicated by strike and dip markings. Sample A is collected from Site 1b.
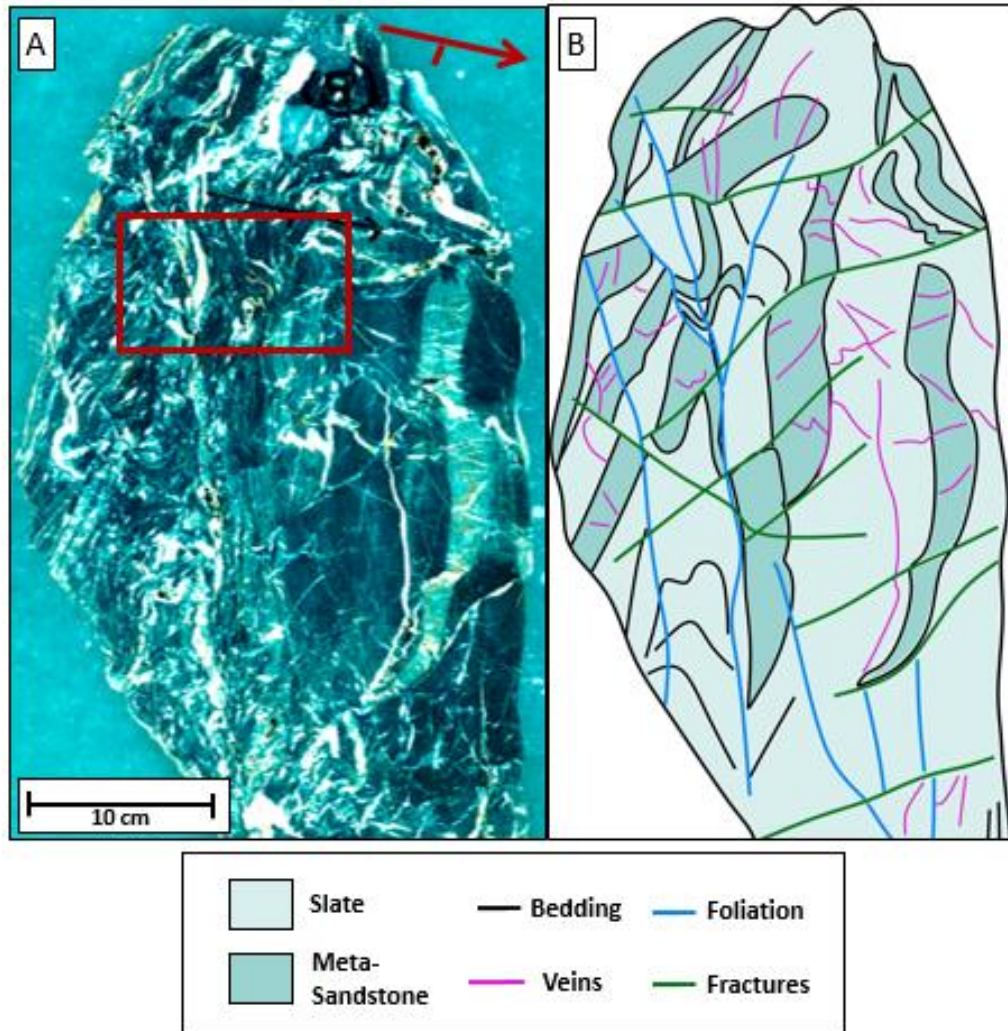
Figure 4.14. Sample B (a) and a corresponding interpretive diagram (b) that outlines structures of interest. The slab shows a near cross sectional view on the plane (071, 84), as indicated by the strike and dip markings. The red box outlines the area of the thin section shown in **Figure 4.15**. Sample B was collected from Site 1e.
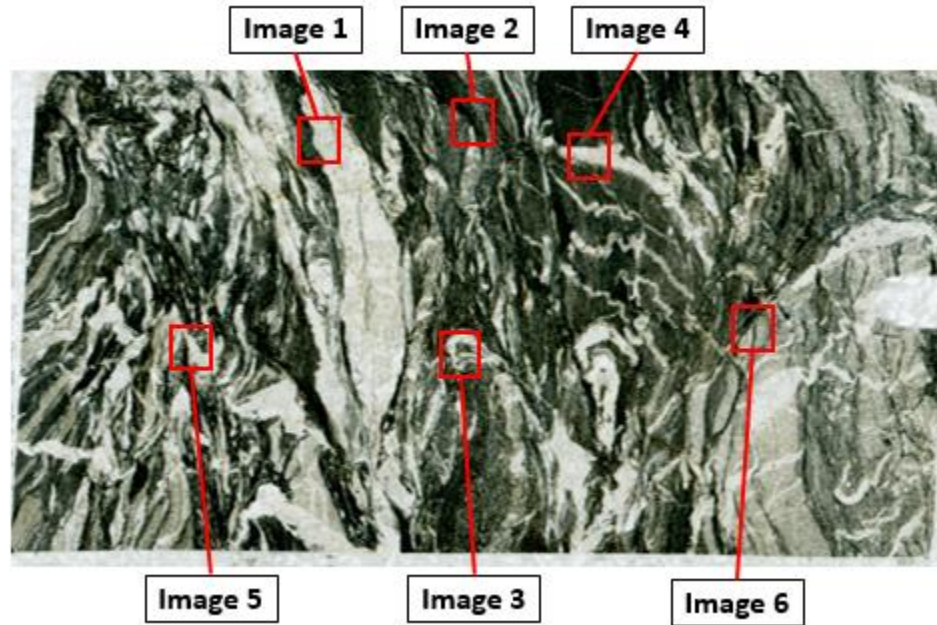
Figure 4.15. A thin section created from Sample B (red box in **Fig. 4.14**) and locations of the structures shown in Figures 4.16 to 4.20.
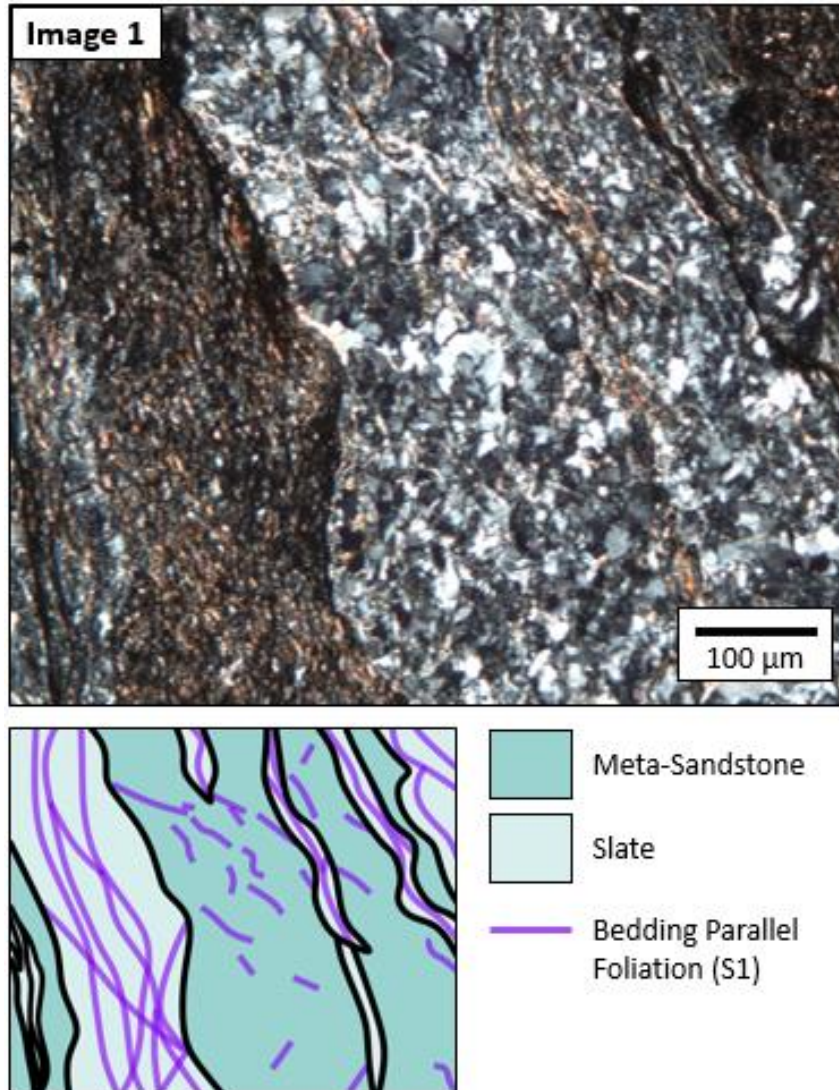
Figure 4.16. Photomicrograph and interpretive diagram of slate and meta-sandstone layers. The mica-defined foliation is subparallel to bedding. Image 1 of Sample B (**see Fig. 4.15**) in crossed-polarized light.
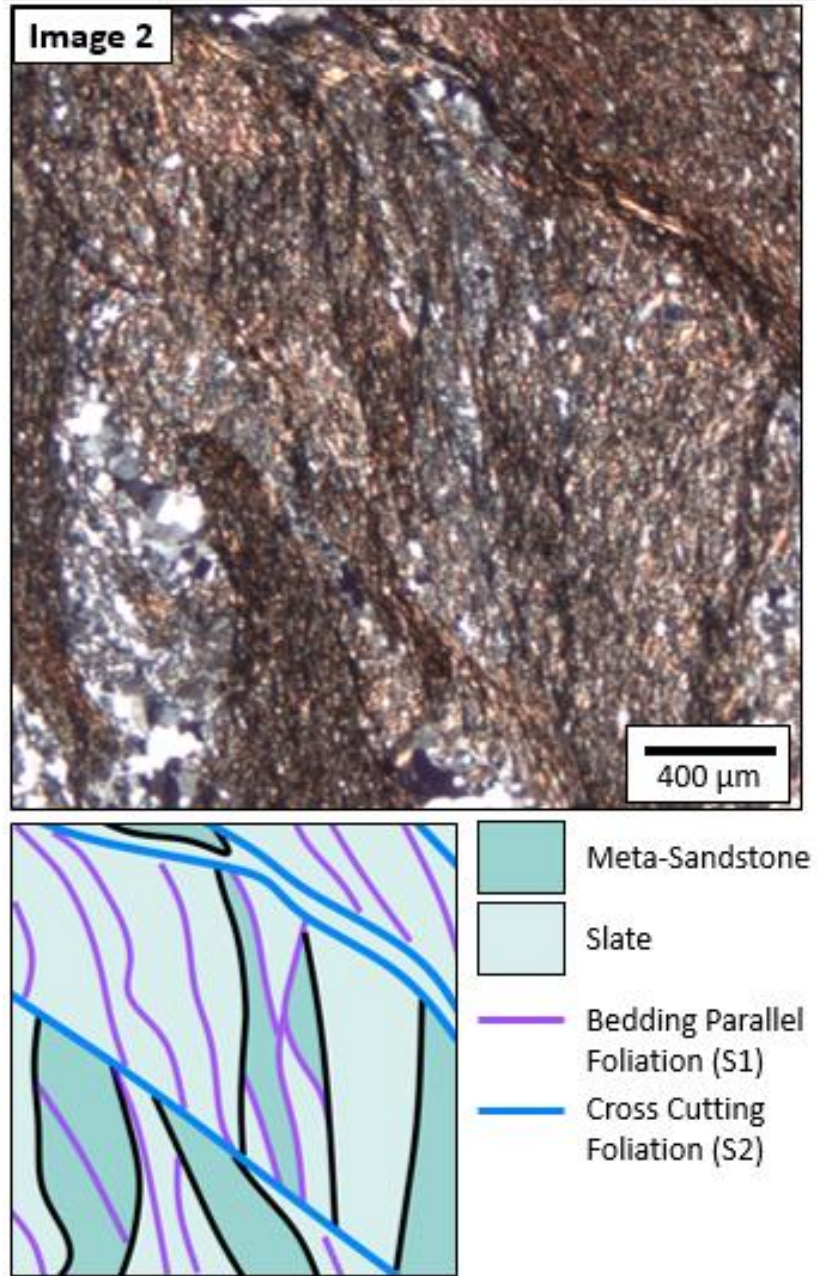
Figure 4.17. Photomicrograph and interpretive diagram of overprinting foliations in Image 2 of Sample B (see **Fig. 4.15**). A second foliation (S2) crosscuts and overprints the bedding parallel foliation (S1). Image shows cross-polarized light.
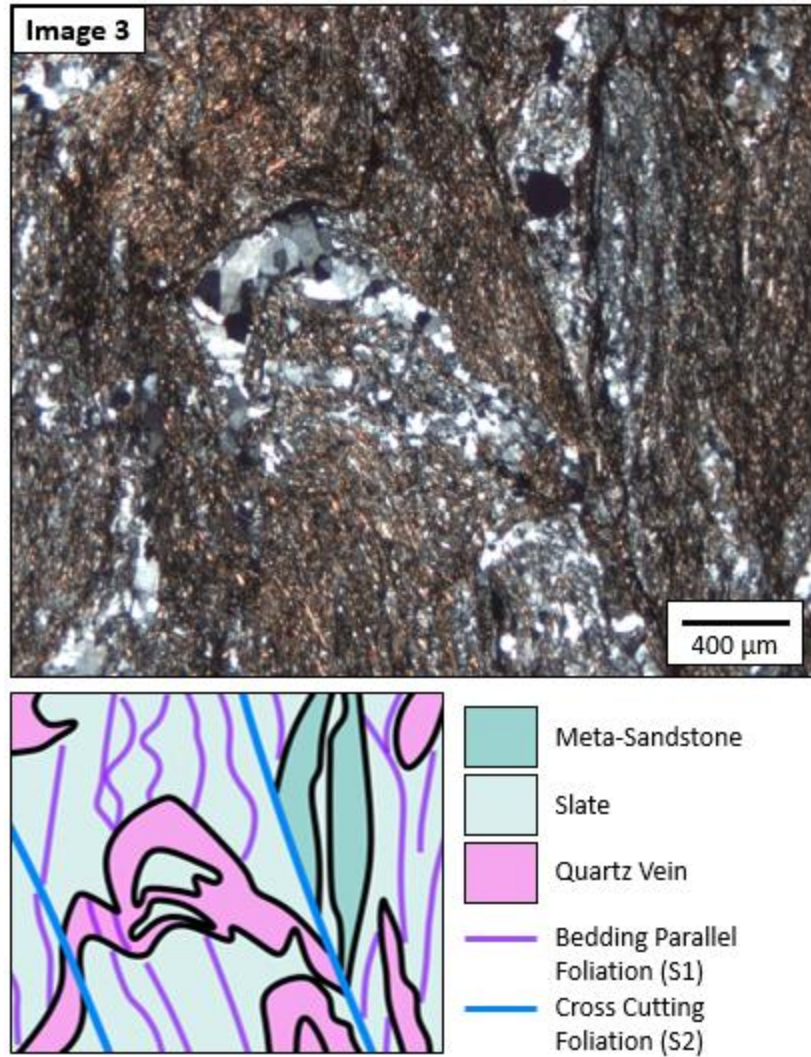
Figure 4.18. Photomicrograph and interpretive diagram of the relationship between a vein and foliation in Image 3 of Sample B (see **Fig. 4.15**). The quartz vein crosscuts S1 and is folded in an orientation that correlates with S2. Image shows cross-polarized light.
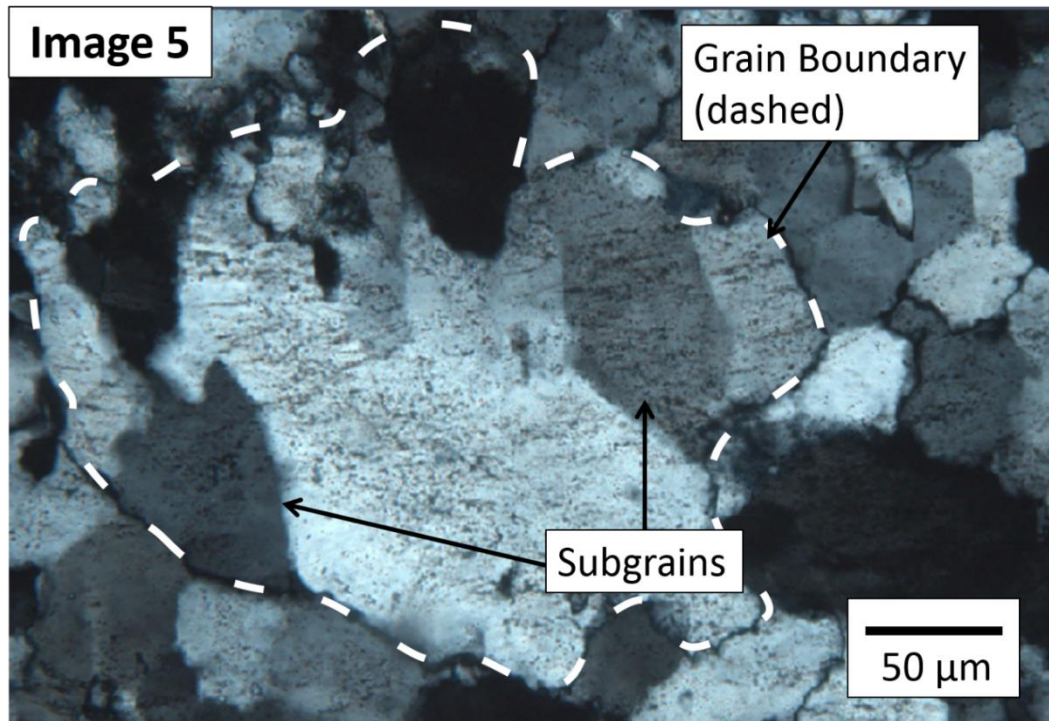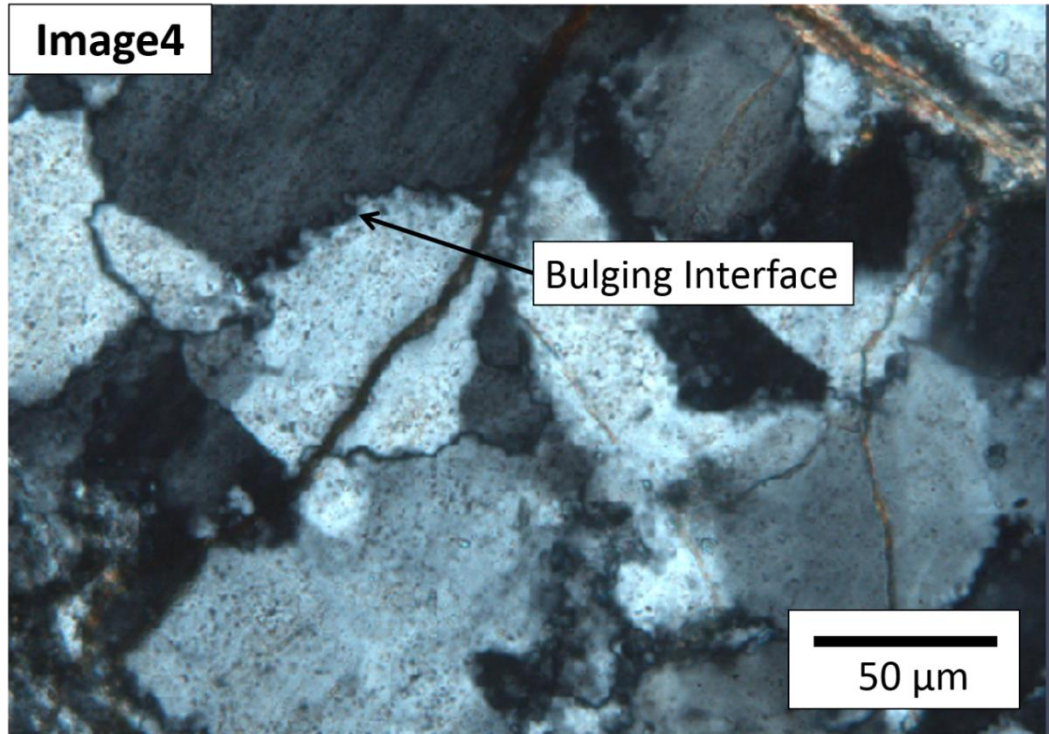
Figure 4.19. Photomicrographs of quartz microstructures in Images 4 and 5 of Sample B (see **Fig. 4.15**). Microstructures are consistent with bulging (Image 4) and subgrain rotation (Image 5) are both present. Images show cross-polarized light.
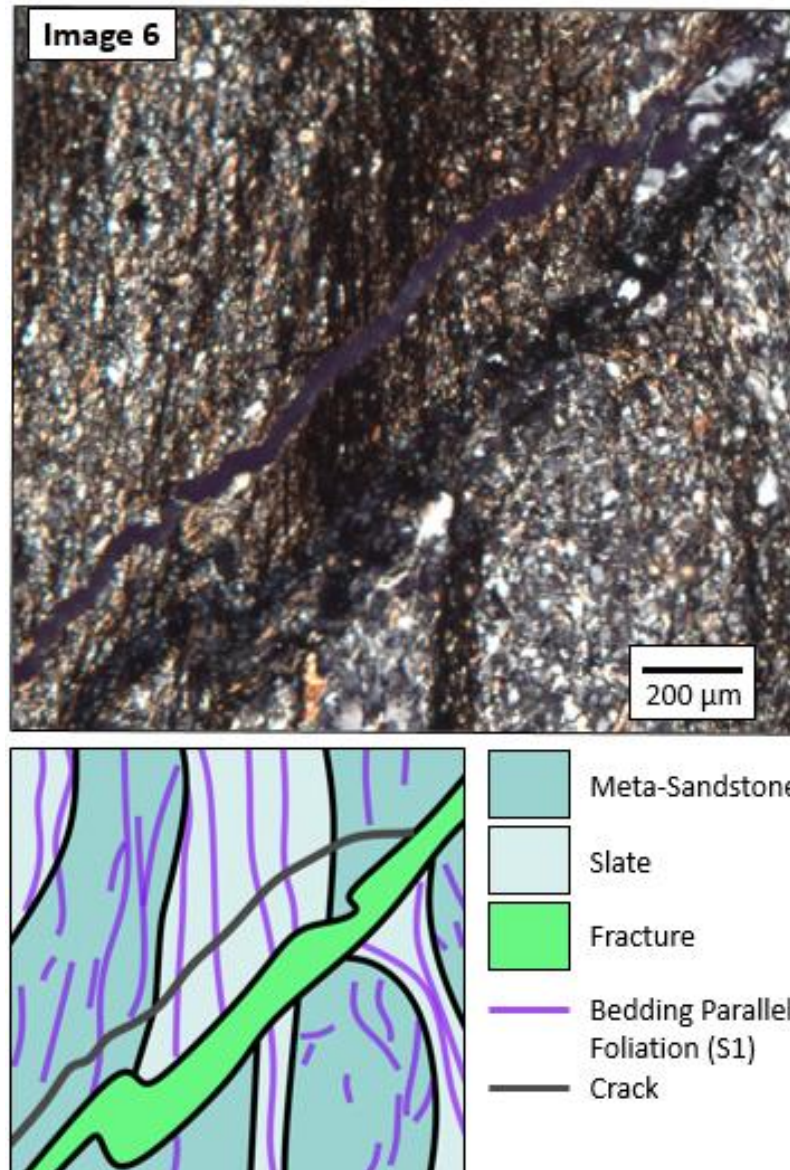
Figure 4.20. Photomicrograph and interpretive diagram of a fracture in Image 6 of Sample B (see **Fig. 4.15**). The fracture is filled with very fine-grained quartz and crosscuts S1, offsetting bedding layers. Image shows crossed-polarized light.

4.2. Interpretations

This section presents interpretations made of field observations, structural data, and micro-scale observations from the meta-sedimentary outcrops, Sites 1 and 2, of the Hamma Hamma Transect.

Sites 1a, 1b, 1c, and 1d represent a single fold, the fold hinge of which was identified at Site 1c (**Fig. 4.2**). This is supported by the progressive change in bedding orientation along these sites (**Fig. 4.8**). The pattern of bedding measurements relative to location suggest several smaller scale folds at Sites 1e and 1f. **Figure 4.21** shows where bedding measurements were taken along these sites and the interpreted fold outline. Fold hinges were not identified at these sites due to cover. Site 2 shows a similar fold pattern as Sites 1e and 1f. The bedding data from Sites 1a-1d span a similar range as the data for Sites 1e and 1f (**Fig. 4.8**), indicating that the folds are related and oriented similarly. When the poles to bedding planes from all sites are considered with the axial trace measurements, a fold axis of (69→342) and an axial plane of (337, 88) was calculated (**Fig. 4.22**). The principal stress (σ1) necessary to form these folds is oriented (02→247), ENE-WSW.

Considering the calculated axial plane, location of fold hinge, and rock type present at each site, the schematic map in **Figure 4.23** was created for Site 1. The area shows a steeply plunging, single anticline, with the hinge at Site 1c. The rocks at Site 1a are interpreted as the same layer as those at Sites 1e and 1f. The smaller scale folds at Sites 1e and 1f are interpreted as parasitic folds, which is consistent with folding in less competent slate layers.

Sedimentary layers are expected to be initially deposited horizontally, and an initial folding is expected to be upright with some shallowly dipping beds and a horizontal fold axis. This is not what was observed in the study area, suggesting that folds were rotated into their current position. The axis of rotation necessary for this process is

(00→073) with a magnitude of 69° counterclockwise, and the σ1 necessary for this rotation is oriented NNW-SSE. **Figure 4.24** shows the poles to bedding data and an interpretation of how the data would look if it was rotated to put the folds in an upright orientation.

Two foliations were identified at the microscale, S1 and S2. S1 is bedding parallel, and I interpret it to have formed from compression due to the burial of the sediments. S2 overprints S1 at the microscale (**Fig. 4.17**), however, at the hand sample scale, the two foliations are undistinguishable from one another (**Fig. 4.14**). It is unclear whether both foliations are expressed at the hand sample and outcrop scale or if only S2 is apparent and measureable. Since S1 appears bedding-parallel, if it was formed from burial rather than folding, it would have been folded with the bedding and would show a range in orientations, similar to the bedding data. The foliation measured at the outcrop scale strikes pretty consistently N-S and is not similar to the beds, so therefore, I interpret the foliation measured at the outcrops as the S2 observed in thin section. A more detailed microscale analysis with a wider range of samples from around the map-scale folds would be required to determine the timing and relationship among the microscale S1 and S2, the outcrop-scale foliation, and the outcrop-scale fold data.

The fold and foliation data do not support the interpretation that the outcrop-scale foliation measurements formed axial planar to the folds. If the folds and foliation formed under the same state of stress, then the axial plane should be parallel to the foliation. This is not the case for the foliation measured in outcrop (S2) and the calculated axial plane from bedding data (**Fig. 4.25**). The foliation has a range of orientations that center around

46

a N-S strike, whereas the axial plane strikes NNW-SSE. There are several possible explanations for this discrepancy. There may have been a component of shear in which the σ1 is oriented at an angle to the foliation and the folds are drag folds associated with strain partitioning on shear planes. This would indicate that the folds and foliation may have formed under the same state of stress. Alternatively, it may be that the foliation formed later than and overprints the folds, and therefore the two are not related.

Orientation data and microscale observations support the interpretation that the fractures and veins are genetically related. The fractures and veins have similar orientations throughout the outcrops (**Fig. 4.26**), and at the micro-scale, the fractures appear as very fine-grained quartz, indicating mineralization (**Fig. 4.20**). Because of this, I interpret the veins to represent mineralized Mode II fractures rather than Mode I fractures. When the data for the fractures and veins are combined, two groups stand out with representative orientations: Group A (115, 61) and Group B (303, 76) (**Fig. 4.27a**).

The orientation of combined fracture and vein groups are consistent with the interpretation that they are conjugate fractures. The maximum principal stress (σ1) for these conjugates would be (76→254), which is nearly vertical (**Fig. 4.27a**). If the assumption of conjugates is correct and if they formed in their current orientation, this suggests a normal motion. The slickensides, however, indicate that the last motion on the fracture planes was reverse (i.e., smooth up dip on the footwall side). One interpretation for this relationship is that the state of stress changed to account for the change in slip direction. This interpretation is not preferred because it is not consistent with a

convergent plate setting. Another interpretation is that the fractures actually formed with a reverse geometry and were then rotated into their current position.

If both the fractures and folds have been rotated and the rotation occurred after both structures formed, then it is possible that the same degree of rotation from the fold data could be applied to the fracture data. When the fracture groups are rotated about the same rotation axis calculated for the folds ([00→073] with a magnitude of 69°, counterclockwise) an initial σ1 of (21→178) (N-S) is calculated (**Fig 4.27b**). This state of stress is sub-perpendicular to the strike of the interpreted axis of rotation and therefore could be the driving force for the rotation.

I propose two stages of deformation throughout the rocks' history, with two different states of stress. The first stage had a σ1 oriented ENE-WSW or E-W which formed the folds and foliation (S2). It is unclear if the folds and foliation formed during the same event or if the foliation overprints the folds, however, it is possible that they formed under a similar state of stress. The second stage had a σ1 oriented N-S or NNW-SSE, which formed the fractures and caused the rotation of the folds and fractures into their current orientation.
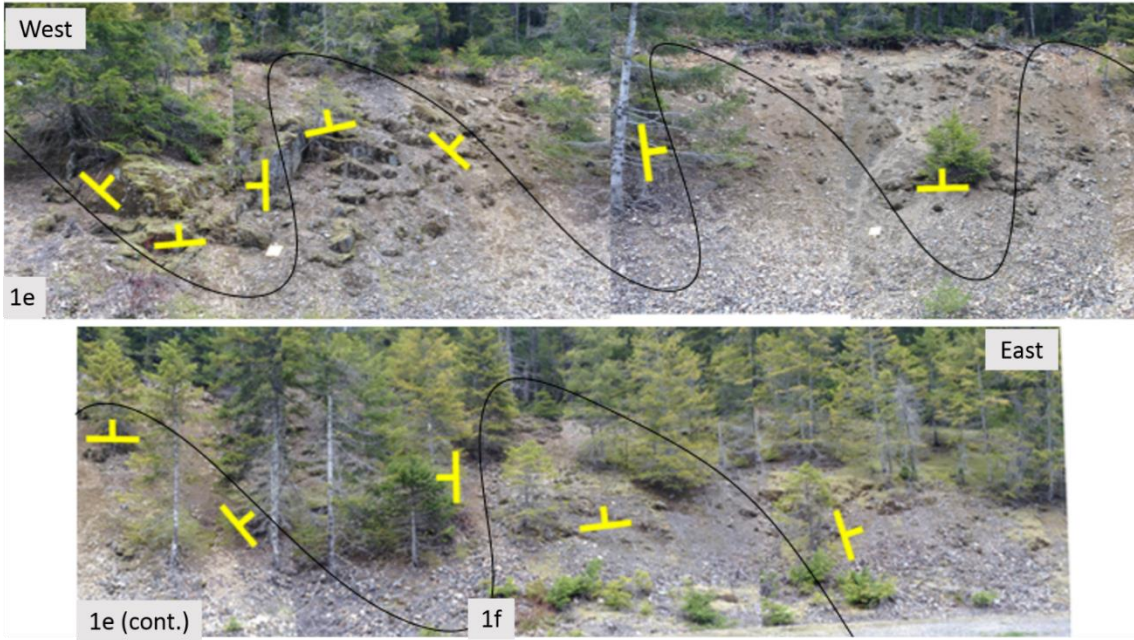
Figure 4.21. Outcrop map of Sites 1e and 1f showing the locations of strike and dip measurements and an interpreted fold line.
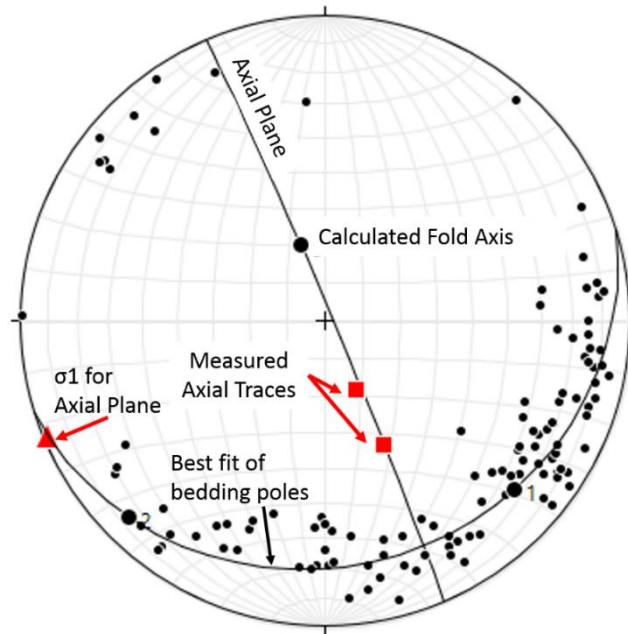
Figure 4.22. Poles to all bedding planes with a cylindrical best fit plotted. The pole to the cylindrical best fit is the calculated fold axis (69→342). The line through the fold axis and the measured axial traces (outlined in Fig. 4.4) is the calculated axial plane (337, 88). The pole to the axial plane is the principal stress (σ1) that formed the folds (02→247).
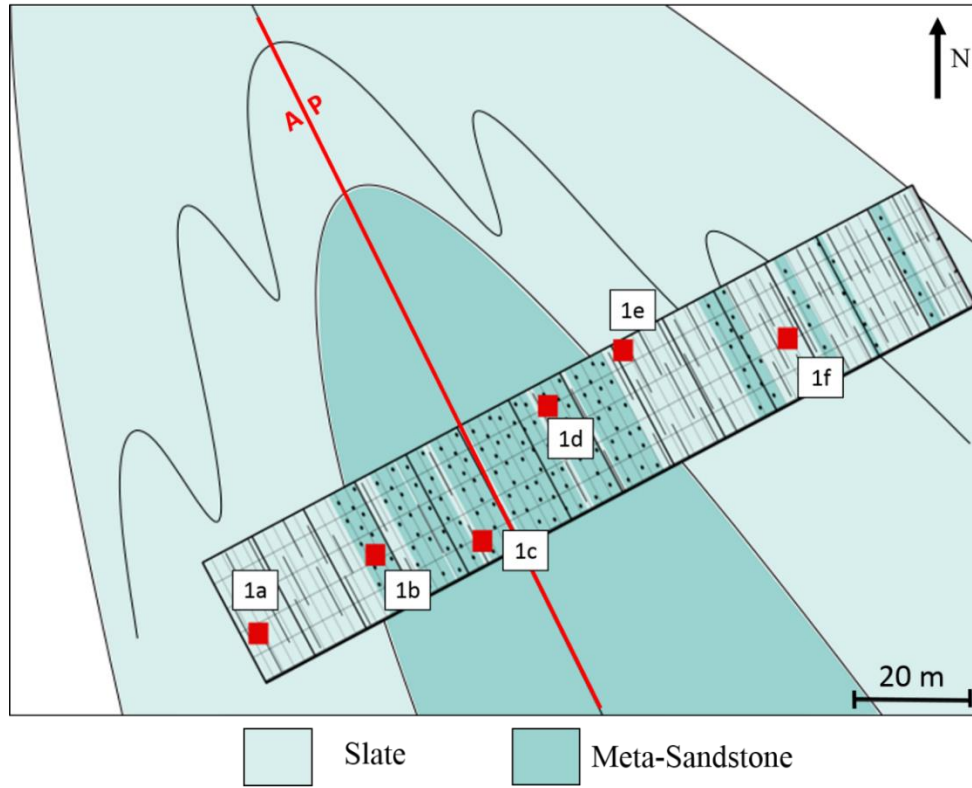
Figure 4.23. Schematic geologic map of Site 1 along the Hamma Hamma Transect. The area is interpreted as one single fold with parasitic folds in the slaty layers of the fold limbs.
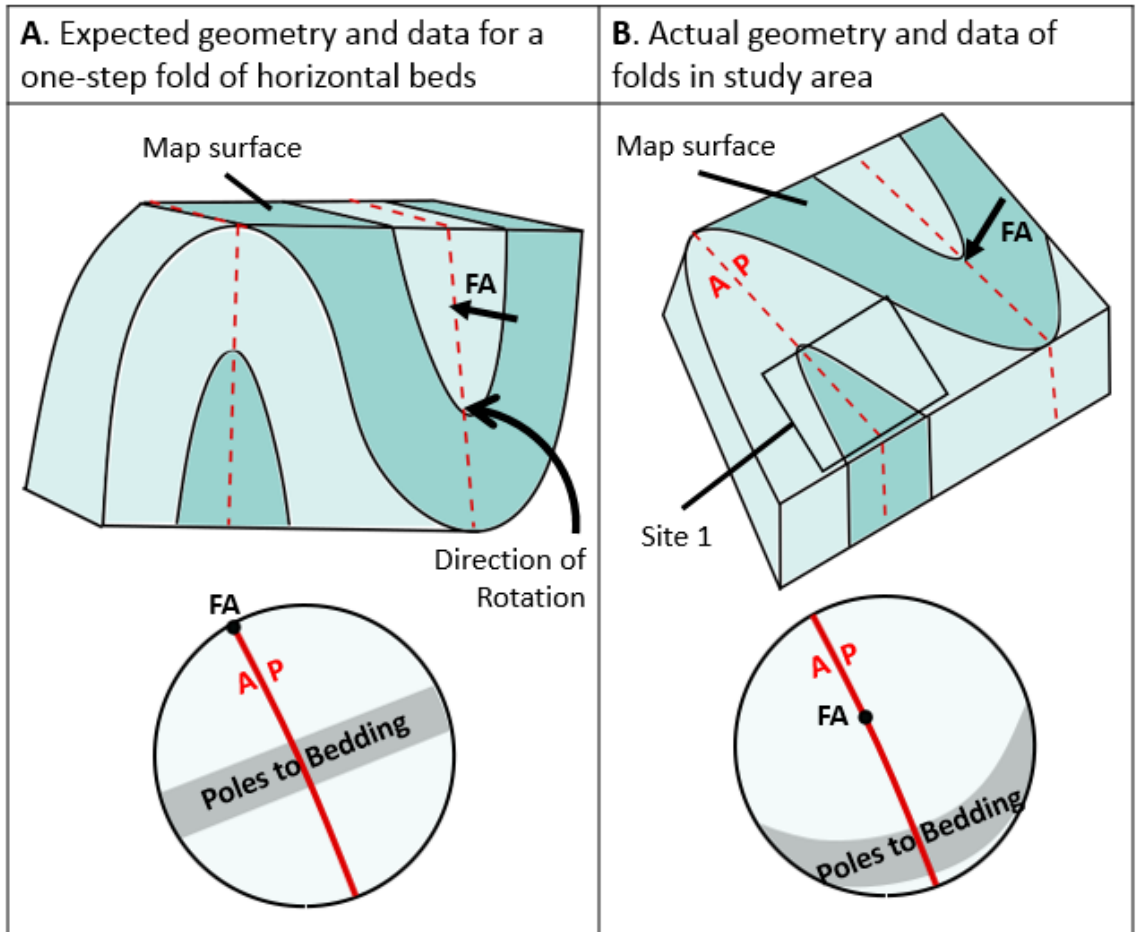
Figure 4.24. 3-dimensional block diagrams and stereographic projections for the current state of the meta-sedimentary folds (b) and if the fold were backrotated to an upright orientation (a). If the folds started in an upright orientation, the geometry in (a) would be 'time 1' and the geometry in (b) would be 'time 2'. The strike of σ1 required for this rotation is interpreted as striking NNW-SSE.
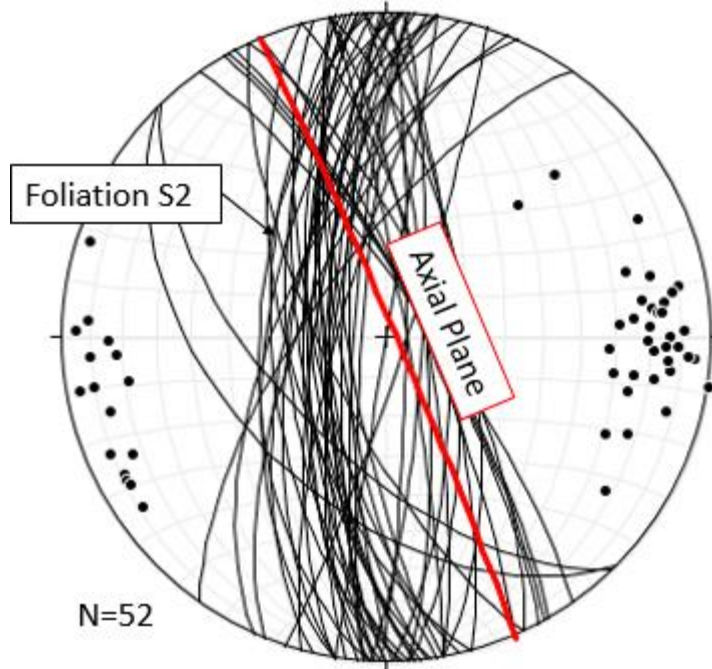
Figure 4.25. The meta-sedimentary foliation data compared to the calculated axial plane from the bedding data. The data shows that the foliation ranges around N-S striking and steeply dipping planes, which is not parallel to the axial plane as expected.
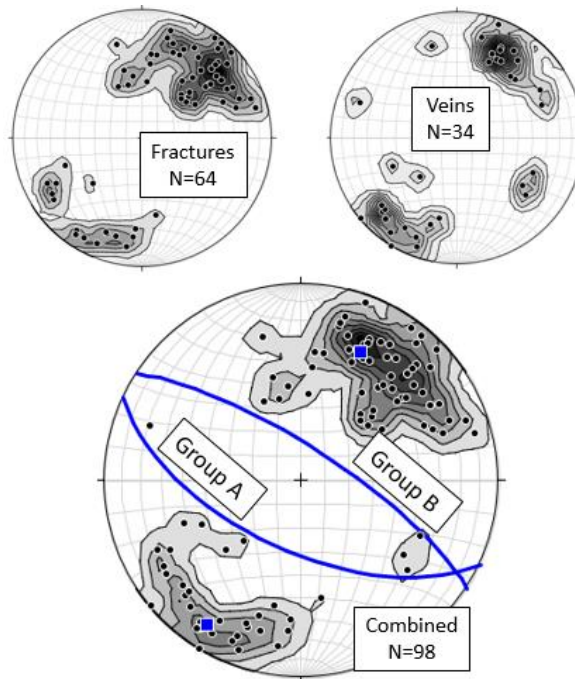
Figure 4.26. Poles to planes of the fracture and vein data from the meta-sedimentary sites. Fracture and vein data are show separately (above) and combined (below). Stereographic projections are lower hemisphere with 1% area contours. The blue boxes indicate the midpoint two data groups in the combined populations, and the blue lines show the plane to the representative midpoints.
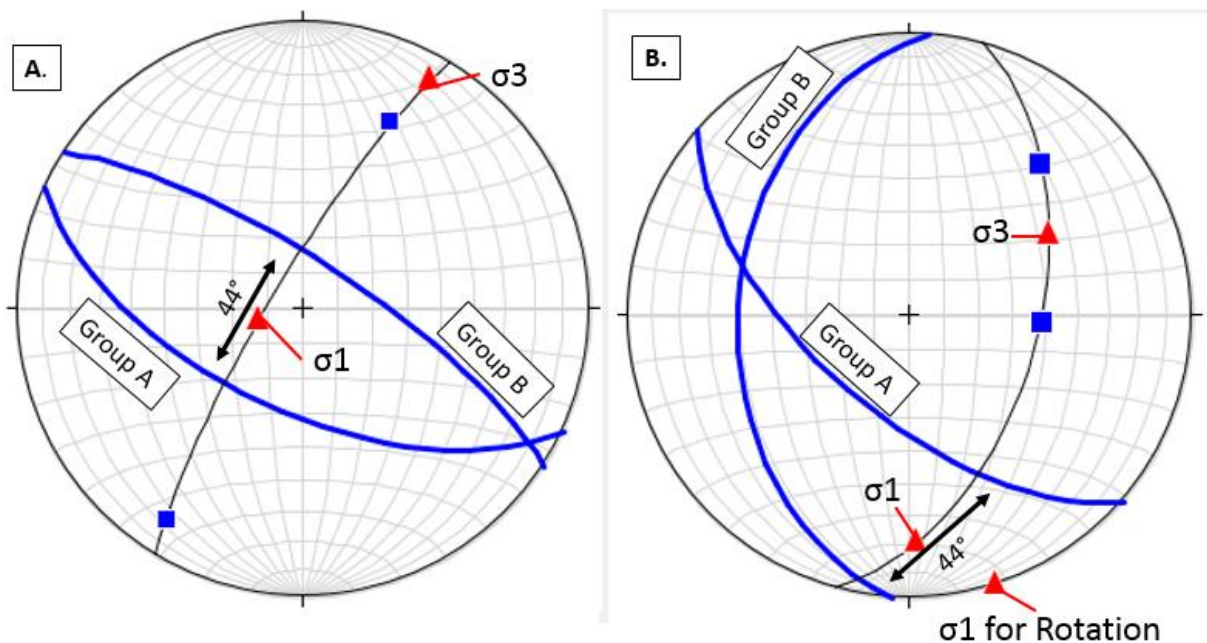
Figure 4.27. The representative orientations and state of stress for the current orientation (a) of fracture groups A and B and for the rotated state (b). (a) shows the interpreted state of stress if the groups are conjugate fractures (σ1: 76→256; σ3: 10→029). The fractures are rotated (b) about the same axis as the folds [(00→073) 69°, counterclockwise] for a historical state of stress (σ1: 21→178; σ3: 42→060). The approximate σ1 for the rotation is also plotted.

4.3. Model of Deformation

Based on the interpretation of the field observations, structural data, and micro-scale analysis of the meta-sedimentary sites along the Hamma Hamma Transect, the following is one proposed model for the deformational history of the rocks. The stages in the deformational history are denoted by T1-6 and refer to **Figure 4.28**.

The rock units were first deposited on the ocean floor as horizontal layers of sediments and then buried and compacted by subsequent deposition (T1). The overburden of burial and being at depth initiated metamorphism of the sediments; the muddier layers

became slate and the sandier layers became meta-sandstone (T2). This is when foliation S1 formed in the slate layers, subparallel to bedding.

These rock packages were then accreted to the North American continent at the Cascadia subduction zone. The regional state of state of stress was compressive, with a σ1 oriented E-W and σ3 oriented vertically. The rocks were at a depth where ductile processes dominate and responded to the stress by folding (T3). The σ1 calculated for the folds, (02→247), is not perfectly E-W, which could be due to the subsequent rotation, or the continent not being completely straight (e.g. if rocks are accreted into an embayment). Nonetheless, the folds are considered to have formed at depth by the E-W compression of the subduction zone. Foliation S2 also formed at a depth where ductile processes dominate as a penetrative fabric in response to the E-W compression. It is not clear if the foliation and folding are related.

After the folding, there was a change in the state of stress, and σ1 became more NNW-SSE or N-S oriented. The rocks must have been exhuming during this time (or perhaps the exhumation was caused by the change) because the fracture network formed under this state of stress and under conditions where fracturing dominated over folding (T4). The NNW-SSE or N-S stresses also caused the rotation of the rocks about the calculated axis of rotation into their current orientation (T5 & T6). While it is not clear when the fractures formed relative to the rotation, I interpret that the fractures formed before the rotation and that the same state of stress caused the rotation.

Time	Explanation	Illustration
T1	Layers of mud and sand are deposited in horizontal layers.	
T2	Layers are compacted by burial; metamorphism begins and foliation S1 forms in slate layers, parallel to bedding.	
T3	Layers are folded by a σ1 oriented WSW-ENE (axial plane shown by red dashed lines) at a depth where more ductile processes dominate. Foliation S2 (blue solid lines) also forms and may or may not be related to the folding.	
T4	A change in the stress regime to a σ1 oriented N-S occurred forming the fracture network (green lines). This happened at a depth where more brittle processes dominate.	

T5	A σ1 oriented more NNW-SSE causes the rocks to rotate 69° counterclockwise about an axis of rotation oriented (00→073) into their current position.	
T6	Exhumation brings the rocks to the surface, during or after their rotation. Structures have present orientation.	

Figure 4.28. Stages in the deformational history of the meta-sedimentary rocks from the Hamma Hamma Transect Sites 1 and 2. Diagrams are not to scale.

5. Pillow Basalts of the Hamma Hamma Transect

5.1 Data & Observations

5.1.1 Field Observations

Sites 3 and 4 are in the Crescent Formation, east of the HRF, and are characterized by tall outcrops of subvertical pillow basalt. The structures of interest are bedding, faults, fractures, veins, and interbedded meta-sedimentary layers.
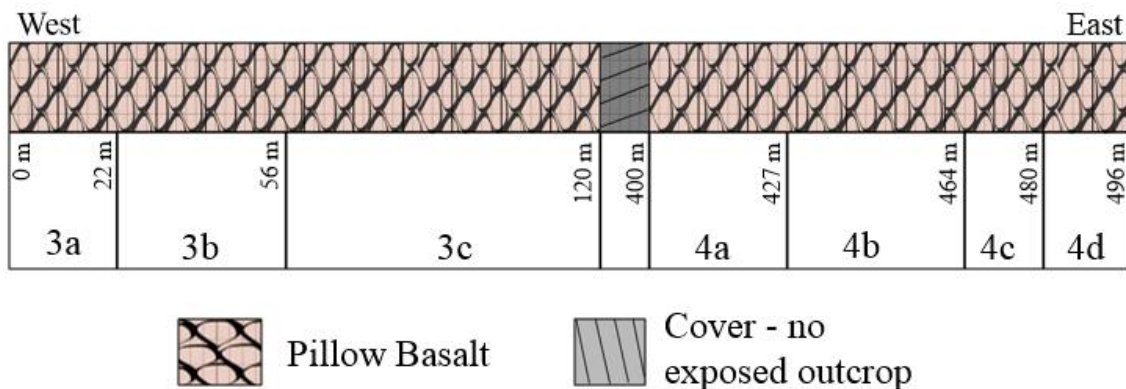
Figure 5.1. Diagram of Sites 3 and 4 showing the length of and rock type present at each subsite. The major lines of division on the column represent 10 m. Site 3a begins at the far west side of outcrop Site 3, which represents "zero", and the numbers indicate how far a subsite is from this point. The column is not continuous; there is approximately 280 m of cover between the two sites.

Pillow basalts are elongate tubes that form by underwater volcanism. The outcrops in this study expose a surface approximately perpendicular to the long axis of these tubes, exposing them as a cross section. The most convex side of the pillow basalts indicates the up direction at the time of deposition and defines bedding. At the study sites, the convex sides are steeply-dipping to vertical and face east (**Fig. 5.2**).

Nine faults were identified in the field with varying levels of confidence, as outlined in **Table 5.1.** These faults are grouped based on the level of confidence as well

as their orientation (see Section 5.1.2). Four faults were identified at Site 3a, two faults at

Site 3b, and one fault was found at each of the remaining sites (i.e., Sites 4a, 4b, and 4c).

No faults were identified at Sites 3c or 4c. The location of each fault is shown in **Figure**

5.3. Faults are expressed as continuous planes that cut across the outcrops (**Fig. 5.4**),

show offset, and have measureable slickenlines. Some faults show evidence for

comminution in the form of fault gouge and cataclasite (**Fig. 5.5**). Offset is inferred

because individual pillows cannot be traced across the faults. The amount and sense of

offset is difficult to determine because there are no clear piercing points. The slickensides

(**Fig. 5.6**) are smooth down dip on the footwall side of the fault plane, indicating that the

footwall moved up relative to the hanging wall (i.e., normal motion).

Table 5.1. Description of confidence levels for identifying fault groups in the pillow basalt outcrops.

Confidence Level	Description	Group(s)
High - 5/5	Faults clearly cut through the outcrop, offset pillows, have measureable slickensides, and show evidence for comminution	A
Moderately High - 4/5	Faults clearly cut through the outcrop, offset pillows, have measureable slickensides, but show no evidence for comminution	B & C
Moderate – 3/5	Faults cut through the outcrop, but strike subparallel to the outcrop and are difficult to discern; offset is not observed but inferred by slickensides on the fault surface; no evidence for comminution	D

The pillow basalt outcrops also have many fractures, semi-continuous cracks that do not show offset or slickensides (**Fig. 5.7**). The fractures cut across the pillows but do not span the whole outcrop like the faults; they cut across smaller pillows and terminate against larger pillows. Two distinct fracture orientations are identifiable in outcrop, referred to here as Group A and Group B. Group A appears to dip to the east, and Group B appears to dip to the west. The fracture groups have a mutually cross-cutting relationship in which they terminate into one another (**Fig. 5.7**). The fractures are relatively evenly distributed across the outcrops and between sites.

Veins are present in the pillow basalts that are contained within the pillows and that cross-cut the pillows. Veins that are contained within the pillows are small, thin, irregular, and splay radially. Larger veins cut across the pillows and are composed of calcite and quartz (**Fig. 5.8**). These veins are generally linear allowing for orientation measurements, but sometimes they are more irregular. They are not distributed evenly throughout the outcrops, some are solitary veins that cut the outcrop (spaced on the order of 10s of meters) and others occur as localized clusters. At Site 3c, there is a 3 m zone that is relatively rich in veins (**Fig. 5.9**). The cluster of veins at Site 3c is cross-cut by fractures.

Meta-sedimentary material originating from fine-grained, calcareous mud are interlayered with the basalt (**Fig. 5.10**), as first described by Garrison (1972 & 1973). The layers are not planar; they follow the bedding planes of the pillows. Where present, this material fills the spaces around pillows, and in some places, fragments of pillow

basalt are incorporated into this material. In general, it is green at Site 3 and pink at Site

4. This meta-sedimentary material is crosscut by the veins and the fractures.

Figure 5.2. Photo of pillow basalt bedding. The most convex side of the pillows (outlined in black dashed lines) defines bedding. Rock hammer is 36 cm long. Photo was taken at Site 4d of a subvertical outcrop facing north.
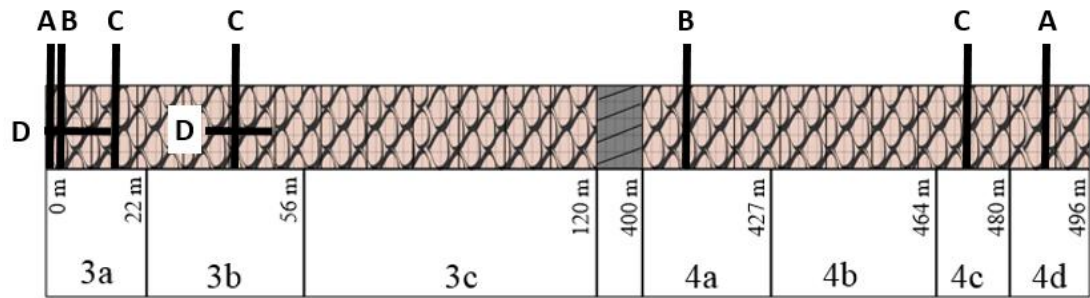
Figure 5.3. The location of each fault observed in outcrop along the west to east transect. Fault Groups A, B, and C are shown as vertical lines because their strikes are at an angle to the face of the outcrop. Fault Group D is shown as a horizontal line because it strikes parallel to the outcrop.

Figure 5.4. Photo of a fault plane at Site 4c. Photo is of a cliff outcrop facing northeast, and the notebook is 30 cm tall.
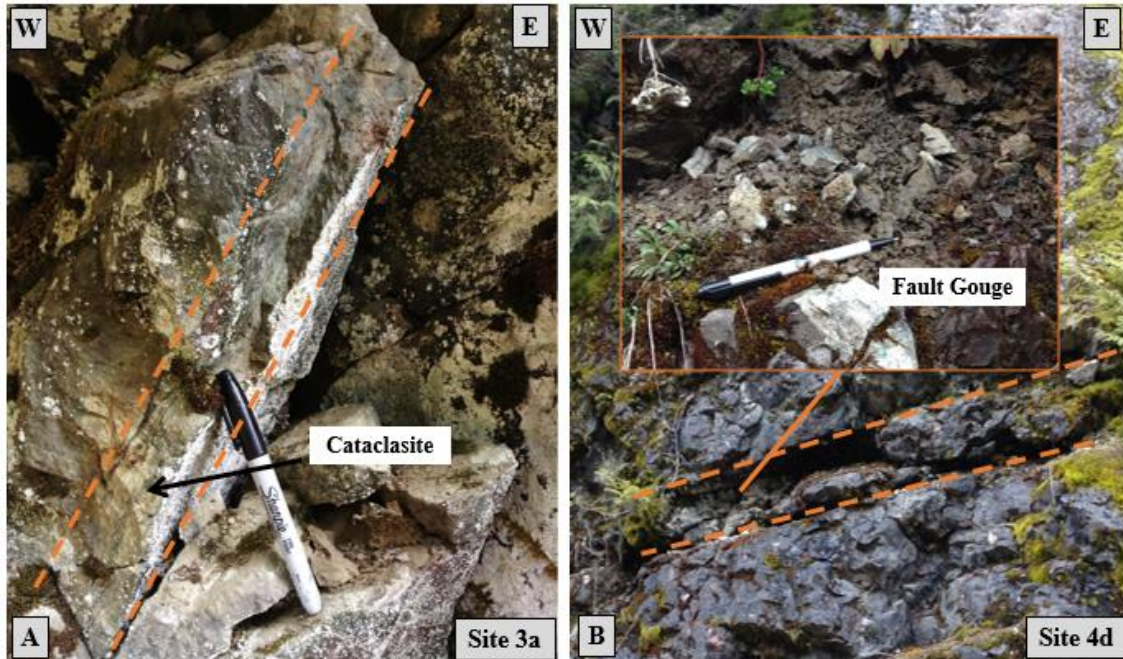
Figure 5.5. Photo of evidence for comminution on some faults. A) A fault at Site 3a shows cataclasite. B) A fault at Site 4d shows unlithified fault gouge. Photos are of subvertical outcrops facing north. The pens are 15 cm long.

Figure 5.6. Photo of slickenlines on fault planes at Site 4c. Photo was taken facing northwest. Pen is 15 cm long.
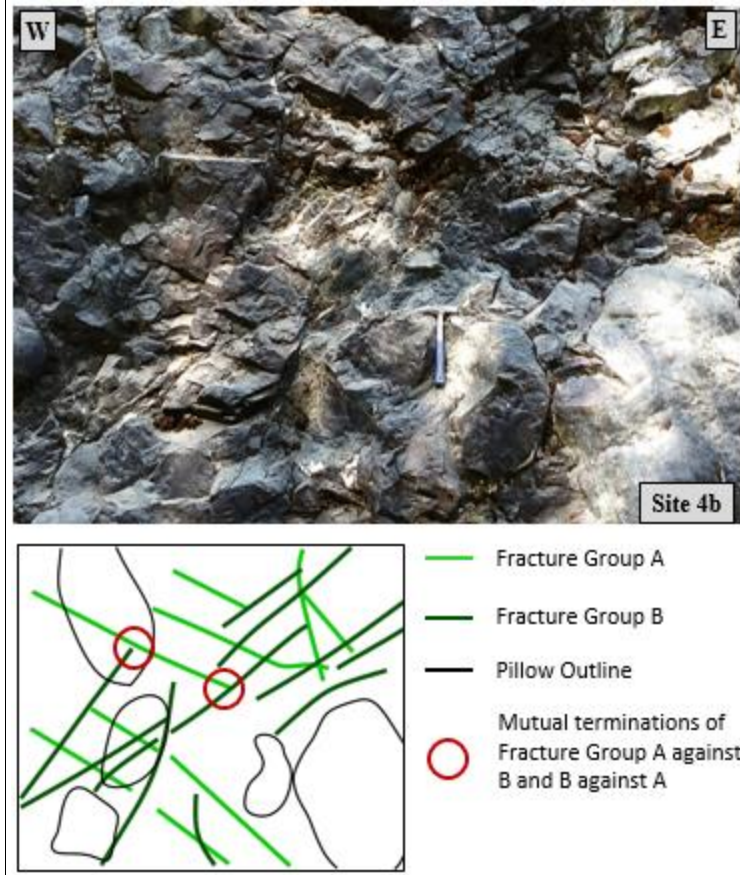
Figure 5.7. Photo and interpretive diagram of fractures cutting through the pillow basalts. Group A dips to the east and Group B dip to the west. The red circles in the diagram highlight examples of where the fractures are mutually cross-cutting. Photo is of a subvertical outcrop from Site 4b facing north. The rock hammer is 36 cm long.
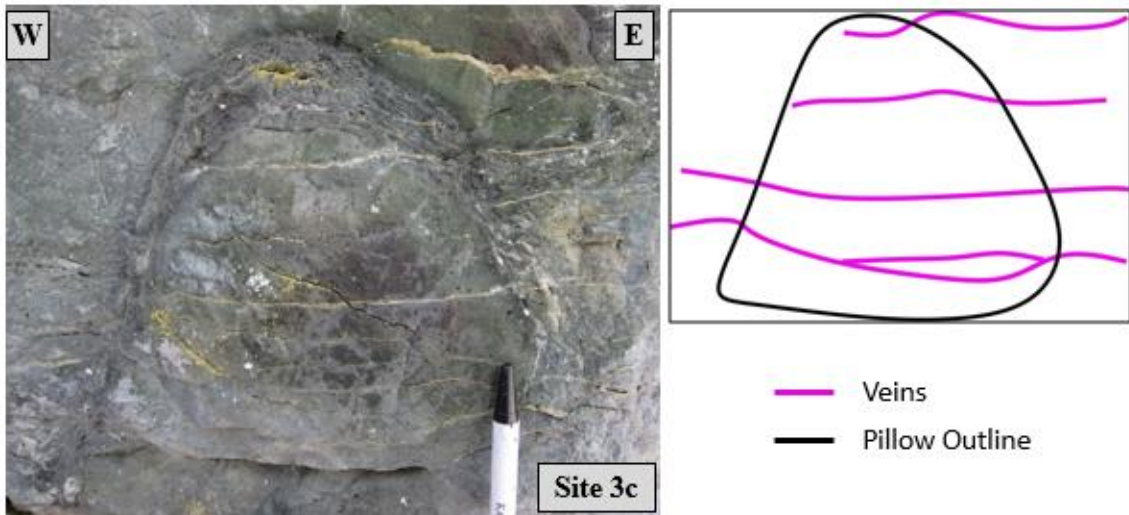
Figure 5.8. Photo and interpretive diagram of veins cutting across an individual pillow. Photo was taken of a subvertical outcrop from Site 3c facing north. The portion of the pen showing is 5 cm long.
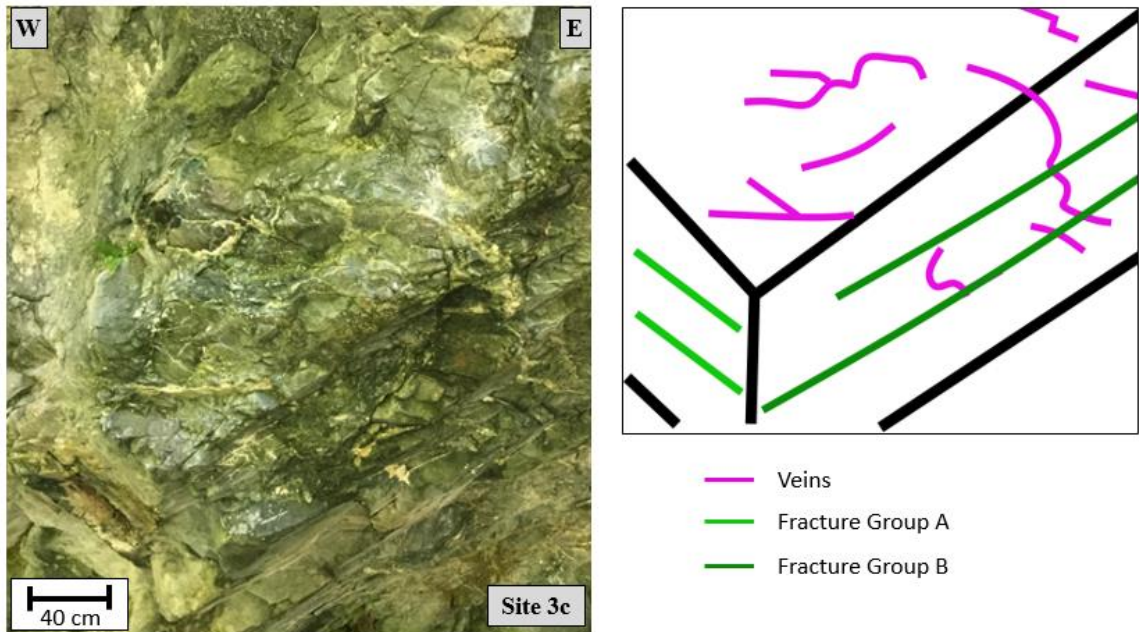
Figure 5.9. Photo and interpretive diagram of a cluster of veins identified at Site 3c. The veins are cut by fractures. Photo is of a subvertical outcrop from Site 3c facing north.
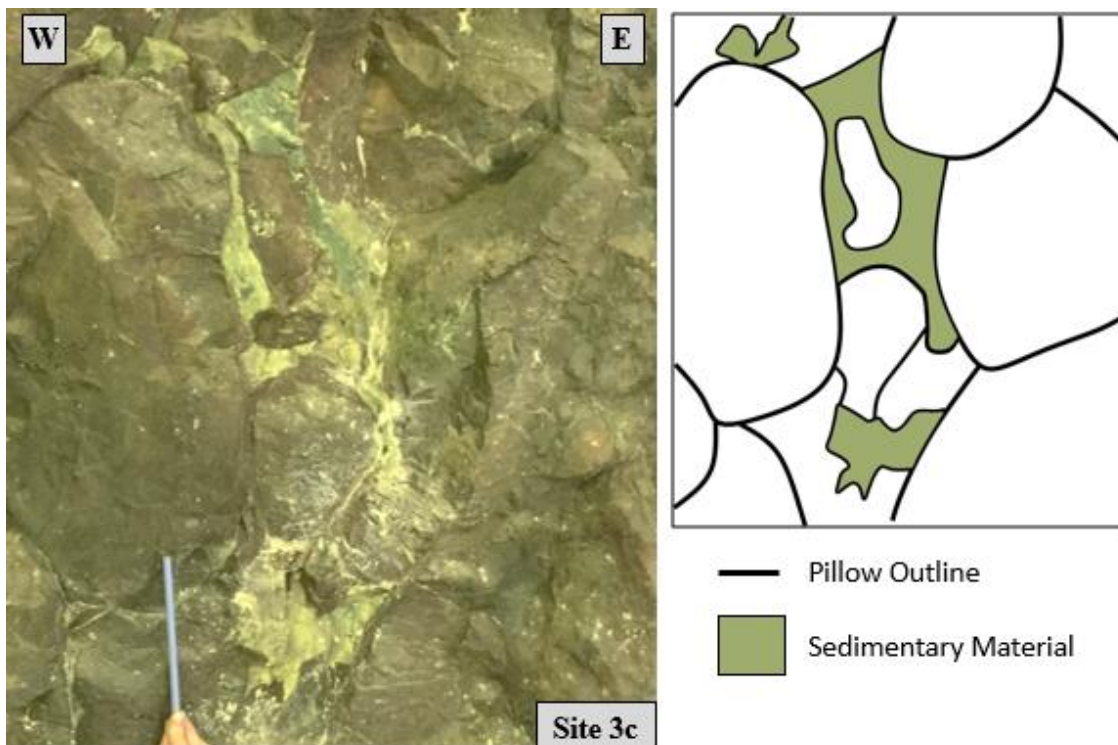
Figure 5.10. Photo and interpretive diagram of meta-sedimentary material between pillow basalt beds. Chunks of pillow basalt appear to be incorporated into this meta-sedimentary material. Photo is of a subvertical outcrop from Site 3c facing north. The pencil is 15 cm long.

65

5.1.2 Structural Orientation Data

Bedding measurements were taken along the most convex side of the pillows (**Fig. 5.2**). Three-dimensional views present in the outcrops gave confidence that measurements accurately reflect bedding orientations, and measurements are relatively consistent from site to site. Beds are subvertical to vertical and strike north-south (**Fig. 5.11**). The orientation of sedimentary material between pillows (**Fig. 5.10**) are also included with the bedding data.

Nine faults of varying orientations were identified across the pillow basalt outcrops. The faults have been divided into four groups based on orientation, geomorphic expression, and confidence in their existence (**Table 5.1**). All fault orientations and associated slickenline measurements are shown in **Figure 5.12** with their respective groups delineated. Two faults were identified with high confidence (5/5) and are oriented similarly, striking NW-SE and dipping to the NE, and are grouped as Fault Group A. Five faults were identified with moderately high confidence (4/5) and strike NE-SW. These faults have been separated into different groups based on their dip direction; Group B dips to the NW whereas Group C dips to the SE. Two faults were identified with moderate confidence (3/5) and are grouped as Fault Group D. These faults strike E-W and dip to the south.

Figure 5.13 shows the orientations and number of faults identified at each subsite. Site 3a has the most faults, one of each group. Of the two faults identified at Site 3b, one is of Group C and one is of Group D. Site 4a has one fault of Group B, Site 4b has one fault Group C, and Site 4d has one fault of Group A.

The fracture orientations at each subsite are presented in **Figure 5.14**. When all fracture orientations are plotted together, two main orientations are apparent, which reflect the oppositely dipping Groups A and B observed in outcrop (**Fig. 5.15**). Fracture Group A strikes NW-SE, dips to the NE, and has a representative orientation of (303, 40). Fracture Group B strikes NE-SW, dips to the NW, and has a representative orientation of (211, 39).

The veins also show a range in orientations and distribution (**Fig. 5.16**). Measurements are for those veins that cut across basalt pillows. Orientations range in strike from E-W to NNE-SSW and dip shallowly to the N, NE, and E. The sites that show a greater number of vein measurements indicate that a cluster was found at that site. More clusters were identified at Site 3 than Site 4, and Site 3 has significantly more veins than Site 4. There is no obvious trend in grouping of orientations from site to site.

Figure 5.17 shows all bedding, fault, fracture, and vein data combined.
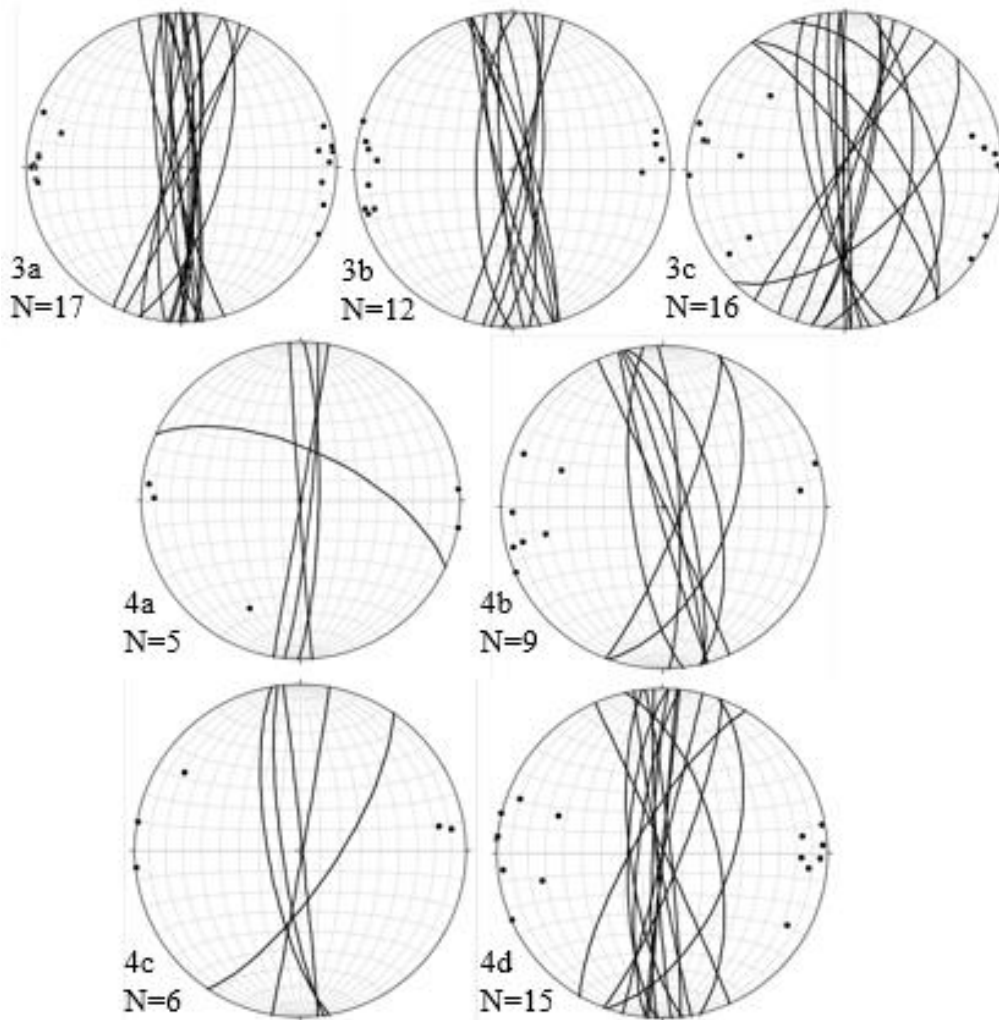
Figure 5.11. Pillow basalt bedding planes and poles for Sites 3a-c and 4a-d. Plots are lower hemisphere, equal area stereographic projections. N values refer to the number of measurements presented in each stereonet.
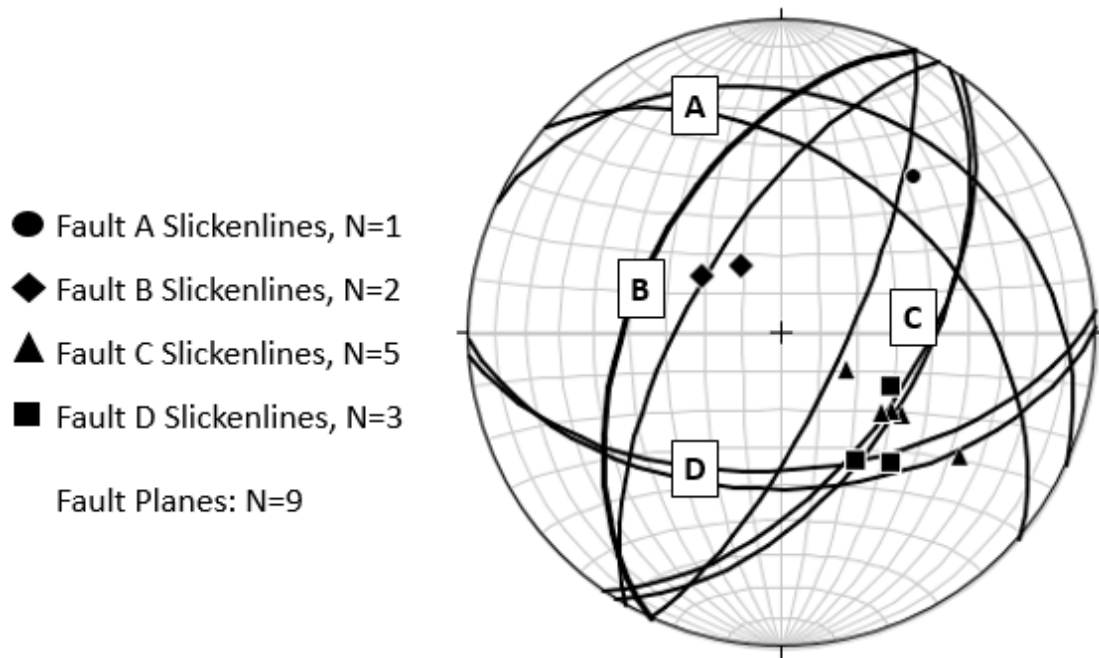
Figure 5.12. Grouping of fault plane measurements and associated slickenline data from the pillow basalt outcrops. Fault groupings were made based on orientation and field expression. All slickenlines indicate a normal sense of motion. Plots are lower hemisphere, equal area stereographic projections. N values refer to the number of measurements presented in each stereonet.
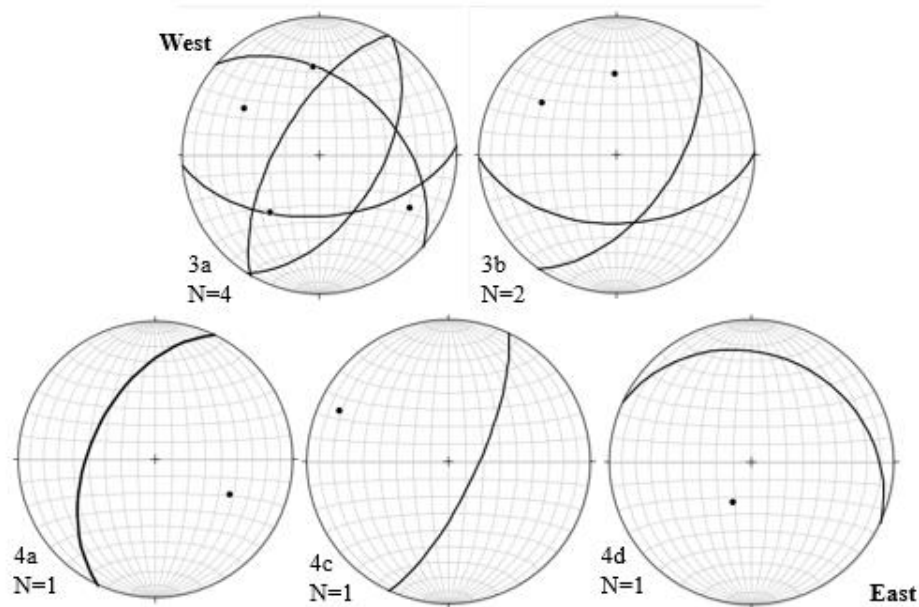
Figure 5.13. Fault planes and poles from the pillow basalt outcrops, Sites 3a-c and 4a-d. Plots are lower hemisphere, equal area stereographic projections. N values refer to the number of measurements presented in each stereonet.
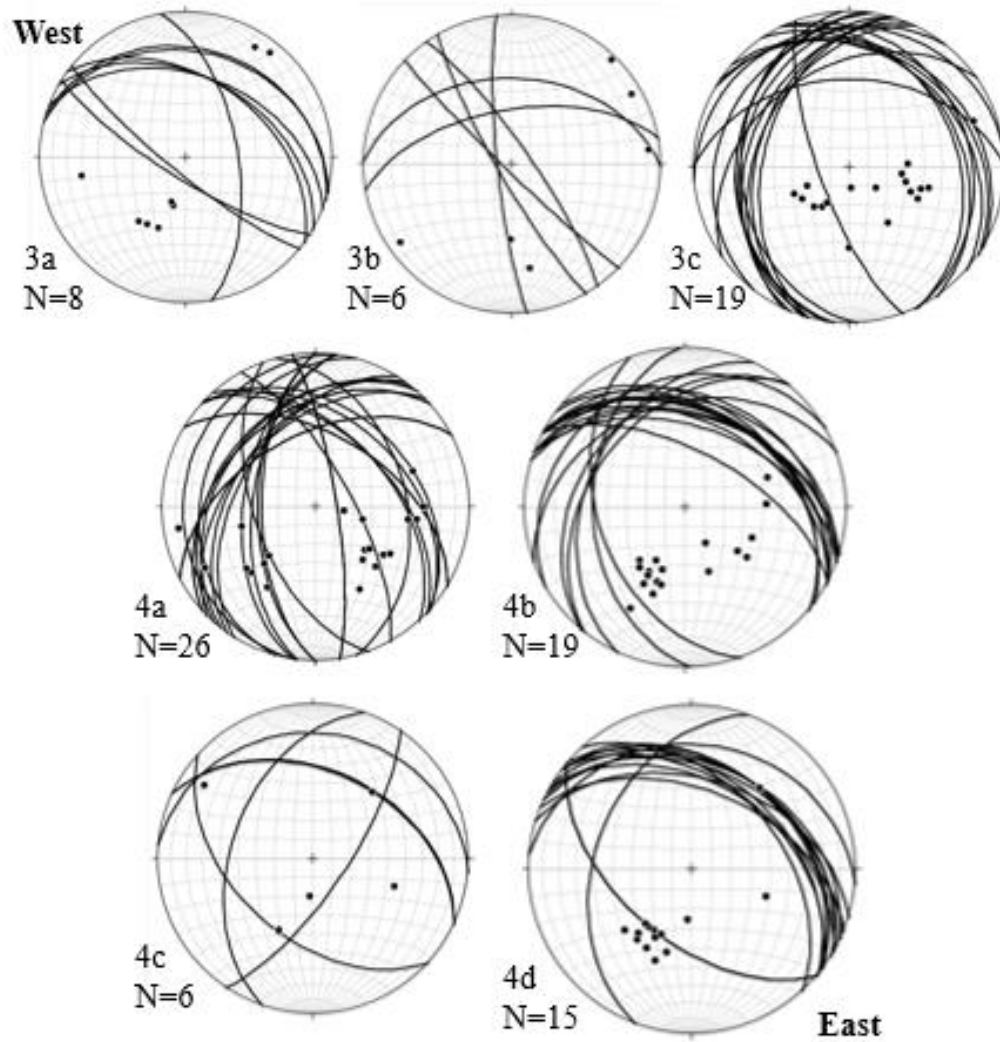
Figure 5.14. Fracture planes and poles from the pillow basalt outcrops, Sites 3a-c and 4a-d. Plots are lower hemisphere, equal area stereographic projections. N values refer to the number of measurements presented in each stereonet.
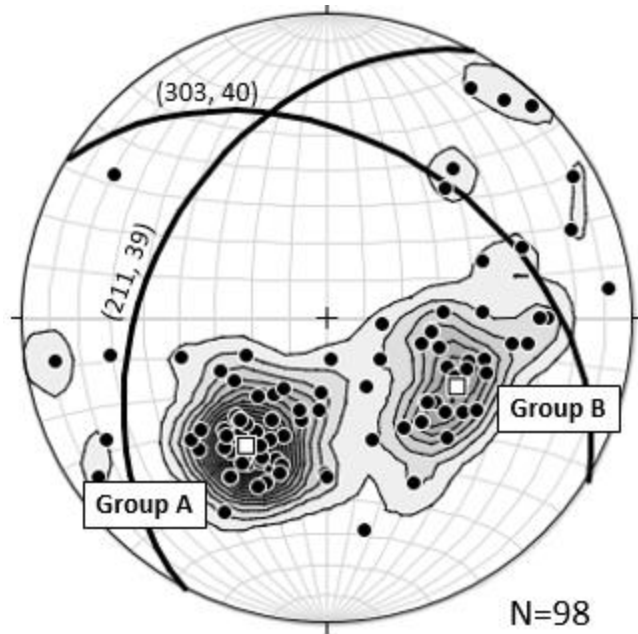
Figure 5.15. Poles to all fracture plane measurements from the pillow basalt outcrops. Group A has a representative orientation of (303, 40), and Group B has a representative orientation of (211, 39). Representative orientations are indicated by white squares. The plot is a lower hemisphere, equal area stereograph with 1% area contours. The N value refers to the number of poles presented.
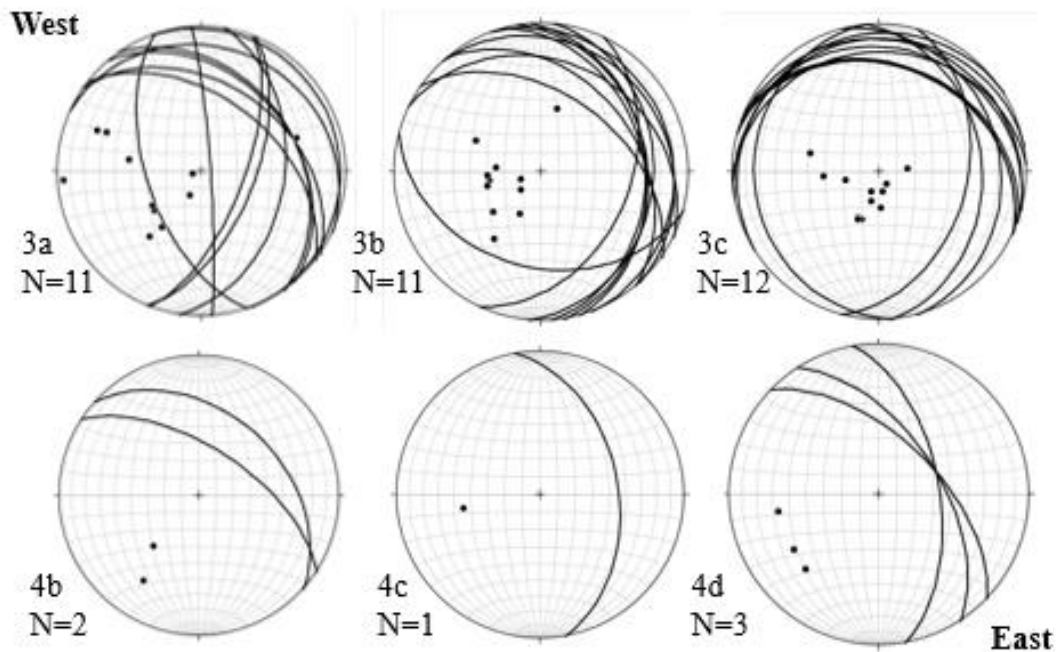
Figure 5.16. Vein planes and poles from the pillow basalt outcrops, Sites 3a-c and 4a-d. Plots are lower hemisphere, equal area stereographic projections. N values refer to the number of measurements presented in each stereonet.
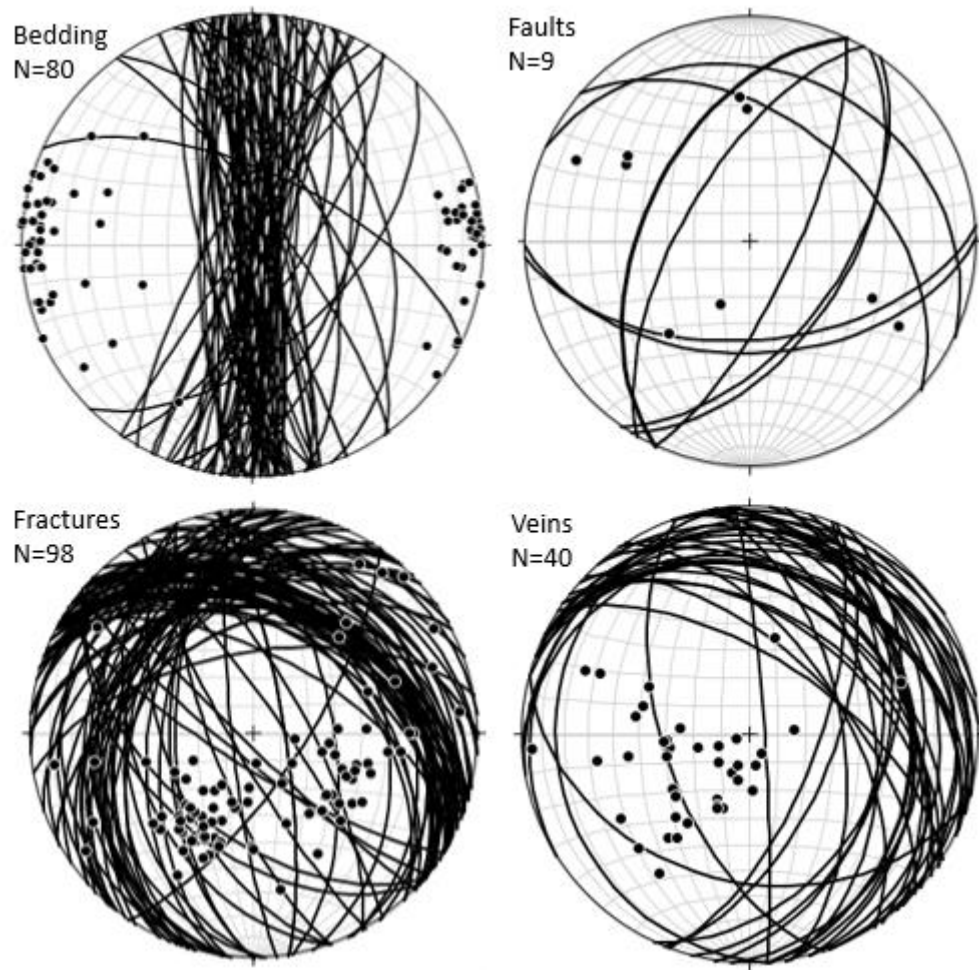
Figure 5.17. Planes and poles of all structures from the pillow basalt outcrops, Sites 3a-c and 4a-d. Plots are lower hemisphere, equal area stereographic projections. N values refer to the number of measurements presented in each stereonet.

5.1.3 Microscale Data and Observations

Samples were collected to investigate how micro-structures vary throughout the core, rim, and sedimentary material within the pillow basalts. This section looks at three samples: Sample C from Site 4c, Sample D from Site 3a, and Sample E from Site 4a. Samples C and D show the edge of the pillow cores, their rims, and meta-sedimentary material along their margins, referred to here as the matrix (**Fig. 5.18**). Sample E is from the center of a pillow core, away from the rim-matrix boundary.

The pillow cores (Sample E) are aphanitic and have an intersertal textured groundmass of plagioclase, clinopyroxene, chlorite, actinolite, and sparse olivine (also described by Lyttle & Clarke [1975]; **Fig. 5.19a**). The plagioclase crystals are thin and feathery. The shape of the chlorite and actinolite mineralizations suggests that they are pseudomorphs of clinopyroxene and olivine. Vesicles are present and are filled with calcite, quartz, prehnite, and zeolites. Iron oxides are prevalent (titanomagnetite according to Lyttle & Clark [1975]) and increase in density towards the pillow rim (**Fig. 5.19b**), giving the rim a black appearance in thin section.

The pillow rims are composed of discontinuous layers of calcite, devitrified glass, oxides, and other minerals, such as chlorite (**Fig 5.20**). The rims in Sample C contain more oxide and calcite layers than the rims from Sample D, which contain more devitrified glass and chlorite layers. The boundary between the layered rim and the oxide-rich edge of the pillow is not always discrete. For example, the oxide layers in the rim of Sample D are less well developed and grains are more interspersed the closer they are to the pillow side of the rim.

73

The meta-sedimentary matrix material originated as micritic, calcareous mud. In general, the material of Sample C is microcrystalline and contains microfossils (described as coccoliths by Garrison [1972]; **Fig. 5.21a**). The material of Sample D is devoid of fossils and coarser-grained, with individual grains discernable at the micro-scale (**Fig. 5.21b**). Oxides are also observed in the matrix and appear as red mineralization in hand sample. This observation is consistent with the presence and distribution of oxides and the overall macro-scale color of the matrix material between sites. Oxides are distributed throughout the matrix in Sample D, giving it a redder overall appearance, whereas the oxides are more localized in Sample C (e.g., red areas near the rims in the otherwise green matrix; Fig. 5.18).

Veins are observed throughout the pillow cores and matrix. Consistent with field observations, some veins are contained within the pillows and terminate at the pillow rim, whereas others cross-cut the pillows and matrix (Sample D, **Fig. 5.18**). Veins are composed of blocky quartz and calcite crystals that show twinning (**Fig. 5.22**). The larger veins, and to a lesser extent the smaller veins, in Sample D are oriented similarly to those measured in outcrop (**Fig. 5.16**). There is no significant offset on the veins, and overall, they are not folded.

Samples C and D show fold structures along the pillow rims (**Figs. 5.18, 5.23**). Among all the samples collected, fold structures were not common but locally developed in some samples. The folds bend the meta-sedimentary matrix and the layers in the pillow rims. An accumulation of darker material in the meta-sedimentary matrix define subtle linear structures that appear axial planar to the folds (**Fig. 5.23a**)

The folds were imaged with the scanning electron microscope (SEM). The pillow rims did not show an alignment of mineral grains consistent with a mineral fabric, although the layering in the rims was locally disrupted. The oxides within the meta-sedimentary core showed a preferred orientation, parallel to the axial trace of the apparent folds. Where the mineral matrix showed a darker red appearance in hand sample, aligned oxide grains anastomose around calcite grains **(Fig. 5.24a&b)**. In other areas without an abundance of oxides, the mineral fabric is defined by the elongate shape of calcite grains. The degree of alignment appears to be stronger and more prevalent in Sample D than in Sample C. However, this mineral fabric is variably-developed in and around the folds and is not penetrative. Samples C and D show horizontal cuts of the rock, and the strike orientation of mineral alignment was estimated from north (**Fig. 5.25**). The orientations are predominantly WNW-ESE in Sample C and range from NE-SW to NW-SE in Sample D, with the strongest grouping oriented WNW-ESE. However, these structures are rare and the sample size is small, so these orientations are not necessarily indicative of a penetrative fabric throughout the sedimentary matrix.
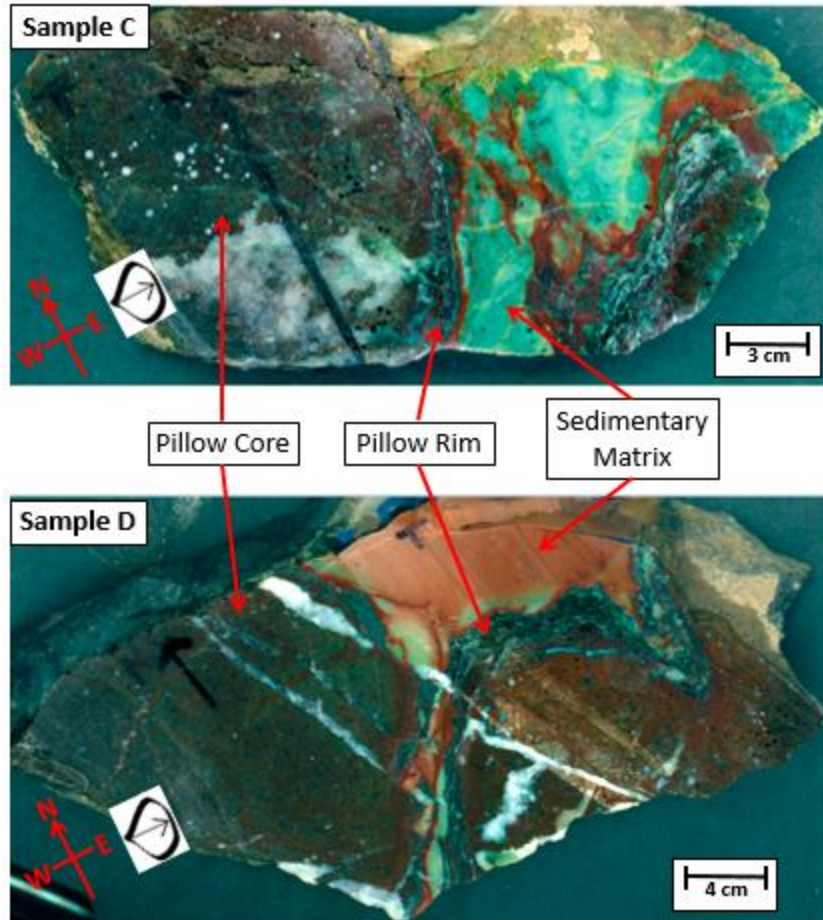
Figure 5.18. Slab scan images of pillow basalt Samples C and D. The pillow core, rim, and meta-sedimentary matrix material are highlighted. Sample C is from Site 3a; Sample D is from Site 4c. Both slabs are cut in map view (looking down from above).
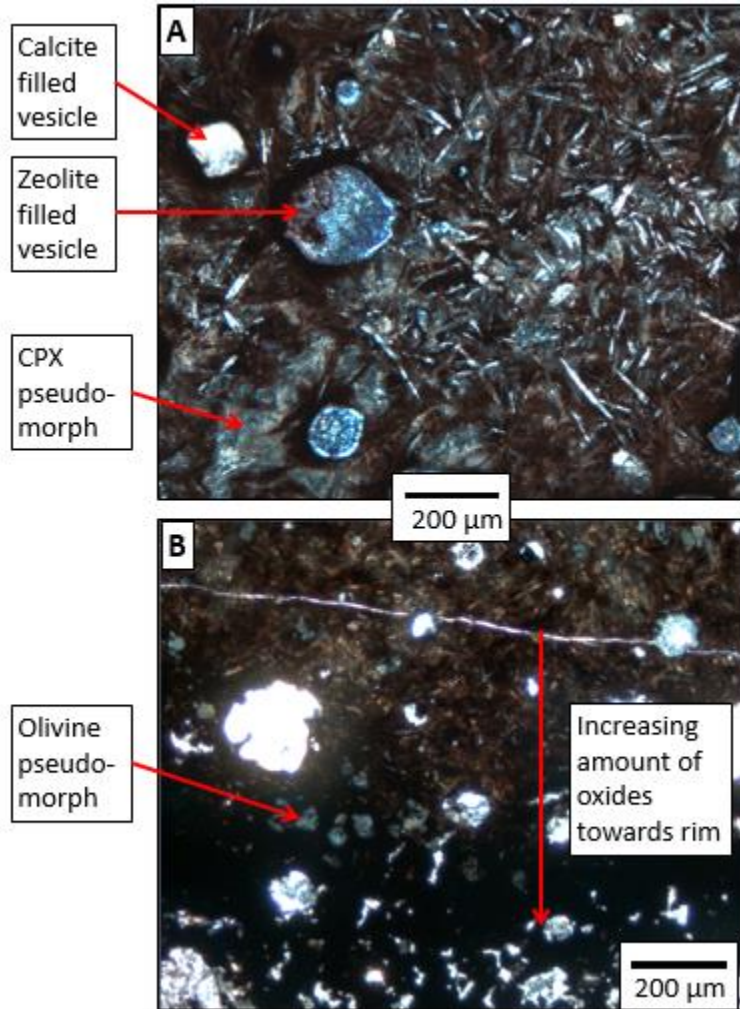
Figure 5.19. Photomicrographs of the pillow basalt ground mass. (a) shows the center of a pillow core and (b) shows the core near the rim of a pillow. The groundmass is composed of plagioclase, clinopyroxene (CPX), and olivine. The CPX and olivine crystals are pseudomorphs and have been replaced by actinolite, chlorite, calcite, and other minerals. Oxides are prevalent throughout and increase in density towards the rims of the pillows (b). Vesicles are filled by zeolites and calcite. Images show cross-polarized light; A-Sample E; B-Sample D.
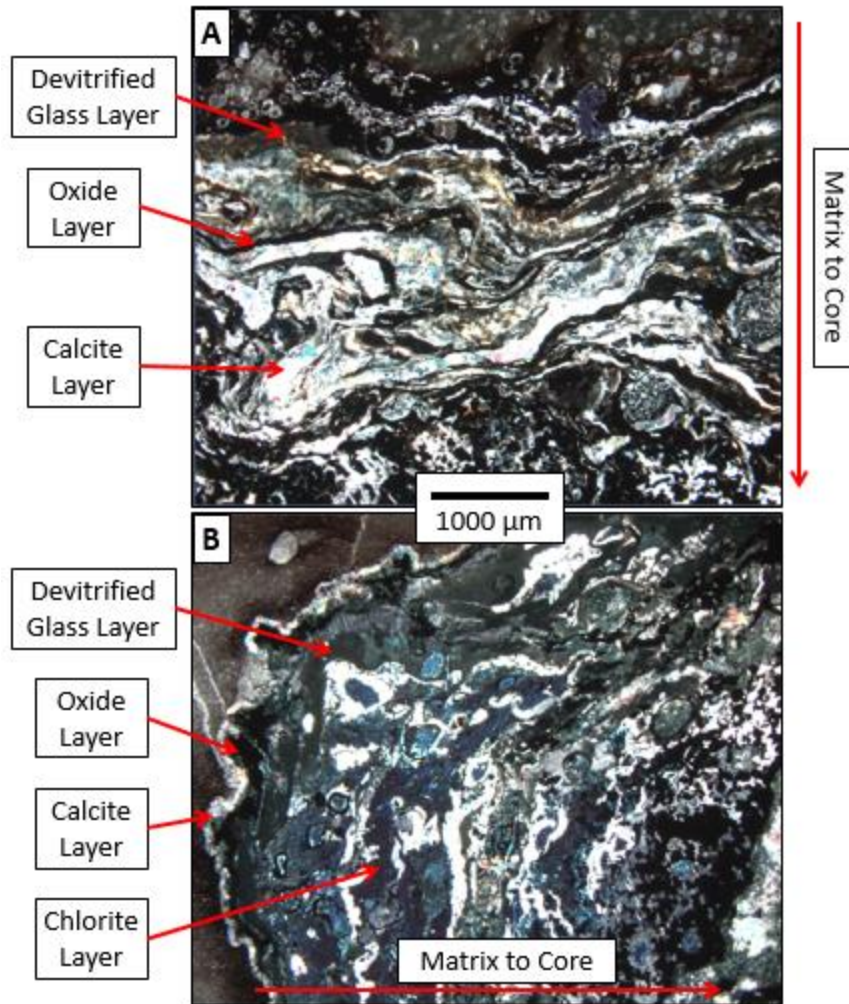
Figure 5.20. Photomicrographs of pillow rims. The rims are composed of varying amounts of discontinuous layers of calcite, devitrified glass, oxides, and chlorite. Sample C has more calcite and oxide layers whereas Sample D has more devitrified glass and chlorite layers. Images show cross-polarized light; A-Sample C; B-Sample D.
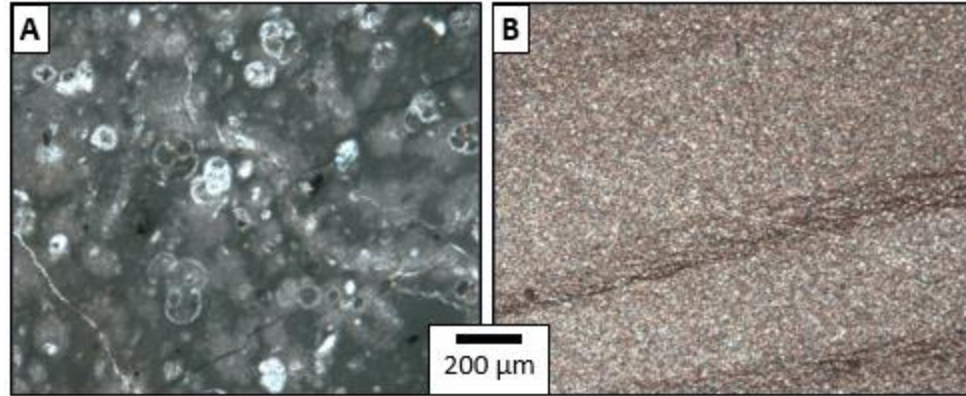
Figure 5.21. Photomicrographs the meta-sedimentary matrix of the pillow basalts. (a) shows the matrix of Sample C which is microcrystalline and contains microfossils. (b) shows the matrix of sample D which is devoid of fossils and coarser grained. Images show plane polarized light.
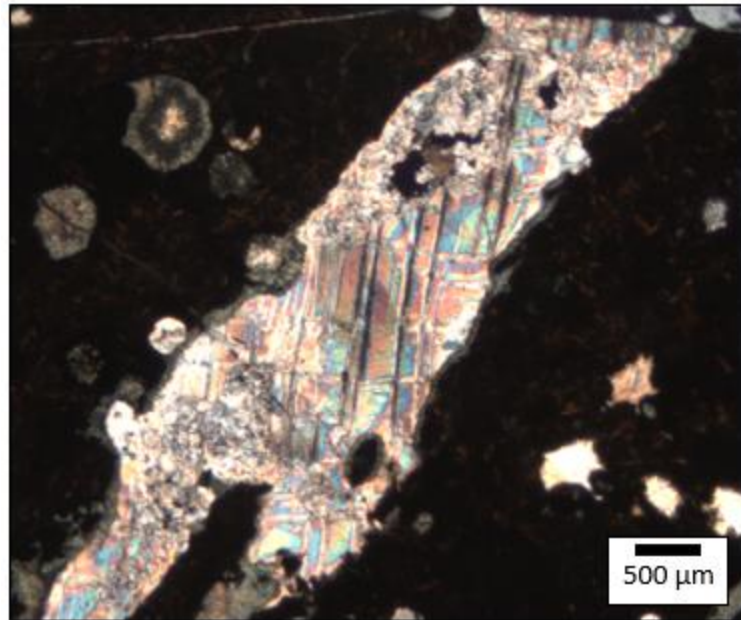
Figure 5.22. Photomicrograph of a calcite vein showing twinning. Image is of Sample D and shows cross-polarized light.
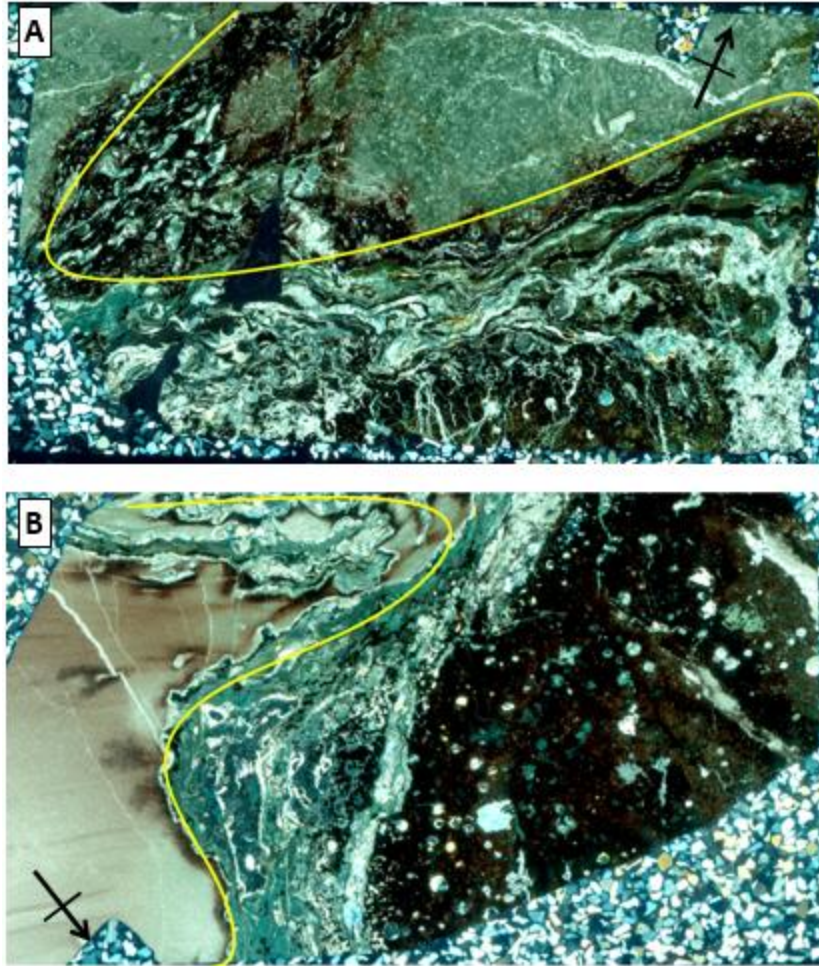
Figure 5.23. Photomicrograph in polarized light of two thin sections made from the rock slabs with the apparent folds outlined as traced by the pillow rims. (a) is from sample C and (b) is from sample D and thin sections are in map view (looking down from above) where north is indicated by the black arrows.
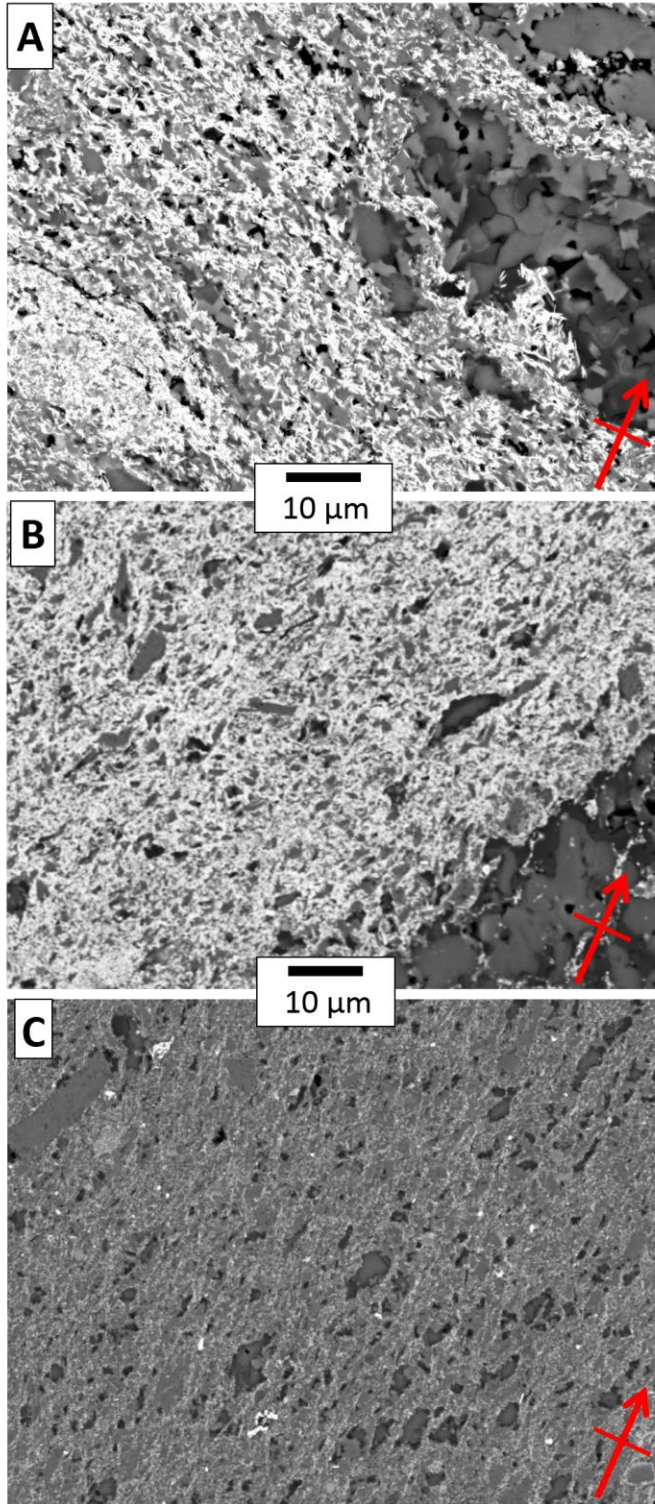
Figure 5.24. Backscattered electron images of mineral fabric locally developed in the meta-sedimentary matrix material. (a, b) show the aligned lighter oxide grains that anastomose around the darker calcite grains; these are from areas with a high concentration of oxides and appear darker red in hand sample. (c) shows a mineral fabric farther from the red, oxide-rich area of the thin section A-Sample C; B and C-Sample D. Images are in map view and north is represented by the red arrow.
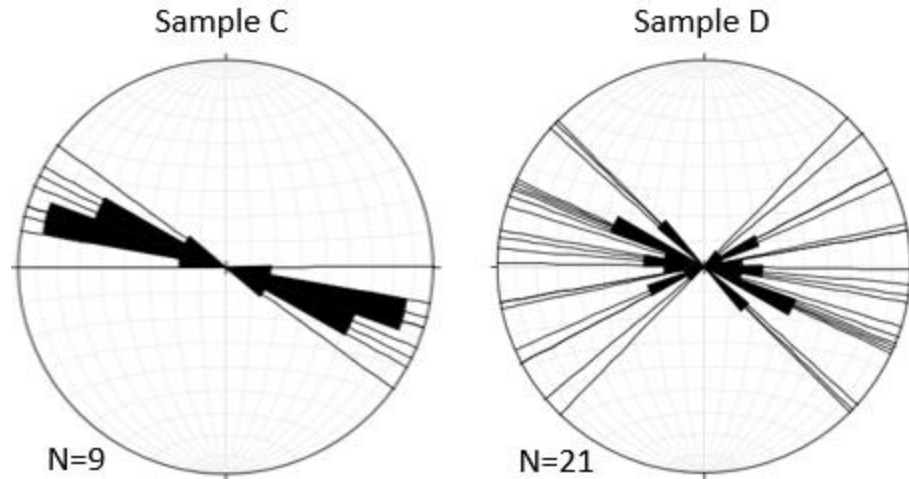
Figure 5.25. Rose diagrams of the average orientation of aligned oxide grains. The orientations are strike estimates as measured from backscattered electron images of thin sections that were cut parallel to the horizontal in "map view".

5.2. Interpretation

This section presents interpretations made based on the field observations, structural data, and micro-scale observations from the pillow basalt outcrops, Sites 3 and 4, of the Hamma Hamma Transect. Table 5.2 shows representative orientations of the structures discussed.

The representative orientation for the pillow basalt bedding is (002, 88); striking N-S and dipping near vertical. Pillow basalts form initially with horizontal bedding, so the present orientation indicates that the beds have been rotated approximately 90°. The pillows top toward the east, so the direction of rotation must be clockwise. The calculated axis of rotation is (00→182) with a magnitude of 92°, clockwise (**Fig. 5.26**). The necessary σ1 for this rotation is oriented E-W.

When all the fault and fracture data are compared, some similar trends are observed (**Fig. 5.17**). The first is that Fault Groups A and B are have similar orientations

to Fracture Groups A and B.   This indicates that the respective groups are related; as a fracture network forms, the fractures will interconnect and form faults that accommodate further movement (**Fig. 5.27**). The presence of cataclasite and fault gouge on the faults in Group A indicate that these faults have accumulated the greatest amount of strain. Since the fracture groups mutually crosscut one another and because of their relative orientations (**Fig. 5.7**), I interpret Faults A and B as conjugate faults with a σ1 of (12→265). This indicates that the faults formed from horizontal, nearly E-W compressive stresses with a reverse sense of motion (**Fig. 5.28**). The slickensides, however, indicate that the last motion on the faults' surface was of a normal motion (smooth down dip on footwall side). If the faults formed in their present orientation, then they must have been reactivated as normal faults by a change in the stress regime. The exhumation of the Crescent Fm. created steep mountains relatively quickly. If the erosion rate cannot keep up with the rate of steepening, normal faulting will occur to alleviate vertical stresses. The discrepancy in the slickensides for Fault Groups A and B is interpreted as reactivation of the faults as normal faults from over-steepening.

If Fault Groups A and B did reactivate as normal faults from over-steepening, it is possible that additional faults would have formed in orientations more optimal for normal slip. Based on orientation, Fault Group C stands out as a conjugate to Fault Group B, with σ1 oriented (87→345) (nearly vertical) and a σ3 oriented (00→119) (nearly horizontal and NW-SE) (**Fig. 5.29**). Slickenline measurements on both Groups B and C are also consistent with normal, dip-slip motion. Therefore, if Faults B and C are conjugates, they have a normal, extensional, geometry. Based on similarities in

orientation, Fault Group C does not have a fracture group associated with it, but it does crosscut through the fractures that are associated with Fault Groups A and B. This supports the interpretation that Fault Group C formed after Fault Groups A and B. A normal conjugate was not identified for Fault Group A.

Fault Group D was identified in the field with the lowest confidence because the faults strike subparallel to the outcrop and only footwall surfaces could be observed. The orientation of slickenlines measured on these faults were used to determine possible reverse and normal conjugates (**Fig. 5.30**). The principal stresses, σ1 and σ3, for each regime do not appear to correlate with any of those calculated for the other faults. Like the other fault groups, the nature of the slickensides suggest that the last motion on the fault was normal. If Fault Group D formed initially as a reverse fault and then reactivated as a normal fault, like Groups A and B, then this would a significant change in the state of stress, from E-W (as calculated for Groups A and B) to N-S (as calculated by the hypothesized reverse conjugate in **Fig. 5.30**). There are other reverse faults mapped in the vicinity that are oriented similarly to Fault Group D (i.e. the western extent of the Seattle Fault), supporting the interpretation of some component of revers motion on the fault.

The vein orientations can be weakly correlated with the fracture orientations if the fractures represent Mode II structures and the veins are Mode I structures. If the veins are Mode I fractures, then their poles indicate a σ3 stress direction. **Figure 5.31** shows all of the fracture data plotted as planes and the location of the line of intersection (red circles) of eight selected pair of fractures. The fracture pairs that define these intersections were considered conjugates, and the σ3 was calculated for each (red triangles). When

compared, the contoured range of the poles to veins (i.e., their estimated σ3) and the

range of σ3 for the selected fracture pairs overlap, which would indicate that the fractures

and the veins formed under the same state of stress. However, there are some vein

orientations that do not agree with this correlation and are more similar in orientation to

fracture Group B, suggesting that some veins are mineralized Mode II fractures.

Within the pillow basalt outcrops, selected samples show that the meta-
sedimentary matrix and the pillow rims are folded with an associated mineral fabric. The

presence of this fabric means that some component of strain was taken up by the matrix

and was driven by dissolution-driven or crystal plastic processes. The sample from Site 3

shows the fabric localized to the pillow rim/sediment boundary whereas the sample from

Site 4 shows the fabric more distributed throughout the sediment. This indicates that

folding and fabric development occurred locally but was not penetratively developed

across the outcrops.

Table 5.2. Representative orientations of major structure groups in the pillow basalt outcrops.

Structure	Representative Orientation(s)
Bedding	(002, 88)
Fault Group A	(304, 37)
Fault Group B	(207, 59)
Fault Group C	(031, 61)
Fault Group D	(087, 50)
Fracture Group A	(303, 40)
Fracture Group B	(211, 39)
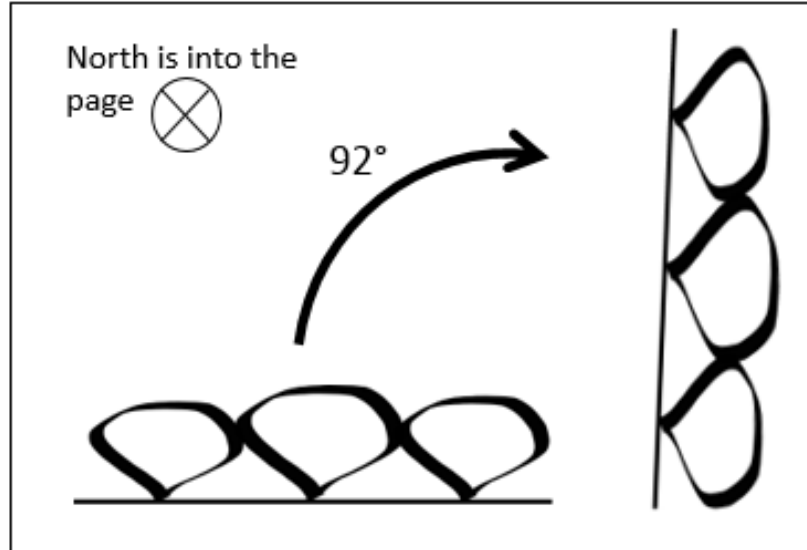
Figure 5.26. Diagram showing the rotation of the pillow basalts. The basalt was rotated ~92° clockwise from horizontal to near vertical about an estimated axis of rotation of (00→182). North is into the page.
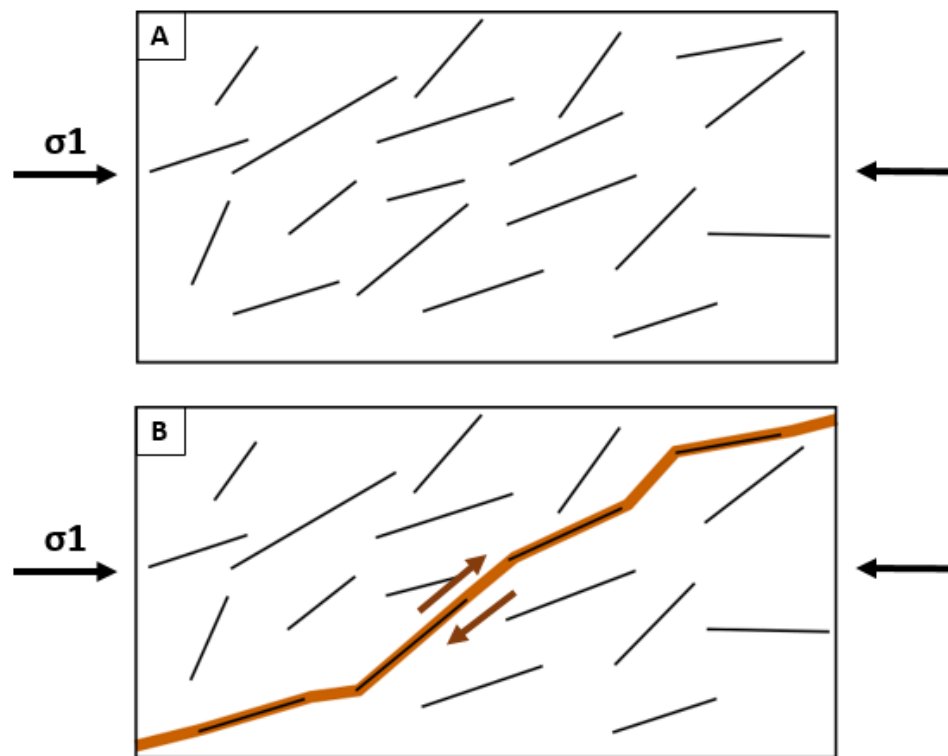
Figure 5.27. Diagram showing how a fault forms from the interconnection of fractures. A) Fractures form in response to a maximum principal stress. B) Fractures link up and form a through-going fault (orange line).
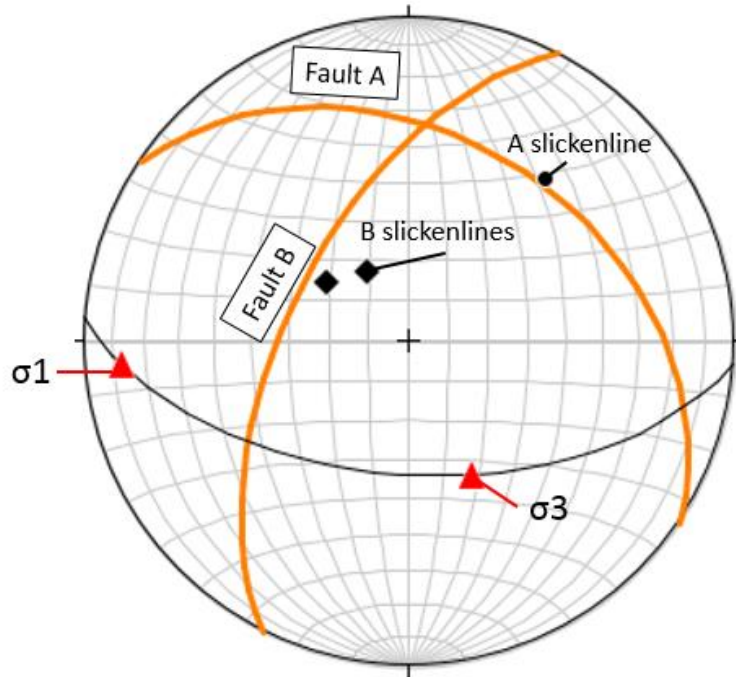
Figure 5.28. Representative orientations and an interpreted state of stress for Fault Groups A and B. If conjugates, σ1 is (12→265) and σ3 is (52→155).
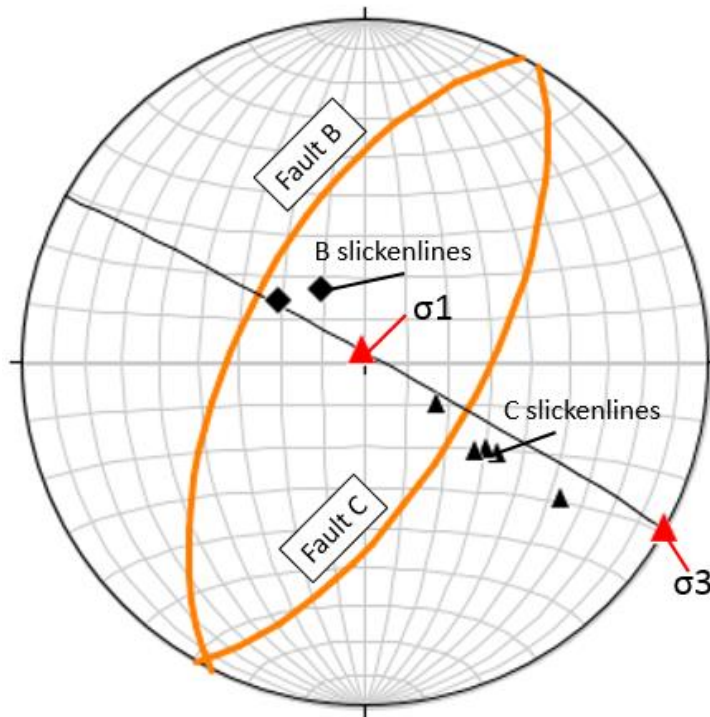
Figure 5.29. Representative orientations and an interpreted state of stress for Fault Groups B and C. If conjugates, σ1 is $(87→345)$ and σ3 is (00→119).
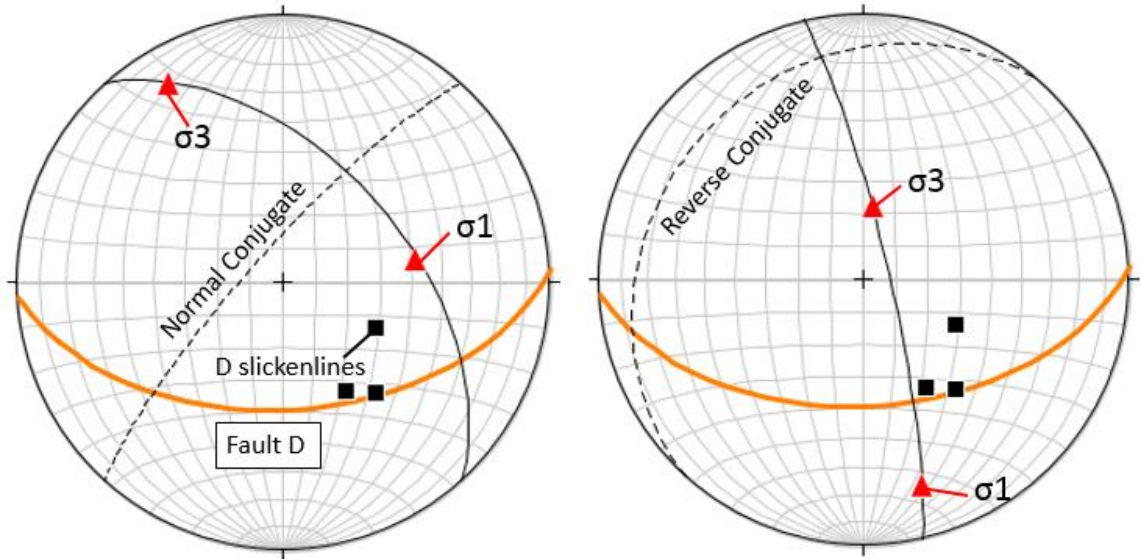
Figure 5.30. Estimated orientations for normal and reverse conjugates to Fault Group D. Conjugate faults were estimated using measured slickenlines (black squares). The principal stresses, σ1 and σ3, for each are also shown.
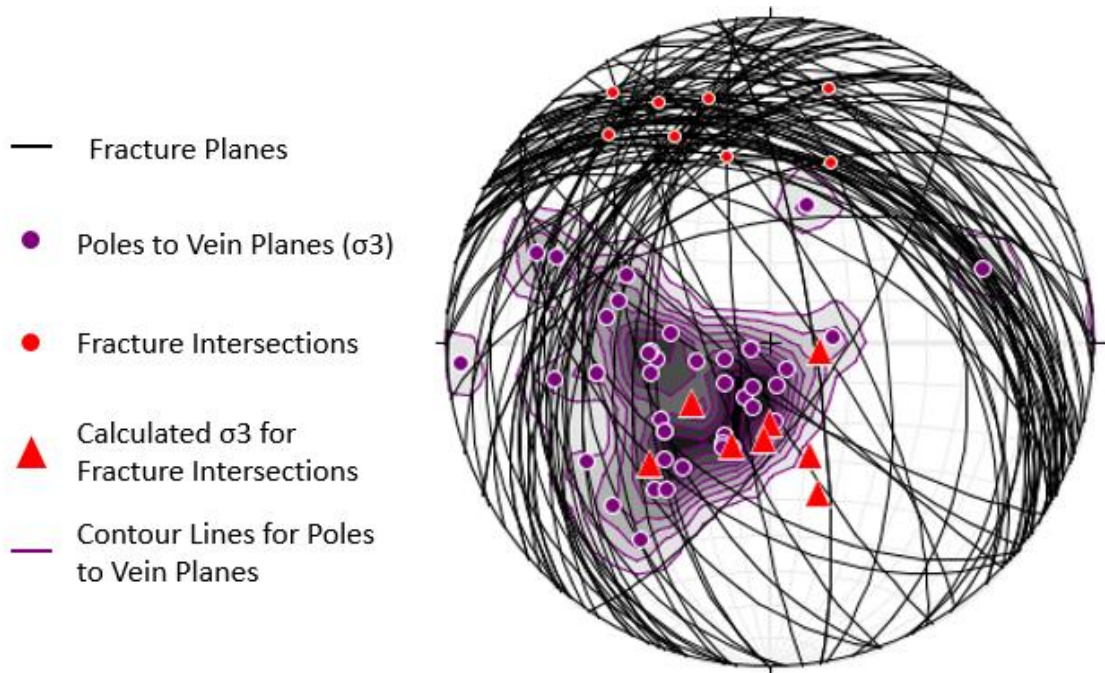
Figure 5.31. A comparison of the estimated minimum principal stress for fractures and veins in the pillow basalts. The poles to veins estimate σ3, assuming Mode I fractures (purple circles). Eight fracture intersections are shown for selected conjugate fracture pairs (red circles), and the estimated σ3 is shown (red triangles) for each pair.

5.3 Model of Deformation

Based on interpretation of the field observations and structural data from the
pillow basalt sites along the Hamma Hamma Transect, the following is one proposed
model for the deformational history of the rocks. The stages in the deformational history
are denoted by T1-5 and refer to **Figure 5.32**.

The pillow basalts of the lower Crescent Fm. formed as part of the large oceanic
chain, Siletzia. Their initial orientation was with their tops pointing upwards and their
most convex edge subparallel to the horizontal, or the ocean floor. The pillows were
rotated on end about a N-S oriented rotation axis by E-W compressive stresses associated
with the subduction zone and accretion and underplating of the meta-sediments (T1).

Once the rock package was rotated into its current position, it began fracturing
under the same E-W oriented state of stress (T2). The veins formed as Mode 1
extensional fractures and along with the fracture Groups A and B as Mode II fractures.
The fractures connected to form conjugate Fault Groups A and B that slipped through
reverse motion (T3).

If Fault Group D formed as a reverse fault as speculated, then it would have
formed by a N-S oriented state of stress. Because of a lack of crosscutting relationships, it
is not clear when it formed in relation to the other faults. However, the meta-sedimentary
interpretations suggest E-W compression followed by N-S compression. If the pillow
basalts experience a similar history, then Fault Group D would have formed after Groups
A and B (T4).

The mountains steepened as the rock body was exhuming. If the erosion rate could not keep up with the rate of steepening, then gravity would become the maximum principal stress and normal faulting would have occurred. The slickensides on Fault Groups A, B, and D indicate that the last motion on their planes was normal, so these faults may have reactivated as normal faults from over-steepening of the rock body (T5). Fault Group C may have also formed as a normal conjugate to Fault Group B.

Time	Explanation	Illustration
T1	The basalts are rotated 92° about a N-S trending axis by an E-W oriented principal stress (σ1).	
T2	After rotation, a fracture network forms under the same E-W oriented state of stress that caused the rotation.	
T3	Fractures connect up to create Fault Groups A & B which are reverse conjugates to one another.	
T4	The state of stress changes to a N-S oriented σ1 causing the formation of Fault Group D.	

(continued on next page)

T5	The rock body over-steepens and Fault Groups A, B, and D reactivate as normal faults. Fault Group C forms as a normal conjugate to Group B.	
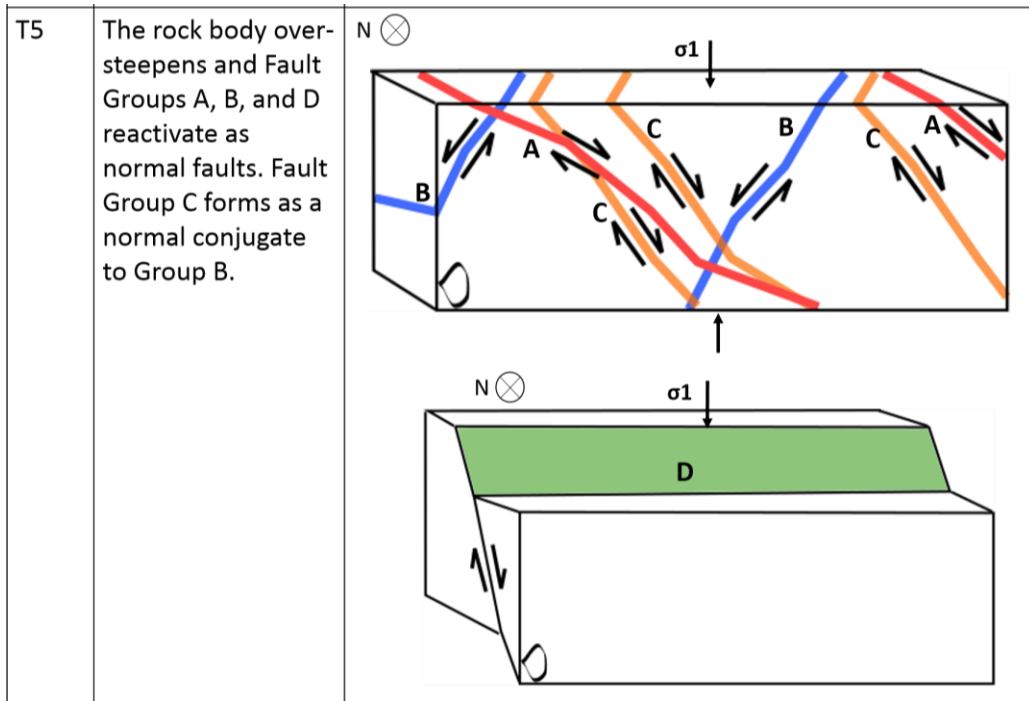
Figure 5.32. Stages in the deformational history of the pillow basalts from the Hamma Hamma Transect Sites 3 and 4. Diagrams are not to scale.

6. Comparison of Meta-Sediments and Pillow Basalts from the Hamma Hamma Transect

This chapter presents a unified model for deformation of the pillow basalts and the meta-sediments within the vicinity of the Hurricane Ridge Fault (HRF) across the Hamma Hamma Transect based on data from all four sites of this study and from the literature. **Figure 6.1** shows the main steps of the model locally within the Hamma Hamma Transect, and **Figure 6.2** shows the main steps in this model regionally for the Olympic Peninsula, as interpreted from the literature.

The pillow basalts formed between 65 and 55 Ma as part of the large, oceanic island chain, Siletzia (Duncan, 1982). Subsequent to its formation, Siletzia was accreted to the North American continent and accretion was complete by 50 Ma (**Fig. 6.1, T1**) (**Fig. 6.2a**) (Wells et al., 2014). The accretion of Siletzia overstuffed the subduction complex, and for the next 10-14 million years, the subduction zone jumped west-ward to where the Cascadia subduction zone currently lies (Schmandt & Humphreys, 2011).

Around 36 Ma, underplating, frontal accretion, and deformation of sedimentary material from the Juan de Fuca slab caused the wedge to thicken beneath the Crescent Fm. (**Fig. 6.2b**) (Brandon & Vance, 1992). Wedge thickening started to steepen the HRF and caused the rotation of the pillow basalts about the N-S oriented horizontal axis (**Fig. 6.1, T2**) (Tabor & Cady, 1978). This is also when the meta-sediments of Sites 1 and 2 of the Hamma Hamma Transect may have experienced folding at depth (**Fig. 6.1, T2**). The folds would have formed initially with their axial planes subparallel to the subducting margin, as in the classic fold and thrust structures of the accretionary wedge (Davis, Suppe, & Dahlen, 1983). The mountain range was not exhuming at this point, (Batt,

Brandon, Farley, & Roden-Tice, 2001; Brandon, Roden-Tice, & Carver, 1998), so the wedge would had to have been thickening downwards.

As wedge thickening progressed, the HRF continued to rotate into its current, near vertical position, putting the pillow basalts on end, facing the east (**Fig. 6.1, T3**). The Crescent Fm. acted as a backstop to the meta-sediments, so the folds of the Hamma Hamma Transect would have steepened along with the HRF into an upright orientation. Once the HRF was vertical and perpendicular to the regional E-W oriented subduction zone stresses, it could no longer accommodate these stresses through slip on the fault. At this point, Fault and Fracture Groups A and B, observed at Sites 3 and 4, formed to accommodate strain from continued E-W oriented compression (**Fig. 5.28**).

At 17 Ma, the exhumation of the metamorphic core began (**Fig. 6.2c**) (Brandon & Vance, 1992). It is unclear whether the HRF was already vertical at the beginning of exhumation, or if the exhumation process played a role in its steepening. If the fractures that cut the folds formed at lower temperatures where more brittle processes dominate, then the folded meta-sediments of Sites 1 and 2 of the Hamma Hamma Transect may have moved to shallower depths during exhumation and were fractured (**Fig. 6.1, T4**). If these fractures formed by N-S oriented compression (**Fig. 4.28**), this would indicate a change in the state of stress, at least locally. The presence and initial formation of Fault Group D is not well-defined; however if, as speculated, it formed initially as a reverse fault, then it would have also formed under this NNW-SSE oriented compression.

The folds of the meta-sediments are steeply-plunging, suggesting a period of rotation from an original upright orientation. This rotation of the folded meta-sediments

94

may have been driven by NNW-SSE oriented compression (**Fig. 4.25**) during the exhumation process but after fracturing (**Fig. 6.1, T5**). One of the models for Olympic exhumation suggests that the mountain range was uplifted by N-S oriented shortening of Siletzia against the Canadian Buttress (Wells et al., 1998; Blakely et al., 2009, 2011; Brocher, Wells, Lamb, & Weaver, 2017; McCaffrey et al., 2007; Wells et al., 2014; Wells & McCaffrey, 2013). If the meta-sediment fractures, rotation of the meta-sediments, and Fault Group D in the pillow basalts did result from near N-S shortening as interpreted here, then these structures would support this model. However, the study area is small compared to the whole mountain range, and the inferred change in the state of stress from E-W to N-S/NNW-SSE compression may only reflect local conditions.

As the meta-sedimentary core was exhumed, the state of stress may have shifted to gravity as the maximum principal stress. Fault Groups A, B and D may have reactivated as normal faults during this time, and Fault Group C may have formed as a conjugate to Fault Group B (**Fig. 5.29**) (**Fig. 6.1, T6**).

Time	Illustration and Explanation
T1	• The Crescent Formation is accreted to the North American continent as part of Siletzia. • The pillows have their most convex sides pointing upwards.
T2	• An E-W oriented principal stress (σ1), associated with the subduction zone to the west, caused the Crescent Fm. to begin to rotate on end. • Sediments were underplated beneath the Crescent Fm.; the boundary between the two rock bodies is the HRF. • Sediments are folded about an axial plane that is parallel to the HRF, which initially was parallel to the subduction zone. This happened at a depth where fold dominated deformation occurs.
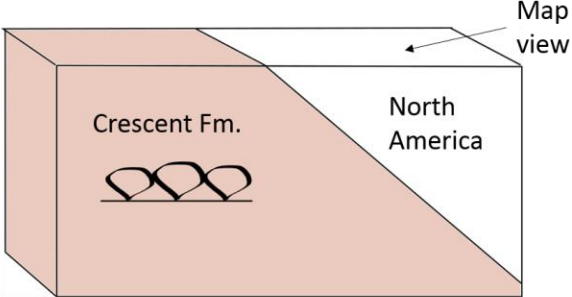
(continued on next page)

T3	• The HRF steepens into its current position by E-W compression and the folds steepen along with it. • The HRF is perpendicular to σ1 and slip on its plane can no long accommodate E-W compression. Fault Groups A and B form to accommodate further E-W compression. ⊗ N B /A← 1/B A← σ1 → ← HRF
T4	• The meta-sediments are pushed up by continued underplating of sediments to a depth where fracture dominated deformation occurs. • There is a change in the state of stress to a σ1 oriented N-S or NNW-SSE that causes fracturing in the meta-sediments and the formation of Fault Group D. ⊗ N D Fractures ⊗ σ1
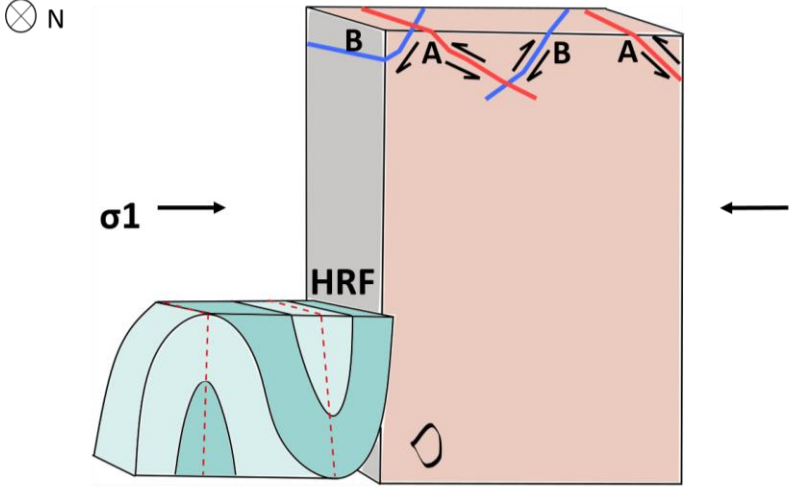
(continued on next page)

T5	• This new state of stress causes the meta-sediments to rotate into their current position.
T6	• As the mountains exhume, they become very steep, causing σ1 to become vertical. • All fault groups reactivate as normal faults (including D, not shown). • Fault Group C forms as a normal conjugate to Fault Group B.
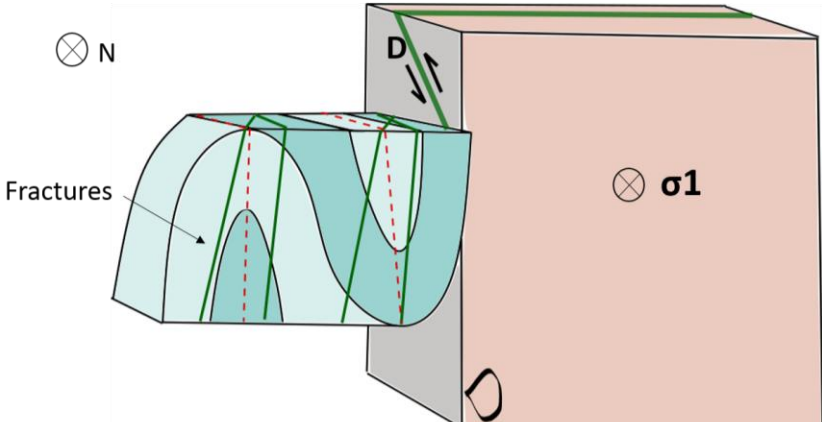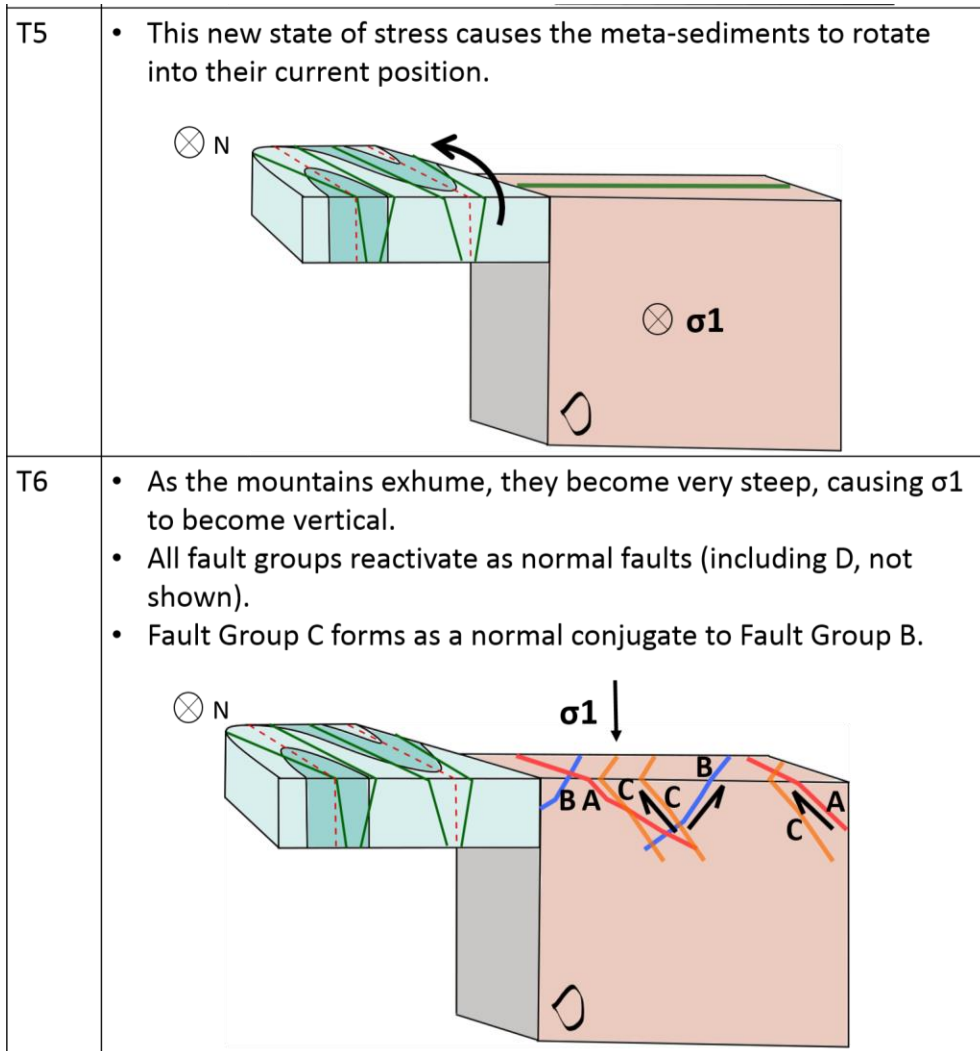
Figure 6.1. Series of events in the model of deformation for the Hamma Hamma Transect. Diagrams are not to scale.
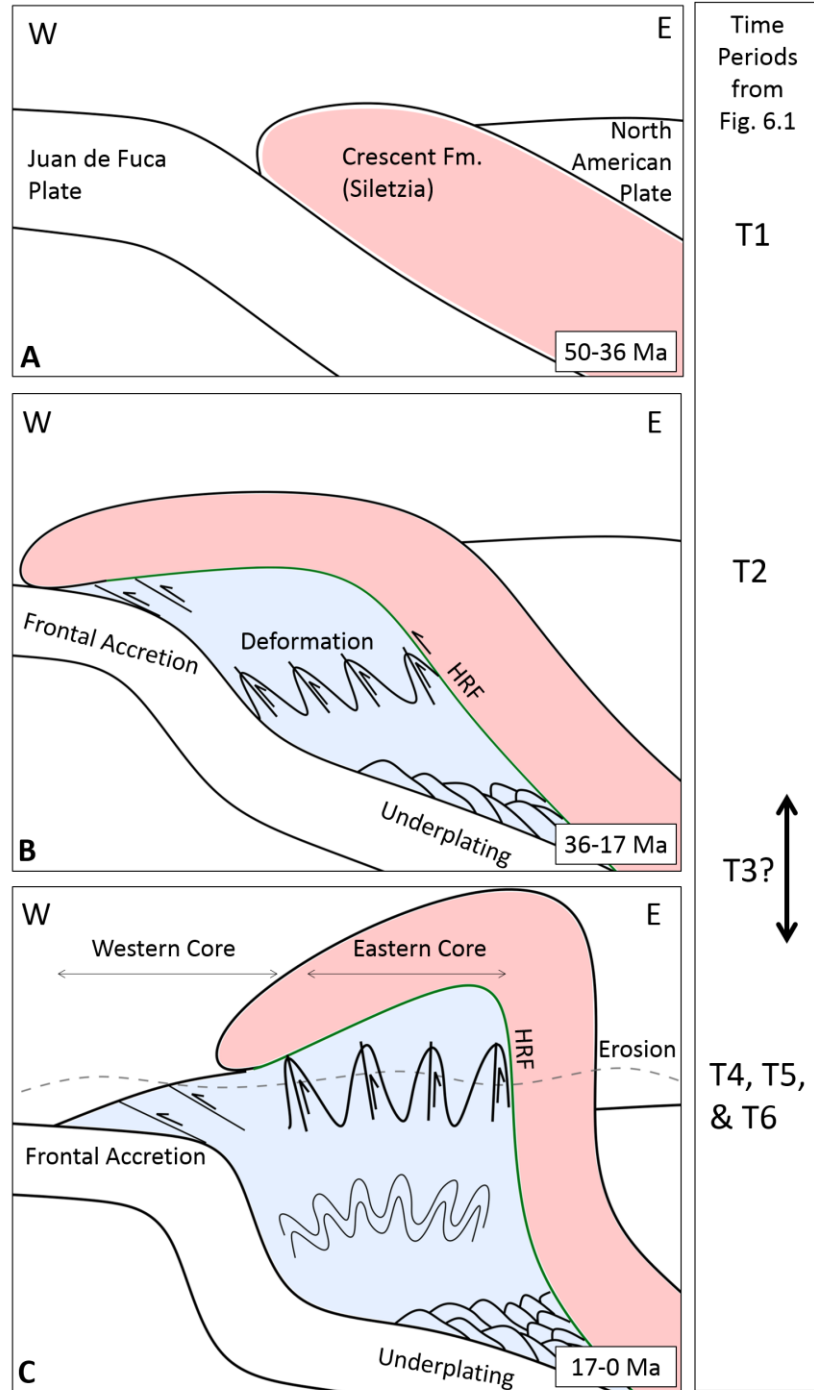
Figure 6.2. Diagrams showing the steps in deformation of the Olympic Peninsula. The relative timing of the events (T1-T6) relate to **Figure 6.1**. A) The Crescent Fm. is accreted to the North American Continent by 50 Ma and the subduction zone is established on the west side of the Siletzia terrane. B) The accretionary wedge thickens as sediments are accreted, underplated, and deformed. C) Exhumation begins and the HRF is rotated into its current, vertical position. The dotted line in (c) represents the current erosional surface. Diagrams are not to scale. The model is based on Batt et al. (2001), Tabor & Cady (1978), and Brandon & Vance (1992).

99

7. Implications for the Interpretation of Regional Structure & Geologic History

7.1 Comparison of the Hamma Hamma Transect to Regional Structures

7.1.1 Meta-Sediments of the Eastern Core

Tabor and Cady (1978) give the most robust structural dataset for the eastern core of the Olympic Mountains. The structures of interest in their study were bedding, cleavages, and pencil features. **Figure 7.1** shows a map of their data with the data from this study added in; the Hamma Hamma Transect falls spatially into the Outer Edge Domains. For many of their structural domains, they describe their bedding data as acting as a proxy for fold axial planes due to the isoclinal nature of the folds. The bedding data in Tabor & Cady's Domain 12 and the data from this study are not parallel to the axial plane and the folds are more open with a northwest plunge. Unlike Domain 12, the foliation in the Hamma Hamma Transect follows a similar trend to the bedding and foliation of the Outer Edge Domains, striking subparallel to the HRF. This study shows that the fold axial plane is not parallel to the dominant cleavage (or S2), suggesting that additional factors affected the formation of the foliation, such as shear folding.

Although Tabor and Cady (1978) describe cleavages as fabric planes that disrupt and offset bedding, they do not document fractures like those described at the sites in this study. Tabor and Cady may have grouped the cleavages and fractures together because of their similar appearance in the field. The micro-scale observations in this study demonstrate that they are different features that formed at different times. The fracture groups identified in this study do strike similarly to the axial plane, but other than this correlation, it is unclear how the fractures from the Hamma Hamma Transect compare to

Tabor & Cady's data. Similarly, there were no pencil structures identified in this study, so it is unclear how the data presented here related to the pencil orientations identified elsewhere in the meta-sedimentary core.

The deformation model for the data collected across the Hamma Hamma Transect suggests two stages of deformation with two states of stress: folds and foliations that formed first under an E-W oriented $\sigma 1$ that were rotated and fractured by a N-S/NNW-SSE oriented $\sigma 1$. Tabor & Cady's Domain 12 share similar fold structures, suggesting similarities in the deformation history, but foliation orientations are different and there is no fracture data to compare. Therefore, it is unclear to what degree Domain 12 and other areas in the Outer Edge Domains share the same deformational history or the same inferred states of stress through time. Since the cleavages, axial planes, and bedding are subparallel to the HRF, it may be that the HRF was folded into place and the structures were rotated along with it (as suggested by Tabor & Cady [1978]) by local states of stress different from the Hamma Hamma Transect. This would allow for different states of stress but a similar two stage history as proposed in this study. This theory is discussed in more detail in the following section.
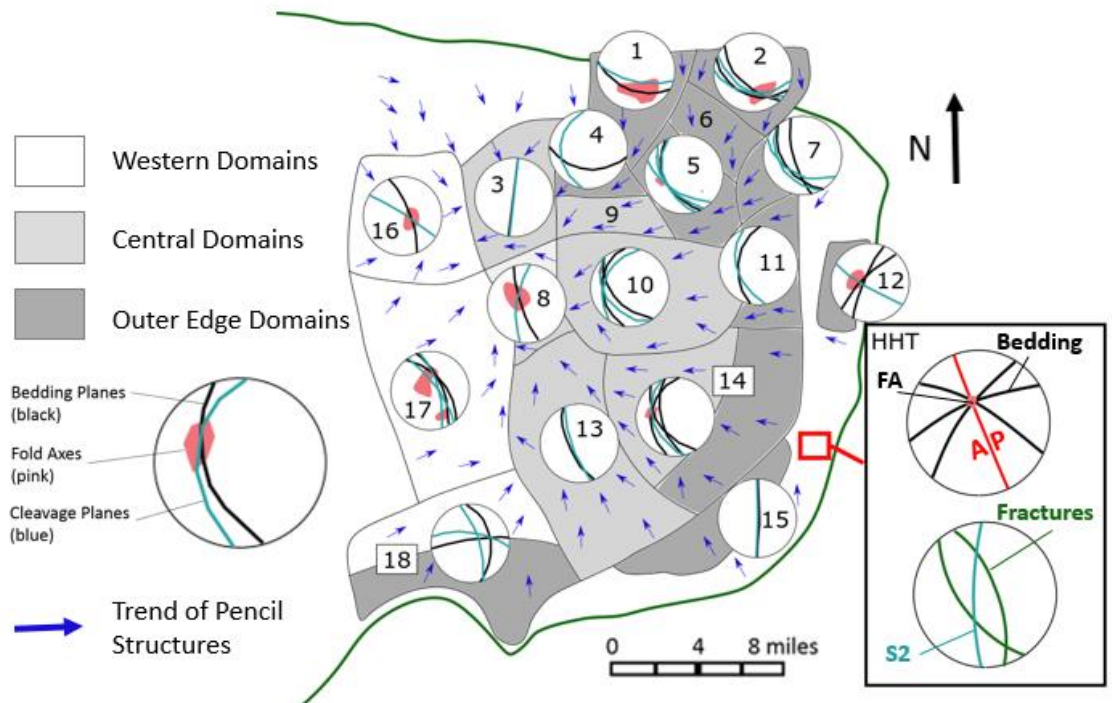
Figure 7.1. The Hamma Hamma Transect (HHT) structural data for the meta-sedimentary Sites 1 and 2 compared to the data from Tabor & Cady (1978). FA=Fold Axis, AP=Axial Plane.

7.1.2. The Crescent Formation of the Peripheral Rocks

The bedding data from the Hamma Hamma Transect is consistent with the bedding data for the rest of the Crescent Formation (**Fig. 7.2**). The beds are steeply dipping, which indicates that the rest of the Crescent Fm. has also been turned on end from its initial orientation of deposition. The general trend in the bedding in the region is that it strikes subparallel to the HRF, and wraps around the eastern core (Gerstel & Lingley, 2003; Tabor & Cady, 1978).

There is no detailed study of the fracture orientation at the outcrop scale in the Crescent Fm. so the data from this study are limited to comparisons with structures

mapped at the regional scale or proposed from the literature (**Fig. 7.2**). Map-scale faults in the area include the Saddle Mountain Fault (SMF), the Frigid Creek Fault (FCF), the Canyon River Fault (CRF), and the proposed western extent of the Seattle Fault (SF) (Blakely et al., 2009). Fault Groups B and C strike subparallel to the Saddle Mountain Fault, with Group C having the same dip direction. The Saddle Mountain Fault is a reverse fault with sinistral component, so although the orientation is similar, the slickenline data from Fault Groups B and C do not match this style of motion. Fault Group D strikes and dips similarly to the Seattle Fault, and the slickenlines of Fault Group D agree with the dip-slip motion of the Seattle Fault. The map-scale faults of the Crescent Formation have been interpreted as playing a role in accommodating N-S shortening from regional rotation of the Siletzia block (Blakely et al., 2009).

Eddy, Clark, & Polenz (2017) propose that there is a fault separating the Blue Mountain Unit and the rest of the Crescent Fm. that runs parallel to the HRF throughout the peninsula. Of the faults identified in this study, none of the fault groups are subparallel to the HRF or bedding, so it is unlikely these faults represent the fault proposed by Eddy, Clark, & Polenz (2017).
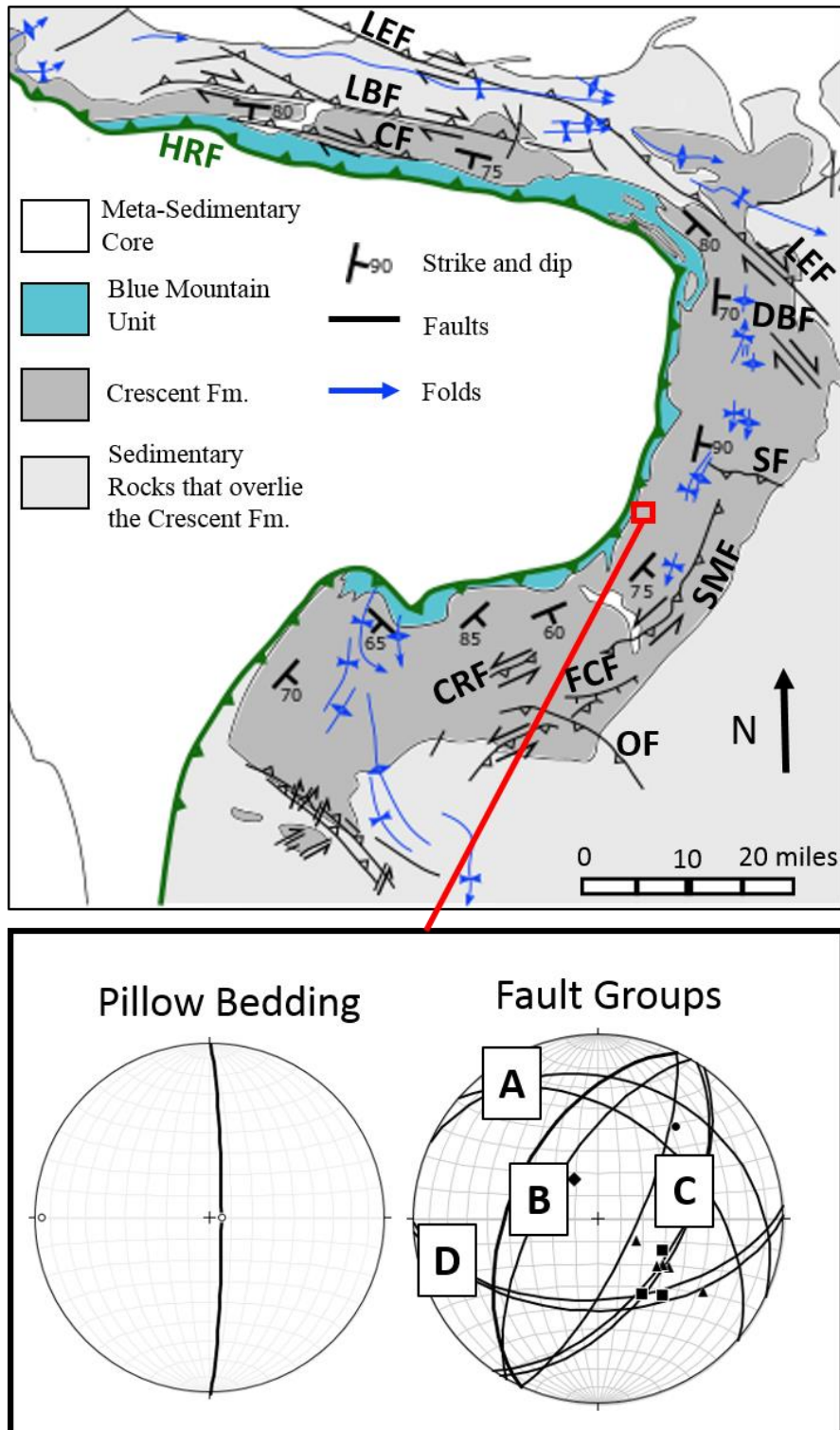
Figure 7.2. The Hamma Hamma Transect structural data for the pillow basalt outcrops, Sites 3 and 4, compared to regional structures of the Crescent Fm.

7.2 Analysis of Regional Structures Relative to the Models for Exhumation

In a classic accretionary complex, imbricate faults and moderately plunging folds form parallel to and dip towards the subduction margin (Davis, Suppe, & Dahlen, 1983). The Crescent Fm. has an arcuate shape, which Tabor & Cady (1978) state is either inherited from the shape of the accreted terrane or was established by deformation after accretion. Some researchers argue that this shape is a product of exhumational doming alone (Warnock, Burmester, & Engebretson, 1993) from the uneven E-W accretion of sediments along the orogen. The data from this study suggests E-W compression, which supports the accretionary model. However, other researchers cite N-S oriented shortening in the formation of the arcuate shape of the Crescent Fm. and as a driver of exhumation. The structural data presented from the Hamma Hamma Transect may also form from a N-S maximum stress. Therefore, it may be that the structures began as what would be expected for a normal accretionary wedge and were subsequently folded about a vertical axis as the rock packages were pushed against the Canadian Buttress (**Fig. 7.3**).
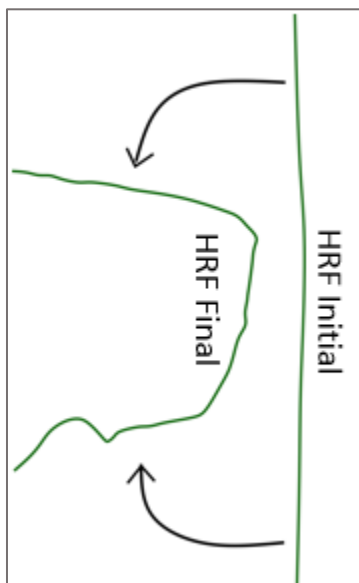
Figure 7.3. Hypothesis for the folding of the HRF by N-S shortening showing the proposed initial and final positions of the fault.

To address this hypothesis, the bedding and fault data for the Outer Edge

Domains in the eastern core and the Crescent were 'unfolded' in the same way as

expected for the HRF if the orogen originally had a straight subduction margin (**Fig. 7.4**).

The result is that faults and folds with orientations subparallel to the edge of the

peripheral rocks and the HRF have similar orientations along the strike of the orogen,

which is what is expected in a normal accretionary wedge. The rocks of the Hamma

Hamma Transect would not have been rotated in this model, so this would need to be

taken into account when comparing the Hamma Hamma Transect data with other

localities elsewhere in the Crescent Formation.
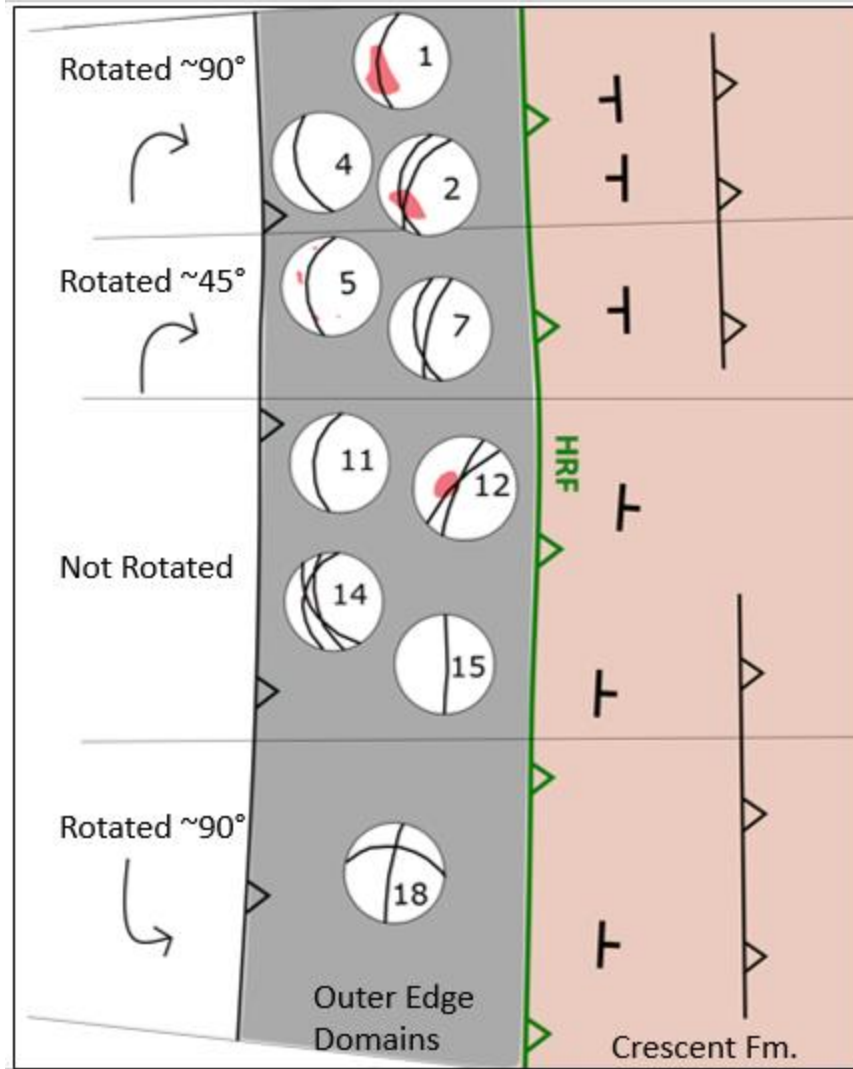
Figure 7.4. A schematic of how the bedding and fault data for the Outer Edge Domains and the Crescent Fm. would look if it were unfolded along with the HRF as depicted in **Figure 7.3**.

8. Conclusion

The purpose of this work was to characterize the structures at the meso-scale on both sides of the Hurricane Ridge Fault along the Hamma Hamma River Transect and then to interpret structures to create a model of deformation for the study area. This was accomplished by field mapping of structures, analysis of structural orientations in stereographic projection, and microscale analysis of samples collected from the sites.

Strain was accommodated in the meta-sedimentary rocks through folding, foliation development, fracturing, and rotation of the rock package. Strain was accommodated in the basalt by faulting, fracturing, rotation of beds, and foliation development in meta-sedimentary material along some bedding planes.

In the meta-sediments, two main periods of deformation are identified: one where the rocks deformed by folding and fabric formation under E-W or ENE-WSW oriented compression followed by another period in which the rocks were fractured and rotated by N-S or NNW-SSE oriented compression. In the pillow basalts, two or possibly three periods of deformation are identified: first a period of E-W compression that rotated and faulted the rocks, followed by further faulting from N-S or NNW-SSE oriented compression, and then finally, reactivation of the faults by vertical compression. The second step in the pillow basalts is speculative because the evidence for it is weaker than that for the other periods of deformation.

The interpretation of the data presented in this work supports the N-S oriented regional shortening of Siletzia model for Olympic exhumation (as described by

McCaffrey et al., 2007 and Wells et al., 2014). The fracturing and rotation of the folds in the meta-sediments and Fault Group D in the pillow basalts suggest deformation by a N-S or NNW-SSE oriented principal stress. However, the study area is small and the states of stress detected may be local phenomena. In order to truly test this model, more meso-scale structural studies would need to be performed in other areas of the peninsula.

References

Allmendinger, R. W., Cardozo, N. C., & Fisher, D. (2013) *Structural Geology Algorithms: Vectors & Tensors.* Cambridge, England: Cambridge University Press.

Anderson, E. M. (1905). The dynamics of faulting. *Edinburgh Geological Society Transactions*, *8*, pp. 393-402.

Batt, G. E., Brandon, M. T., Farley, K. A., & Roden-Tice, M. (2001). Tectonic synthesis of the Olympic Mountains segment of the Cascadia wedge, using two-dimensional thermal and kinematic modeling of thermochronological ages. *Journal of Geophysical Research*, *106*(B11), pp. 26731–26746.

Blakely, R. J., Sherrod, B. L., Hughes, J. F., Anderson, M. L., Wells, R. E., & Weaver, C. S. (2009). Saddle Mountain fault deformation zone, Olympic Peninsula, Washington: Western boundary of the Seattle uplift. *Geosphere, 5*(2), pp. 105–125.

Blakely, R. J., Sherrod, B. L., Weaver, C. S., Wells, R. E., Rohay, A. C., Barnett, E. A., & Knepprath, N. E. (2011). Connecting the Yakima fold and thrust belt to active faults in the Puget Lowland, Washington. *Journal of Geophysical Research, 116*(B07105), pp. 1–33.

Brandon, M. T., Roden-Tice, M. K., & Garver, J. I. (1998). Late Cenozoic exhumation of the Cascadia accretionary wedge in the Olympic Mountains, northwest Washington State. *Bulletin of the Geological Society of America, 110*(8), pp. 985–1009.

Brandon, M. T., & Vance, J. A. (1992). Tectonic evolution of the Cenozoic Olympic subduction complex, Washington State, as deduced from fission track ages for detrital zircons. *American Journal of Science, 292*, pp. 565-636.

Brocher, T. M., Wells, R. E., Lamb, A. P., & Weaver, C. S. (2017). Evidence for distributed clockwise rotation of the crust in the northwestern United States from fault geometries and focal mechanisms. *Tectonics, 36*, 787–818.

Cardozo, N. & Allmendinger, R. W. (2013). Spherical projections with OSXStereonet: Computers & Geosciences, 51, pp. 193-205.

Davis, D., Suppe, J., & Dahlen, F. A. (1983). Mechanics of fold-and-thrust belts and accretionary wedges. Journal of Geophysical Research, 88(B2), pp. 1153-1172.

Duncan, R. A. (1982). A captured island chain in the Coast Range of Oregon and Washington. *Journal of Geophysical Research, 87*(B13), pp. 10,827-10,837.

Eddy, M. P., Clark, K. P., & Polenz, M. (2017). Age and volcanic stratigraphy of the Eocene Siletzia oceanic plateau in Washington and on Vancouver Island. *Lithosphere, 9*(4), pp. 652–664.

Garrison R. E. (1972). Inter- and intrapillow limestones of the Olympic Peninsula, Washington. *The Journal of Geology, 80*(3), pp. 310-322.

Gerstel, W. J. & Lingley, W. S. Jr. (2000). Geologic Map of the Forks Quadrangle, Washington [map]. (1:100,000). Olympia, WA: Washington State Department of Natural Resources.

Gerstel, W. J. & Lingley, W. S. Jr. (2003). Geologic Map of the Mount Olympus Quadrangle, Washington [map]. (1:100,000). Olympia, WA: Washington State Department of Natural Resources.

Glassley, W. (1974). Geochemistry and tectonics of the Crescent Volcanic Rocks, Olympic Peninsula, Washington. *Geological Society of America Bulletin, 85*, pp. 785-794.

Healy, D. Blenkinsop, T. G., Timms, N. E., Meredith, P. G., Mitchell, T. M., Cooke, M. L. (2015). Polymodal faulting: Time for a new angle on shear failure. *Journal of Structural Geology, 80*, pp. 57-71.

Hirsch, D. M., & Babcock, R. S. (2009). Spatially heterogeneous burial and high-P/T metamorphism in the crescent formation, Olympic Peninsula, Washington. *American Mineralogist, 94*, pp.1103–1110.

Joyner, C. N. (2016). Lacustrine Megaturbidites and Displacement Waves: The Holocene Earthquake History of the Lake Creek-Boundary Creek Fault at Lake Crescent, Washington, USA. Thesis. Retrieved from https://repository.lib.ncsu.edu/handle/1840.20/33332.

Lamb, A. P., Liberty, L. M., Blakely, R. J., Pratt, T. L., Sherrod, B. L., & van Wijk, K. (2012). Western limits of the Seattle fault zone and its interaction with the Olympic Peninsula, Washington. *Geosphere, 8*(4), pp. 915–930.

Logan, R. L. (2003). Geologic Map of the Shelton 1:100,000 Quadrangle, Washington [map]. (1:100,000). Olympia, WA: Washington State Department of Natural Resources.

Lyttle N. A. & Clark D. B. (1975). New Analyses of Eocene basalt from the Olympic Peninsula, Washington. *Geological Society of America Bulletin, 86*, pp. 421-427.

McCaffrey, R., Qamar, A. I., King, R. W., Wells, R., Khazaradze, G., Williams, C. A., Stevens, C. W., Vollick, J. J., & Zwick, P. C. (2007). Fault locking, block rotation

and crustal deformation in the Pacific Northwest. *Geophysical Journal International, 169*(3), pp. 1315–1340.

Nelson, A. R., Personius, S. F., Wells, R. E., Schermer, E. R., Bradley, L., Buck, J., & Reitman, N. (2017). Holocene earthquakes of magnitude 7 during westward escape of the Olympic Mountains, Washington. *Bulletin of the Seismological Society of America, 107 (5)*, pp. 2394-2415.

Orange, D. L., Geddes, D. S., & Moore, J. C. (1993). Structural and fluid evolution of a young accretionary complex: the Hoh rock assemblage of the western Olympic Peninsula, Washington. *Geological Society of America Bulletin, 105*(8), pp. 1053–1075.

Pazzaglia, F. J., & Brandon, M. T. (2001). A fluvial record of long-term steady-state uplift and erosion across the Cascadia forearc high, Western Washington State. *American Journal of Science, 301*, pp. 385-431.

Schasse, H. W. (2003)a. Geologic Map of the Washington portion of the Cape Flattery 1:100,000 Quadrangle [map]. (1:100,000). Olympia, WA: Washington State Department of Natural Resources.

Schasse, H. W. (2003)b. Geologic Map of the Washington portion of the Port Angeles 1:100,000 Quadrangle [map]. (1:100,000). Olympia, WA: Washington State Department of Natural Resources.

Schmandt, B., & Humphreys, E. (2011). Seismically imaged relict slab from the 55 Ma Siletzia accretion to the northwest United States. *Geology, 39*(2), pp. 175–178.

Stipp, M., Stunitz, H., Heilbronner, R., & Schmid, S. M. (2002). The eastern Tonale fault zone: a 'natural laboratory' for crystal plastic deformation of quartz over a temperature range from 250 to 700 °C. *Journal of Structural Geology, 24*, pp. 1861-1884.

Tabor, R. W. & Cady, W. M. (1978). The structure of the Olympic Mountains, Washington; analysis of a subduction zone. *U. S. Geological Survey Professional Paper, 1033*.

Walsh, T. J. and Logan, R. L. (2007). Results of trenching the Canyon River Fault, southeast Olympic Mountains, Washington [abstract for GSA presentation]. Presented at GSA Cordilleran Section Meeting on 6 May 2007. Retrieved from: https://gsa.confex.com/gsa/2007CD/finalprogram/abstract_121357.htm.

Warnock, A. C., Burmester, R. F., & Engebretson, D. C. (1993). Paleomagnetism and tectonics of the Crescent Formation, northern Olympic Mountains, Washington. *Journal of Geophysical Research, 98*(B7), 11,729–11,741.

Wells, R., Bukry, D., Friedman, R., Pyle, D., Duncan, R., Haeussler, P., & Wooden, J. (2014). Geologic history of Siletzia, a large igneous province in the Oregon and Washington Coast Range: Correlation to the geomagnetic polarity time scale and implications for a long-lived Yellowstone hotspot. *Geosphere, 10*(4), 692–719.

Wells, R. E., & McCaffrey, R. (2013). Steady rotation of the Cascade arc. Geology, 41(9), pp. 1027–1030.

Wells, R. E., Weaver, C. S., & Blakely, R. J. (1998). Fore-arc migration in Cascadia and its neotectonic significance. *Geology, 26*(8), 759–762.

Appendix: Spatial and Structural Data

Table A1. GPS locations of each site from the Hamma Hamma Transect.

Site	Starting Point		Ending Point	
	Latitude	Longitude	Latitude	Longitude
1	47.575218	-123.261287	47.575818	-123.259652
2	47.580019	-123.251279	47.580186	-123.250621
3	47.582472	-123.228886	47.582588	-123.227200
4	47.582154	-123.223441	47.582376	-123.222123

Table A2. Strike and dip measurements of bedding planes from the meta-sedimentary outcrops along the Hamma Hamma Transect.

Site	Strike	Dip	Site	Strike	Dip	Site	Strike	Dip	Site	Strike	Dip
1a	190	78	1b	193	80	1d	131	85	1f	276	70
1a	189	81	1c	219	81	1e	172	61	1f	296	63
1a	156	81	1c	199	70	1e	176	60	1f	301	71
1a	173	75	1c	184	70	1e	261	78	1f	244	61
1a	191	84	1c	214	86	1e	269	69	1f	325	72
1a	196	81	1c	212	83	1e	247	72	1f	328	66
1a	186	80	1c	189	76	1e	252	73	2a	197	70
1a	183	75	1c	186	76	1e	258	75	2a	202	60
1a	188	75	1c	198	80	1e	1	89	2a	204	70
1a	166	76	1c	219	85	1e	174	81	2a	206	70
1a	180	75	1c	55	86	1e	265	80	2a	208	75
1a	172	79	1c	39	84	1e	268	58	2a	211	69
1a	175	79	1c	47	81	1e	272	69	2a	212	80

1b	208	68	1c	219	48	1e	250	64	2a	213	65
1b	208	66	1c	48	72	1e	242	76	2a	220	68
1b	206	61	1c	66	78	1e	273	70	2a	224	71
1b	220	65	1c	35	75	1e	268	68	2a	226	60
1b	215	76	1c	36	78	1e	273	57	2b	256	68
1b	215	68	1c	200	80	1e	270	64	2b	260	70
1b	218	70	1d	222	63	1f	271	54	2b	285	55
1b	214	65	1d	240	70	1f	263	60	2b	290	62
1b	213	80	1d	240	80	1f	270	56	2b	290	59
1b	214	81	1d	239	73	1f	294	70	2b	229	67
1b	211	76	1d	241	73	1f	298	65	2b	255	63
1b	214	73	1d	234	75	1f	312	79	2c	182	65
1b	206	70	1d	236	74	1f	324	74	2c	197	75
1b	210	76	1d	242	65	1f	306	82	2c	255	84
1b	204	71	1d	250	76	1f	311	70	2c	291	69
1b	206	84	1d	306	80	1f	306	75	2c	35	79
									2c	85	61

Table A3. Strike and dip measurements of mineralizes fractures (veins) from the meta-sedimentary outcrops along the Hamma Hamma Transect.

Site	Strike	Dip	Site	Strike	Dip	Site	Strike	Dip	Site	Strike	Dip
1c	113	55	1c	128	67	1c	336	46	2b	315	69
1c	116	68	1c	120	59	1e	159	61	2b	110	85
1c	113	61	1c	116	66	1e	150	65	2b	320	89
1c	117	59	1c	123	71	1f	300	71	2b	305	81
1c	104	71	1c	313	35	1f	216	54	2b	301	90
									2b	131	54

Table A4. Strike and dip measurements of foliation planes from the meta-sedimentary outcrops along the Hamma Hamma Transect.

Site	Strike	Dip	Site	Strike	Dip	Site	Strike	Dip
1a	136	61	1c	356	72	1f	331	80
1a	155	74	1c	359	74	1f	337	81
1a	167	72	1c	3	81	1f	356	80
1b	183	58	1c	184	82	1f	202	69
1b	178	70	1c	182	75	1f	330	80
1b	183	71	1c	172	68	2a	18	85
1b	189	72	1d	350	69	2a	350	80
1b	180	76	1d	1	85	2a	135	48
1b	174	71	1e	195	78	2b	181	69
1b	170	80	1e	175	74	2b	185	76
1b	175	73	1e	187	77	2b	189	66
1b	171	78	1e	189	90	2b	350	85
1b	165	65	1e	204	63	2b	177	61

1c	180	76	1e	345	77	2b	215	71
1c	184	84	1e	325	80	2b	176	65
1c	182	79	1f	332	80	2c	189	60
1c	179	81	1f	335	75	2c	193	65
1c	173	75						

Table A5. Strike and dip measurements of fracture planes and trend and plunge measurements of associated slickenlines from the meta-sediment outcrops along the Hamma Hamma Transect.

Site	Fracture Planes		Slickenlines		Site	Fracture Planes		Slickenlines	
	Strike	Dip	Plunge	Trend		Strike	Dip	Plunge	Trend
1a	82	40	40	165	1d	125	65	50	290
1a	100	55	54	178	1d	136	85	85	198
1a	75	45	45	180	1d	135	65	65	80
1a	96	55	55	295	1e	160	78	58	175
1b	125	45			1e	139	76	80	72
1b	130	51			1e	150	65		
1b	95	36			1e	135	35		
1b	75	35			1e	130	80		
1b	138	40	40	220	1e	148	40		
1b	141	36	35	208	1e	140	64		
1b	132	37	35	195	1f	300	79		
1b	96	48	45	215	1f	151	69		
1b	115	65	60	226	1f	141	53		
1b	156	58			1f	136	42		

1b	135	72			1f	165	80		
1b	278	74			1f	260	51		
1b	144	65			2a	142	57	80	290
1c	108	66			2a	332	64	55	126
1c	131	59			2a	334	70	60	120
1c	114	60			2a	135	65		
1c	162	65	20	155	2a	126	85		
1c	325	72	69	60	2a	105	75		
1c	158	70			2b	305	77		
1c	120	70			2b	275	66		
1c	65	36			2b	274	60		
1c	75	64			2b	285	68		
1c	141	56			2b	304	80		
1c	340	53			2b	135	69		
1c	317	43			2c	290	68		
1c	110	60			2c	293	78		
1c	104	69			2c	291	67		
1d	130	85			2c	328	71		

Table A6. Strike and dip measurements of bedding planes from the pillow basalt outcrops along the Hamma Hamma Transect.

Site	Strike	Dip	Site	Strike	Dip	Site	Strike	Dip	Site	Strike	Dip
3a	5	81	3b	176	84	3c	12	80	4c	170	74
3a	4	81	3b	165	83	3c	215	87	4c	125	86
3a	164	85	3b	344	80	3c	174	85	4c	172	81
3a	0	83	3b	11	84	3c	205	88	4c	354	89
3a	174	88	3b	18	89	3c	45	56	4c	10	89
3a	206	88	3b	354	81	4a	295	64	4d	177	87
3a	22	85	3b	181	71	4a	6	85	4d	14	90
3a	1	84	3b	4	75	4a	190	90	4d	130	54
3a	178	85	3b	170	81	4a	176	89	4d	21	81
3a	186	80	3c	180	89	4a	1	81	4d	5	90
3a	195	84	3c	8	56	4b	21	81	4d	170	88
3a	0	86	3c	165	72	4b	345	85	4d	354	86
3a	355	83	3c	340	42	4b	164	87	4d	186	78
3a	172	88	3c	12	78	4b	173	74	4d	182	85
3a	354	82	3c	358	88	4b	336	89	4d	6	90
3a	16	69	3c	324	79	4b	20	56	4d	182	73
3a	173	78	3c	325	63	4b	347	63	4d	210	76
3b	343	85	3c	171	78	4b	358	82	4d	173	74
3b	345	86	3c	178	86	4b	346	78	4d	336	89
3b	8	81	3c	18	86	4c	34	73	4d	20	56
									4d	347	63

Table A7. Strike and dip measurements of fault planes and trend and plunge measurements of associated slickenlines from the pillow basalt outcrops along the Hamma Hamma Transect.

Site	Fault Plane		Slickenlines	
	Strike	Dip	Plunge	Trend
3a	86	54	45	140
	32	54	51	125
			31	125
3a	210	65	65	305
3a	311	45	35	40
			65	265
3b	89	49	51	150
			58	116
3b	35	56	54	126
			56	129
4a	205	50		
4c	25	74	70	120
4d	295	25	45	315
			18	198

Table A8. Strike and dip measurements of mineralized fracture (vein) planes from the pillow basalt outcrops along the Hamma Hamma Transect.

Site	Strike	Dip	Site	Strike	Dip	Site	Strike	Dip	Site	Strike	Dip
3a	9	42	3a	340	5	3b	105	36	3c	285	17
3a	161	59	3b	305	46	3b	320	35	3c	345	19
3a	21	66	3b	351	29	3c	267	20	3c	355	31
3a	308	48	3b	345	31	3c	15	40	3c	290	12
3a	320	35	3b	356	30	3c	175	16	4a	303	62
3a	305	39	3b	318	15	3c	238	8	4a	312	40
3a	325	34	3b	296	26	3c	260	11	4c	350	45
3a	22	60	3b	25	40	3c	295	28	4d	327	57
3a	356	85	3b	340	12	3c	290	28	4d	314	59
3a	295	15	3b	5	25	3c	294	29	4d	350	57

Table A9. Strike and dip measurements of fracture planes from the pillow basalt outcrops along the Hamma Hamma Transect.

Site	Strike	Dip	Site	Strike	Dip	Site	Strike	Dip	Site	Strike	Dip
3a	122	78	3b	335	24	4a	195	26	4b	205	38
3a	129	81	3b	326	30	4a	187	15	4b	290	34
3a	300	44	3b	205	40	4a	313	36	4b	287	42
3a	284	28	3b	311	28	4a	312	41	4b	290	48
3a	287	26	3b	195	44	4a	212	48	4b	160	45
3a	306	45	3b	197	40	4a	160	57	4c	34	73
3a	291	43	3b	304	25	4a	188	51	4c	132	48
3a	350	61	3b	301	22	4a	242	51	4c	275	20
3b	174	82	3b	195	31	4a	228	38	4c	295	43
3b	134	86	4a	180	61	4a	301	51	4c	199	46
3b	260	60	4a	314	50	4a	351	79	4c	295	42
3b	271	42	4a	225	46	4b	298	61	4d	295	36
3b	325	80	4a	215	45	4b	219	41	4d	200	40
3b	150	82	4a	318	50	4b	178	42	4d	275	25
3c	218	18	4a	242	51	4b	290	41	4d	308	45
3c	160	74	4a	228	38	4b	310	36	4d	310	42
3c	235	36	4a	301	51	4b	298	39	4d	130	54
3c	177	31	4a	351	79	4b	298	31	4d	300	46
3c	186	28	4a	345	41	4b	240	21	4d	292	50
3c	188	28	4a	180	59	4b	299	38	4d	318	46
3c	334	32	4a	187	56	4b	298	40	4d	287	44

3c	270	43	4a	331	71	4b	250	35	4d	302	36
3c	202	35	4a	221	35	4b	298	45	4d	307	36
3c	265	11	4a	218	37	4b	307	39	4d	310	36
						4b	220	35	4d	298	39